bioRxiv preprint doi: https://doi.org/10.1101/2021.12.12.469460; this version posted August 7, 2022. The copyright holder for this preprint (which was not certified by peer review) is the author/funder. All rights reserved. No reuse allowed without permission.

Tabula Microcebus: A transcriptomic cell atlas of mouse lemur, an emerging primate model organism

The Tabula Microcebus Consortium*

bioRxiv preprint doi: https://doi.org/10.1101/2021.12.12.469460; this version posted August 7, 2022. The copyright holder for this preprint (which was not certified by peer review) is the author/funder. All rights reserved. No reuse allowed without permission.

The Tabula Microcebus Consortium

Lead authors

Camille Ezran[1, 2‡], Shixuan Liu[1, 2, 3‡], Stephen Chang[1, 2, 4‡], Jingsi Ming[5, 6], Olga Botvinnik[7], Lolita Penland[7], Alexander Tarashansky[7, 8], Antoine de Morree[9, 10], Kyle J. Travaglini[1, 2], Kazuteru Hasegawa[1, 11, 12], Hosu Sin[13], Rene Sit[7], Jennifer Okamoto[7], Rahul Sinha[14], Yue Zhang[2, 15], Caitlin J. Karanewsky[1, 2], Jozeph L. Pendleton[1, 2], Maurizio Morri[7], Martine Perret[16], Fabienne Aujard[16], Lubert Stryer[17], Steven Artandi[1, 11, 12], Margaret Fuller[13, 18], Irving L. Weissman[14], Thomas A. Rando[9], James E. Ferrell, Jr.[1, 3], Bo Wang[8], Iwijn De Vlaminck[19], Can Yang[6], Kerriann M. Casey[20], Megan A. Albertelli[20], Angela Oliveira Pisco[7], Jim Karkanias[7], Norma Neff[7], Angela Wu[21, 22], Stephen R. Quake[7, 8, 23]†, Mark A. Krasnow[1, 2]†

‡ Co-first authors

† Corresponding authors: krasnow@stanford.edu (M.A.K.), steve@quake-lab.org (S.R.Q.)

Leadership and coordination

Trainees: Camille Ezran[1, 2], Shixuan Liu[1, 2, 3], Stephen Chang[1, 2, 4]

Principal investigators: Mark A. Krasnow[1, 2], Stephen R. Quake[7, 8, 23], Angela Wu[21, 22], Norma Neff[7], Jim Karkanias[7], Angela Oliveira Pisco[7]

Donor recruitment and animal husbandry

Megan A. Albertelli[20], Caitlin J. Karanewsky[1, 2], Jozeph L. Pendleton[1, 2], Fabienne Aujard[16], Martine Perret[16], Liza Shapiro[24], Andriamahery Razafindrakoto[25], Hajanirina Noëline Ravelonjanahary[25], Patricia Wright[26], Anne D. Yoder[27], Cathy V. Williams[28], Robert Schopler[28], Ute Radespiel[29], Jean-Michel Verdier[30], Corinne Lautier[30], E. Christopher Kirk[24], Rebecca Lewis[24]

Necropsy, sample collection, biobanking, histology, and pathology

Kerriann M. Casey[20], Megan A. Albertelli[20], Caitlin J. Karanewsky[1, 2], Jozeph L. Pendleton[1, 2], Camille Ezran[1, 2], Shixuan Liu[1, 2, 3], Kyle J. Travaglini[1, 2], Astrid Gillich[1, 2], Zicheng Zhao[2, 20], Stephen Chang[1, 2, 4], Elias Godoy[20], Jérémy Terrien[16], Jacques Epelbaum[16, 31], Dita Gratzinger[32], Katherine Lucot[32], Tom Montine[32]

Tissue processing, annotation, and analysis [Principal investigators]

Aorta: Jessica D'Addabbo[33, 34], Isaac Bakerman[4], [Patricia Nguyen[12, 33, 34]]

Bladder: Aaron Kershner[1, 35], Karim Mrouj[36], [Philip Beachy[3, 13, 36, 37]]

Blood: Rahul Sinha[14], Camille Ezran[1, 2], Yue Zhang[2, 15], Shixuan Liu[1, 2, 3], Caitlin J. Karanewsky[1, 2], [Irving L. Weissman[14], Mark A. Krasnow[1, 2]]

Bone (limb, spine): Thomas Ambrosi[36], Malachia Hoover[36], Alina Alam[36], [Charles Chan[36]]

Bone marrow: Rahul Sinha[14], SoRi Jang[1, 2], Camille Ezran[1, 2], [Irving L. Weissman[14], Mark A. Krasnow[1, 2]]

Brain (cortex, brainstem, cerebellum): Avin Veerakumar[1, 2, 8, 38], Peng Li[1, 2], Andrea R. Yung[1, 2], Connor V. Duffy[2, 18], Song-Lin Ding[39], [Ed S. Lein[39], Silvana Konermann[1,2], Liqun Luo[2, 15], Trygve E. Bakken[39], Justus Kebschull[40], Rebecca D. Hodge[39], Mark A. Krasnow[1, 2]]

Colon/Small intestine: Taichi Isobe[41], [Michael F. Clarke[36]]

bioRxiv preprint doi: https://doi.org/10.1101/2021.12.12.469460; this version posted August 7, 2022. The copyright holder for this preprint (which was not certified by peer review) is the author/funder. All rights reserved. No reuse allowed without permission.

Diaphragm/Limb muscle: Antoine de Morree[9, 10], Biter Bilen[9], Jean Farup[9, 10], Andoni Urtasun[9], Jengmin Kang[9], [Thomas A. Rando[9]]
Eye: Ming Chen[18], Bao Xiang[42], Varun Ramanan Subramaniam[42], Shravani Mukherjee[42], Aditi Swarup[42], Lily Kim[18], Bronwyn Scott[42], Ahmad Al-Moujahed[42], [Albert Y. Wu[42], Douglas Vollrath[18], Lubert Stryer[17]]
Fat: Nicholas Schaum[9], Jingsi Ming[5, 6], Shixuan Liu[1, 2, 3], Amanda L. Wiggenhorn[32, 43], [Tony Wyss-Coray[9, 44], Jonathan Z. Long[32, 45], Angela Wu[21, 22]]
Ganglion (vagus nerve): Yin Liu[1, 2], [Mark A. Krasnow[1, 2]]
Heart: Stephen Chang[1, 2, 4], [Mark A. Krasnow[1, 2]]
Hypothalamus & Pituitary: Andrea R. Yung[1, 2], Shixuan Liu[1, 2, 3], [Mark A. Krasnow[1, 2]]
Kidney: Shixuan Liu[1, 2, 3], Ahmad Nabhan[1, 2], Lolita Penland[7], Yue Zhang[2, 15], Andrea R. Yung[1, 2], [Gabriel Loeb[46], Mark A. Krasnow[1, 2]]
Liver: Shengda Lin[47], Shixuan Liu[1, 2, 3], Honor Paine[48], Deviana Burhan[48], Aris Taychameekiatchai[48], [Steven Artandi[1, 11, 12], Bruce Wang[48]]
Lung: Kyle J. Travaglini[1, 2], Ahmad Nabhan[1, 2], F. Hernán Espinoza[1, 2], Astrid Gillich[1, 2], [Christin Kuo[49], Ross Metzger[49, 50], Mark A. Krasnow[1, 2]]
Lymph node: SoRi Jang[1, 2], Lolita Penland[7], [Norma Neff[7], Mark A. Krasnow[1, 2]]
Mammary gland: Zhen Qi[36], [Michael F. Clarke[36]]
Microbiome: Rebecca Culver[18], [Kerwyn C. Huang[7, 8, 51]]
Pancreas: Patrick Neuhöfer[1, 11, 12], Charles A. Chang[13, 52], Yan Hang[13, 52], [Seung K. Kim[12, 13, 52, 53], Steven Artandi[1, 11, 12]]
Prostate: Hannah Weinstein[54, 55, 56], Paul Allegakoen[54], [Franklin W. Huang[54]]
Salivary gland: Sivakamasundari V[36], [Philip Beachy[3, 13, 36, 37]]
Skin: Song Eun Lee[9, 44], [Tony Wyss-Coray[9, 44]]
Spleen: Lolita Penland[7,] Hannah K. Frank[32], Dita Gratzinger[32], [Norma Neff7, Scott D. Boyd[32]]
Testes: Kazuteru Hasegawa[1, 11, 12], Hosu Sin[13], Jingsi Ming[5, 6], [Steven Artandi[1, 11, 12], Margaret Fuller[13, 18], Angela Wu[21, 22]]
Thymus: Isaac Bakerman[4], Jessica D'Addabbo[33, 34], [Patricia Nguyen[12, 33, 34]]
Tongue: Wan-Jin Lu[36], Ankit Baghel[15], [Philip Beachy[3, 13, 36, 37]]
Trachea/Thyroid/Parathyroid: William Kong[36], [Philip Beachy[3, 13, 36, 37]]
Uterus/Abdominal mass: Lolita Penland[7], [Norma Neff[7]]

Library processing, sorting, and sequencing
Stephen Chang[1, 2, 4], Lolita Penland[7], Carly Israel[7], Rene Sit[7], Jennifer Okamoto[7], Yue Zhang[2, 15], Rahul Sinha[14], Shixuan Liu[1, 2, 3], Camille Ezran[1, 2], Kyle J. Travaglini[1, 2], Antoine de Morree[9, 10], Ahmad Nabhan[1, 2], Youcef Ouadah[1, 58], Jalal Baruni[1, 2, 15, 59], Robert C. Jones[8], Norma Neff[7], Maurizio Morri[7], Spyros Darmanis[7], Sheela Crasta[7], Jia Yan[7], Aditi Agrawal[7], Shelly Huynh[7], Brian Yu[7], James Webber[7]

Global data analysis [Principal investigators]
General analysis: Camille Ezran[1, 2], Shixuan Liu[1, 2, 3], [Mark A. Krasnow[1, 2]]
Sequence alignment: Stephen Chang[1, 2, 4], Kyle J. Travaglini[1, 2], Rahul Sinha[14], Rene Sit[7], [Mark A. Krasnow[1, 2], Irving L. Weissman[14], Stephen R. Quake[7, 8, 23]]
FIRM integration: Jingsi Ming[5, 6], [Angela Wu[21, 22], Can Yang[6]]
Molecular trajectory: Shixuan Liu[1, 2, 3], Camille Ezran[1, 2], Weilun Tan[7], [Mark A. Krasnow[1, 2]]

bioRxiv preprint doi: https://doi.org/10.1101/2021.12.12.469460; this version posted August 7, 2022. The copyright holder for this preprint (which was not certified by peer review) is the author/funder. All rights reserved. No reuse allowed without permission.

Global cell type comparison: Shixuan Liu[1, 2, 3], [Mark A. Krasnow[1, 2]]
Cross-species comparison: Olga Botvinnik[7], Alexander Tarashansky[7, 8], Saba Nafees[7], Shixuan Liu[1, 2, 3], Camille Ezran[1, 2], Kyle J. Travaglini[1, 2], Antoine de Morree[9, 10], Jia Zhao[6], Gefei Wang[6], [Jim Karkanias[7], Bo Wang[8], Stephen R. Quake[7, 8, 23], Mark A. Krasnow[1, 2], Thomas A. Rando[9], Angela Wu[21, 22], Can Yang[6]]
Spermatogenesis: Jingsi Ming[5, 6], Hosu Sin[13], Kazuteru Hasegawa[1, 11, 12], Camille Ezran[1, 2], [Angela Wu[21, 22], Margaret Fuller[13, 18], Steven Artandi[1, 11, 12], Can Yang[6], Mark A. Krasnow[1, 2]]
uTAR: Michael F.Z. Wang[19, 60], [Iwijn De Vlaminck[19]]
SICILIAN: Roozbeh Dehghannasiri[1, 61], Julia Olivieri[62], [Julia Salzman[1, 61]]
SAMap: Alexander Tarashansky[7, 8], [Bo Wang[8]]
Major histocompatibility locus: Lisbeth A. Guethlein[51, 63], Camille Ezran[1, 2], [Peter Parham[51, 63], Mark A. Krasnow[1, 2]]
B cell receptor locus: Hannah K. Frank[32, 57], Camille Ezran[1, 2], [Scott D. Boyd[32], Mark A. Krasnow[1, 2]]
Cross-tissue neutrophil trajectory: Camille Ezran[1, 2], Shixuan Liu[1, 2, 3], [Mark A. Krasnow[1, 2]]
Cross-tissue monocyte and macrophage comparison: Qiuyu Jing[21], Camille Ezran[1, 2], Shixuan Liu[1, 2, 3], [Angela Wu[21, 22], Mark A. Krasnow[1, 2]]
Chemokine expression: Camille Ezran[1, 2], [Mark A. Krasnow[1, 2]]
Metastatic tumor: Jane Antony[36], Camille Ezran[1, 2], [Michael F. Clarke[36], Mark A. Krasnow[1, 2]]
Endothelium: Camille Ezran[1, 2], Astrid Gillich[1, 2], Geoff Stanley[8], [Ross Metzger[49, 50], Mark A. Krasnow[1, 2], Stephen R. Quake[7, 8, 23]]
Adipocytes: Jinxurong Yang[21], Jingsi Ming[5, 6], Camille Ezran[1, 2], Shixuan Liu[1, 2, 3], [Jonathan Z. Long[32, 45], Angela Wu[21, 22], Mark A. Krasnow[1, 2], Can Yang[6]]
Primate-specific genes: Winston Koh[64, 65], Camille Ezran[1, 2], [Mark A. Krasnow[1, 2]]
Global hormone signaling: Shixuan Liu[1, 2, 3], [James E. Ferrell, Jr.[1, 3], Mark A. Krasnow[1, 2]]
OnClass: [Sheng Wang[66]]
Data portal/Online histology atlas: Zicheng Zhao[2, 20], Snigdha Agarwal[7], Kyle Awayan[7], Aaron McGeever[7], Venkata N. P. Vemuri[7], [Stephen R. Quake[7, 8, 23], Angela Oliveira Pisco[7]]

Principal investigators (A-Z)
Megan A. Albertelli[20], Steven Artandi[1, 11, 12], Fabienne Aujard[16], Trygve E. Bakken[39], Philip Beachy[3, 13, 36, 37], Scott D. Boyd[32], Kerriann M. Casey[20], Charles Chan[36], Michael F. Clarke[36], Jacques Epelbaum[16, 31], James E. Ferrell, Jr.[1, 3], Margaret Fuller[13, 18], Dita Gratzinger[32], Franklin W. Huang[54], Kerwyn C. Huang[7, 8, 51], Jim Karkanias[7], Justus Kebschull[40], Seung K. Kim[12, 13, 52, 53], Silvana Konermann[1,2], Mark A. Krasnow[1, 2], Christin Kuo[49], Ed S. Lein[39], Shengda Lin[47], Gabriel Loeb[46], Jonathan Z. Long[32, 45], Liqun Luo[2, 15], Ross Metzger[49, 50], Jingsi Ming[5, 6], Tom Montine[32], Norma Neff[7], Patricia Nguyen[12, 33, 34], Peter Parham[51, 63], Martine Perret[16], Angela Oliveira Pisco[7], Stephen R. Quake[7, 8, 23], Thomas A. Rando[9], Ute Radespiel[29], Julia Salzman[1, 61], Liza Shapiro[24], Lubert Stryer[17], Jérémy Terrien[16], Jean-Michel Verdier[30], Iwijn De Vlaminck[19], Douglas Vollrath[18], Bo Wang[8], Bruce Wang[48], Sheng Wang[66], Irving L. Weissman[14], Patricia Wright[26], Tony Wyss-Coray[9, 44], Albert Y. Wu[42], Angela Wu[21, 22], Can Yang[6], Anne D. Yoder[27]

bioRxiv preprint doi: https://doi.org/10.1101/2021.12.12.469460; this version posted August 7, 2022. The copyright holder for this preprint (which was not certified by peer review) is the author/funder. All rights reserved. No reuse allowed without permission.

Writing
Camille Ezran[1, 2,] Shixuan Liu[1, 2, 3], Stephen Chang[1, 2, 4], Jingsi Ming[5, 6], Antoine de Morree[9, 10], Lubert Stryer[17], Angela Wu[21, 22], Stephen R. Quake[7, 8, 23], Mark A. Krasnow[1, 2]

Affiliations
1. Department of Biochemistry, Stanford University School of Medicine, Stanford, CA, USA.
2. Howard Hughes Medical Institute, USA.
3. Department of Chemical and Systems Biology, Stanford University School of Medicine, Stanford, CA, USA.
4. Department of Medicine, Division of Cardiovascular Medicine, Stanford University, Stanford, CA, USA.
5. Academy of Statistics and Interdisciplinary Sciences, KLATASDS-MOE, East China Normal University, Shanghai, China.
6. Department of Mathematics, Hong Kong University of Science and Technology, Hong Kong SAR, China.
7. Chan Zuckerberg Biohub, San Francisco, CA, USA.
8. Department of Bioengineering, Stanford University, Stanford, CA, USA.
9. Department of Neurology and Neurological Sciences, Stanford University School of Medicine, Stanford, CA, USA.
10. Department of Biomedicine, Aarhus University, Aarhus, Denmark.
11. Stanford Cancer Institute, Stanford University School of Medicine, Stanford, CA, USA.
12. Department of Medicine, Stanford University School of Medicine, Stanford, CA, USA.
13. Department of Developmental Biology, Stanford University School of Medicine, Stanford, CA, USA.
14. Stanford Institute for Stem Cell Biology and Regenerative Medicine, Stanford, CA, USA.
15. Department of Biology, Stanford University, Stanford, CA, USA.
16. Adaptive Mechanisms and Evolution (MECADEV), UMR 7179, National Center for Scientific Research, National Museum of Natural History, Brunoy, France.
17. Department of Neurobiology, Stanford University School of Medicine, Stanford, CA, USA.
18. Department of Genetics, Stanford University School of Medicine, Stanford, CA, USA.
19. Nancy E. and Peter C. Meinig School of Biomedical Engineering, Cornell University, Ithaca, NY, USA.
20. Department of Comparative Medicine, Stanford University School of Medicine, Stanford, CA, USA.
21. Division of Life Science, Hong Kong University of Science and Technology, Hong Kong SAR, China.
22. Department of Chemical and Biological Engineering and Center for Aging Science, Hong Kong University of Science and Technology, Hong Kong SAR, China.
23. Department of Applied Physics, Stanford University, Stanford, CA, USA.
24. Department of Anthropology, University of Texas at Austin, Austin, TX, USA.
25. Department of Animal Biology, Faculty of Science, University of Antananarivo, Antananarivo 101, BP 566, Madagascar.
26. Department of Anthropology, Stony Brook University, NY, USA.

bioRxiv preprint doi: https://doi.org/10.1101/2021.12.12.469460; this version posted August 7, 2022. The copyright holder for this preprint (which was not certified by peer review) is the author/funder. All rights reserved. No reuse allowed without permission.

27. Department of Biology, University Program in Genetics & Genomics, Duke University, Durham, NC, USA.
28. Duke Lemur Center, Durham, NC, USA.
29. Institute of Zoology, University of Veterinary Medicine Hannover, Germany.
30. MMDN, University of Montpellier, EPHE-PSL, INSERM, Montpellier, France.
31. Unité Mixte de Recherche en Santé 894 INSERM, Centre de Psychiatrie et Neurosciences, Université Paris Descartes, Sorbonne, Paris, France
32. Department of Pathology, Stanford University School of Medicine, Stanford, CA, USA.
33. Division of Cardiovascular Medicine, Stanford University, Stanford, CA, USA.
34. Stanford Cardiovascular Institute, Stanford, CA, USA.
35. Institute of Stem Cell Biology and Regenerative Medicine, Stanford University School of Medicine, Stanford, CA, USA.
36. Institute for Stem Cell Biology and Regenerative Medicine, Stanford University School of Medicine, Stanford, CA, USA.
37. Department of Urology, Stanford University School of Medicine, Stanford, CA, USA.
38. Medical Scientist Training Program, Stanford University School of Medicine, Stanford, CA, USA.
39. Human Cell Types Department, Allen Institute for Brain Science, Seattle, WA, USA.
40. Department of Biomedical Engineering, Johns Hopkins School of Medicine, Baltimore, MD, USA.
41. Department of Oncology and Social Medicine, Kyushu University, Japan.
42. Department of Ophthalmology, Stanford University School of Medicine, Stanford, CA, USA.
43. Department of Chemistry, Stanford University, Stanford, CA, USA.
44. Wu Tsai Neurosciences Institute, Stanford, CA, USA.
45. Stanford ChEM-H, Stanford, CA, USA.
46. Division of Nephrology, Department of Medicine, University of California San Francisco, San Francisco, CA, USA.
47. Zhejiang Provincial Key Laboratory for Cancer Molecular Cell Biology, Life Sciences Institute, Zhejiang University, Hangzhou, Zhejiang, China.
48. Department of Medicine and Liver Center, University of California San Francisco, San Francisco, CA, USA.
49. Department of Pediatrics, Stanford University School of Medicine, Stanford, CA, USA.
50. Division of Cardiology, Stanford University School of Medicine, Stanford, CA, USA.
51. Department of Microbiology and Immunology, Stanford University School of Medicine, Stanford, CA, USA.
52. Stanford Diabetes Research Center, Stanford, CA, USA.
53. JDRF Center of Excellence, Stanford, CA, USA.
54. Division of Hematology/Oncology, Department of Medicine, University of California San Francisco, San Francisco, CA, USA.
55. Helen Diller Family Comprehensive Cancer Center, University of California San Francisco, San Francisco, CA, USA.
56. Bakar Computational Health Sciences Institute, University of California San Francisco, San Francisco, CA, USA.
57. Department of Ecology and Evolutionary Biology, Tulane University, New Orleans, LA, USA.

bioRxiv preprint doi: https://doi.org/10.1101/2021.12.12.469460; this version posted August 7, 2022. The copyright holder for this preprint (which was not certified by peer review) is the author/funder. All rights reserved. No reuse allowed without permission.

58. Program in Cancer Biology, Stanford University School of Medicine, Stanford, CA, USA.
59. Department of Anesthesiology, Perioperative and Pain Medicine, Stanford University School of Medicine, Stanford, CA, USA.
60. Department of Computational Biology, Cornell University, Ithaca, NY, USA.
61. Department of Biomedical Data Science, Stanford University, Stanford, CA, USA.
62. Institute for Computational and Mathematical Engineering, Stanford University, Stanford, CA, USA.
63. Department of Structural Biology, Stanford University School of Medicine, Stanford, CA, USA.
64. Institute of Bioengineering and Bioimaging, Agency of Science Technology and Research, Singapore.
65. Bioinformatics Institute, Agency of Science Technology and Research, Singapore.
66. Paul G. Allen School of Computer Science & Engineering, University of Washington, Seattle, WA, USA.

bioRxiv preprint doi: https://doi.org/10.1101/2021.12.12.469460; this version posted August 7, 2022. The copyright holder for this preprint (which was not certified by peer review) is the author/funder. All rights reserved. No reuse allowed without permission.

ABSTRACT

Mouse lemurs are the smallest, fastest reproducing, and among the most abundant primates, and an emerging model organism for primate biology, behavior, health and conservation. Although much has been learned about their physiology and their Madagascar ecology and phylogeny, little is known about their cellular and molecular biology. Here we used droplet- and plate-based single cell RNA-sequencing to profile 226,000 cells from 27 mouse lemur organs and tissues opportunistically procured from four donors clinically and histologically characterized. Using computational cell clustering, integration, and expert cell annotation, we defined and biologically organized over 750 mouse lemur molecular cell types and their full gene expression profiles. These include cognates of most classical human cell types, including stem and progenitor cells, and the developmental programs for spermatogenesis, hematopoiesis, and other adult tissues. We also described dozens of previously unidentified or sparsely characterized cell types and subtypes. We globally compared cell type expression profiles to define the molecular relationships of cell types across the body, and explored primate cell type evolution by comparing mouse lemur cell profiles to those of the homologous cells in human and mouse. This revealed cell type specific patterns of primate cell specialization even within a single tissue compartment, as well as many cell types for which lemur provides a better human model than mouse. The atlas provides a cellular and molecular foundation for studying this primate model organism, and establishes a general approach for other emerging model organisms.

bioRxiv preprint doi: https://doi.org/10.1101/2021.12.12.469460; this version posted August 7, 2022. The copyright holder for this preprint (which was not certified by peer review) is the author/funder. All rights reserved. No reuse allowed without permission.

INTRODUCTION

Systematic genetic and genomic studies of a handful of diverse organisms over the past half century have transformed our understanding of biology. But many of the most interesting and important aspects of primate biology, behavior, disease, and conservation are absent or poorly modeled in mice or any of the other established genetic model organisms[1–3]. Mouse lemurs are the smallest (~50 g), fastest reproducing (2 month gestation, 8 month (minimum) generation, 1-4 offspring per pregnancy) and among the most abundant primates (millions to tens of millions), and an emerging primate model organism[4]. Although much has been learned from laboratory studies of their physiology and aging[5–10], and from field studies in Madagascar of their ecology, behavior, and phylogeny[11–14], little is known about their genetics or cellular and molecular biology.

To establish a new genetic model organism, the first step has traditionally been to characterize the wild type and then systematically screen for interesting phenotypes and map the affected genes and underlying mutations or, since the advent of gene targeting, to create targeted mutations and assess their phenotype, as is standard in mouse. Systematic screens are underway for mouse lemur, leveraging their standing genetic diversity and the large pool of naturally-occurring mutations (Karanewsky et al, in prep; Chang et al, in prep), as in human genetics research. The next step is to create a genetic map or reference genome sequence, which is already available for mouse lemur[15] and is becoming increasingly affordable, accurate, and complete with powerful new genomic sequencing techniques[16]. With the accompanying development of single cell RNA-sequencing (scRNA-seq) technologies[17], we reasoned that a reference molecular cell atlas would provide a cellular and molecular foundation that would aid definition and understanding of wild type organism, organ, cell and gene function, enable new

bioRxiv preprint doi: https://doi.org/10.1101/2021.12.12.469460; this version posted August 7, 2022. The copyright holder for this preprint (which was not certified by peer review) is the author/funder. All rights reserved. No reuse allowed without permission.

types of cellular and molecular screens, and speed genetic mapping, while providing unprecedented resolution and insights into primate specializations and evolution.

Here we set out to create a comprehensive transcriptomic cell atlas of the mouse lemur *Microcebus murinus*, using a similar strategy to the one we used recently to construct the Tabula Muris mouse cell atlas[18,19] and the human lung cell atlas[20] (Fig. 1). We adapted the strategy to address several challenges for a new model organism. First, because there was no classical histological atlas, little molecular information, and few cell markers, we relied on the extensive knowledge of human and mouse cell markers (Table 1) from the long history of these fields plus the new atlases. Second, unlike classical model organisms but similar to human studies, donors are of different genetic backgrounds, ages, and diseases. Hence we collected extensive clinical data and histopathology on every donor and organ[21], and as in the prior Tabula Muris atlases we procured multiple organs from each donor and processed them in parallel (Fig. 1 a-c, Table 2), thereby controlling for the many technical and biological variables, at least among cell profiles from the same donor. Finally, there is heightened sensitivity for primate studies, so our strategy was opportunistic and designed to maximize information from each donor. To achieve our goal, we brought together experts from diverse fields, including mouse lemur biologists, veterinarians, pathologists, tissue experts, single cell genomics specialists, and computational leaders, to create the Tabula Microcebus Consortium - a team of over 150 collaborating scientists from over 50 laboratories at fifteen institutions worldwide.

bioRxiv preprint doi: https://doi.org/10.1101/2021.12.12.469460; this version posted August 7, 2022. The copyright holder for this preprint (which was not certified by peer review) is the author/funder. All rights reserved. No reuse allowed without permission.

RESULTS

1. Expression profiles of 226,000 cells from 27 mouse lemur organs

The approach used to create a mouse lemur molecular cell atlas is diagrammed in Fig. 1. Two male and two female aged laboratory *Microcebus murinus* mouse lemurs (L1, 9 y/o male; L2, 10 y/o female; L3 11 y/o female; L4, 11 y/o male) were euthanized for humane reasons over a 5 year period due to clinical conditions that failed to respond to therapy, as detailed in the companion manuscript[21]. Samples were then opportunistically collected for analysis. At the time of euthanasia, blood was drawn, then fresh tissues were quickly isolated (<2 hours post-euthanasia) by a veterinary pathologist and divided into samples that were immediately fixed for pathology or rapidly transported (minutes) at 4°C to the lab where organ-specific experts dissociated each tissue into single cell suspensions for expression profiling using protocols optimized for each organ (Fig. 1a and Supplementary Methods). Full veterinary evaluation, clinical pathology, and histopathological analysis are provided in a companion manuscript[21] as well as metadata for each individual, organ, and cell profiled in Supplementary Methods. This created a classical histological atlas of the mouse lemur (Fig. 1b, https://tabula-microcebus.ds.czbiohub.org/).

From each individual, 3 to 24 organs and tissues were profiled by scRNA-seq, cumulatively totaling 27 different organs and tissues, most of which (20) were profiled in at least two subjects (Fig. 1c and Table 2). Beyond the 19 profiled in mouse for Tabula Muris Senis (aorta, bladder, bone marrow, brain, diaphragm, fat depot (mesenteric, subcutaneous, brown interscapular, and peri-gonadal), heart, kidney, colon, limb muscle, liver, lung, mammary gland, pancreas, skin, spleen, thymus, tongue, and trachea), we also profiled blood, bone, brainstem, pituitary gland, retina, small intestine, testis, and uterus (Fig. 1c).

bioRxiv preprint doi: https://doi.org/10.1101/2021.12.12.469460; this version posted August 7, 2022. The copyright holder for this preprint (which was not certified by peer review) is the author/funder. All rights reserved. No reuse allowed without permission.

RNA sequencing libraries were prepared directly from single cell suspensions of each organ from each individual using the droplet-based 10x Chromium (10x) protocol. For most organs, aliquots of the cell suspensions were also FACS-sorted for live cells, and for heart cardiomyocytes were hand-picked, and then RNA sequencing libraries were prepared robotically from individual cells using the plate-based Smart-seq2 (SS2) protocol. The 10x and SS2 libraries were sequenced to achieve saturation on an Illumina NovaSeq 6000 System (10x, 26 bp and 90 bp paired-end reads; SS2, 2 x 100 bp paired-end reads). The higher throughput and lower cost of 10x allowed profiling of more cells, whereas SS2 provided greater transcriptomic coverage that aided cell classification, detection of genes expressed at low levels, and gene discovery and structure characterization (accompanying Tabula Microcebus manuscript 2). The 10x sequencing reads were demultiplexed, assigned to cells, and aligned to the *M. murinus* genome (assembly: Mmur 3.0[15], accession: GCF_000165445.2; annotation: NCBI Refseq Annotation Release 101) using Cell Ranger (10xGenomics). SS2 sequencing reads were aligned to the same genome annotation using STAR two-pass mapping, in which the first pass identified splice junctions that were added to the gene reference to improve second pass mapping. For both platforms, the aligned reads were counted (as unique molecular identifiers (UMIs) for 10x, and as reads for SS2) to determine the level of expression in each cell for each gene and scaled using Seurat v2 (see Methods) (Butler et al, 2018, Nature Biotech). After initial filtering of cell expression profiles for gene count (<500 expressed genes) and sequencing read/UMI parameters (<1000 UMIs for 10x and <5,000 reads for SS2, except for heart as described in Methods) and removing cells with profiles compromised by index switching[22], we obtained 244,081 cell profiles. We then identified low quality profiles (predominantly tRNA, rRNAs, and/or high levels of immediate early genes) and putative cell doublets, leaving 226,701 high quality single cell

bioRxiv preprint doi: https://doi.org/10.1101/2021.12.12.469460; this version posted August 7, 2022. The copyright holder for this preprint (which was not certified by peer review) is the author/funder. All rights reserved. No reuse allowed without permission.

transcriptomic profiles: 214,890 from 10x (16,682 - 88,910 per individual) and 11,811 from SS2 (394 - 6,723 per individual), distributed across four individuals and 27 organs (Fig. 1 c-d, Table 2).

To identify cells with similar gene expression profiles in each organ, the profiles obtained from 10x scRNA-seq analysis of each organ of each individual were separately analyzed through dimensionality reduction by principal component analysis (PCA), visualization in 2-dimensional projections with t-Stochastic Neighbor Embedding (t-SNE) and Uniform Manifold Approximation and Projection (UMAP), and clustering by the Louvain method in Seurat v2. For each obtained cluster of cells with similar profiles, the tissue compartment (epithelial, endothelial, stromal, immune, neural, and germ) was assigned based on expression of the mouse lemur orthologs of compartment-specific marker genes from mouse and human (Table 1)[20]. Cells from each compartment of each organ from each individual were then separately and iteratively clustered until the differentially-expressed genes that distinguished the resultant cell clusters were deemed not biologically relevant (e.g., stress or ribosomal genes) (Fig. 1e). Each resultant cluster was assigned a cell type designation, as detailed below.

We then integrated the cell expression profiles obtained from SS2 scRNA-seq analysis with the 10x dataset from the same organ and individual (Fig. 1 e-f). For this cross-platform integration we used FIRM[23], an algorithm that accounts for differences in cell type composition between the two platforms by finding the nearest 10x cell cluster for each SS2 cluster in the same embedded space, then subsampling the data to ensure that the proportion of cells from each cluster match across both platforms, and finally rescaling the gene expression values accordingly to re-calculate the embedding. Compared to existing batch correction algorithms, this method provided superior integration of shared cell types across platforms while preserving the original

bioRxiv preprint doi: https://doi.org/10.1101/2021.12.12.469460; this version posted August 7, 2022. The copyright holder for this preprint (which was not certified by peer review) is the author/funder. All rights reserved. No reuse allowed without permission.

structure for each dataset (Fig. 1 f-g). The cell type designation of each SS2 cell profile was automatically assigned based on the designation of the neighboring 10x cells, and manually curated.

We next used FIRM to integrate the combined 10x/SS2 datasets for each organ across the 2-4 profiled individuals, and then to integrate the profiles across all 27 organs into a single embedded space (Fig. 1 e-g). At each integration step, cell type designations were manually verified by a single expert to ensure consistency of nomenclature throughout the atlas. In this way, cell profiles that co-clustered across organs were given the same cell type designation, and clusters distinguished only in the merged atlas (e.g., related cells too rare in an individual organ to separate from other clusters in that organ) were re-assigned their own cell type designation. This approach identified 768 molecularly-distinct cell populations ("molecular cell types") across the 27 profiled organs, with 28±17 (mean±SD) cell populations per organ and 294±1007 cells in each population (Fig. 1c-d, Table 2), which were given 256 different cell designations as detailed below (Fig. 2a).

2. Identification of hundreds of mouse lemur cell types and their expression profiles

To assign provisional cell identities and names to the 768 molecular cell types, we first compiled a list from the literature of canonical marker genes for all of the mouse and human cell types in each compartment of the 27 profiled organs, and found the orthologous mouse lemur genes (Table 1 and Methods). We then searched among the cell clusters of each organ compartment for clusters enriched in expression of each set of cell type marker genes and assigned cells in those clusters the name of the corresponding human and/or mouse cell type and their corresponding cell ontology[24]; for cell types with small numbers, we used expert, biologically-guided manual curation. This allowed us to name almost all cell populations,

bioRxiv preprint doi: https://doi.org/10.1101/2021.12.12.469460; this version posted August 7, 2022. The copyright holder for this preprint (which was not certified by peer review) is the author/funder. All rights reserved. No reuse allowed without permission.

although for many (34) cell designations there were multiple corresponding cell populations (Fig. 2 a-b, Fig. S1). This was resolved by adding a suffix to the cell designations recognizing a differentially-expressed gene or gene signature that distinguished them (see Section 4). For lung and muscle, we verified that these manual, expert-curated cell type assignments showed good agreement with automated cell identity assignments using Self-Assembling Manifold mapping (SAMap)[25], an algorithm that computationally aligns the mouse lemur cell expression profiles to well curated and validated cell profiles we previously obtained for the corresponding mouse and human organs (see Section 6). We identified the differentially-expressed genes that are enriched in each cell type relative to the entire atlas, to other cell types of the same tissue, and to the same compartment of that tissue (Table 3).

Examples of the identified and named cell types for six of the profiled tissues are shown in Fig. 3a (kidney) and Fig. S2 (brain cortex, brainstem, hypothalamus/pituitary, eye retina, limb muscle). For limb muscle (Fig. S2 e-f), we identified 31 molecular cell types distributed across the endothelial (7 types), stromal (10 types), and immune (14 types) compartments. We also profiled, though less deeply, another skeletal muscle (diaphragm) and identified 13 of the corresponding cell types. Stromal cells of limb muscle included putative tendon cells (express tenocyte markers tenomodulin *TNMD+* and scleraxis *SCX+*) and adipocytes (adiponectin *ADIPOQ+*). Fatty infiltrates are rarely seen in aged murine skeletal muscle[26] but are common in aged human muscle[27], suggesting mouse lemur could provide a valuable model of fatty infiltration of muscle during human aging. We also identified vascular smooth muscle cells (*ACTA2+ MYH11+)* and pericytes (*ACTA2+ HIGD1B+*) as well as cells expressing mature myocyte markers (*ACTA1+*, *MYL1+*), presumably the self-sealed fragments of mature

bioRxiv preprint doi: https://doi.org/10.1101/2021.12.12.469460; this version posted August 7, 2022. The copyright holder for this preprint (which was not certified by peer review) is the author/funder. All rights reserved. No reuse allowed without permission.

myofibers. Based on expression of troponin isoforms, myofibers were further subdivided into fast (*TNNT3+*, *TNNI2+*, *TNNC2+*) and slow (*TNNT1+*, *TNNI1+*, *TNNC1+*) myocytes.

We identified two putative stem/progenitor cell populations in limb muscle (Fig. S2 e-f). One was a cell cluster in the myocyte/myogenic compartment that expressed the human and mouse muscle stem cell (MuSC, or "satellite cell") transcription factors *MYF5* and *PAX7*. These cells also expressed *CD56 (NCAM1)* and *CD82*, cell surface markers used to purify human MuSCs[28,29], as well as *VCAM1* or *ITGA7* used to purify mouse MuSCs[30,31]. A similar population of putative MuSCs (*CD56+ CD82+ VCAM1+ ITGA7+*) was found in the diaphragm. We also identified putative fibroadipogenic progenitors (FAPs), which in humans and mice give rise to fibroblasts and adipocytes (and perhaps chondrocytes and osteoblasts) and promote MuSC-mediated regeneration and sustain the MuSC pool[32–34]. The putative lemur FAPs were found in both limb muscle and diaphragm as stromal populations that selectively expressed *PDGFRA* and *THY1*, surface markers used to purify human FAPs[35] (note that *LY6A* (*SCA-1*), used to purify mouse FAPs[32] is not annotated in the lemur genome). In a companion paper (de Morree et al), we use the identified surface markers to purify and functionally characterize these putative stem/progenitor populations from lemur, and show they exhibit many characteristics more similar to their human counterparts than those of mouse.

From blood, we identified mouse lemur cognates of all the major human and mouse immune cell types including, in the lymphoid lineage, B cells, plasma cells, *CD4+* T cells, *CD8+* T cells, natural killer cells, natural killer T cells, and innate lymphoid cells; and in the myeloid lineage, erythrocytes, platelets, monocytes, macrophages, conventional and plasmacytoid dendritic cells, neutrophils, basophils, and even the rare and fragile eosinophils (Fig. 2). In the bone, bone marrow and other hematopoietic and lymphoid tissues, we identified

bioRxiv preprint doi: https://doi.org/10.1101/2021.12.12.469460; this version posted August 7, 2022. The copyright holder for this preprint (which was not certified by peer review) is the author/funder. All rights reserved. No reuse allowed without permission.

presumptive progenitors including hematopoietic precursors, and progenitors of erythrocytes, megakaryocytes and granulocyte-monocytes and putative adipogenic and osteogenic progenitors. However, certain immune cell subtypes in human and/or mouse were not identified in lemur. For example, lemur monocytes formed a single cluster in most tissues that could not be resolved into classical and non-classical monocytes using the markers that distinguish the two cell types in human (*CD14, CD16*) or mouse (*LY6C1/2*, which has no primate ortholog, *CCR2, CX3CR1*)[36] (also see accompanying Tabula Microcebus manuscript 2). Conventional dendritic cells (cDCs) detected in the lemur analysis could not be divided into type 1 and type 2 subtypes characteristic of humans and mice. Conversely, other dendritic molecular types were identified in lemur (e.g., *FLT3+ IGSF6+* DCs) that had no apparent human or mouse cognates. The full spectrum of developing and mature immune cells across the body allowed us to reconstruct the early stages of hematopoietic development (Section 3), as well as the subsequent dispersal of mouse lemur immune cells throughout the body and its alteration by disease (accompanying Tabula Microcebus manuscript 2).

3. Molecular gradients of cell identity

Although the vast majority of profiled lemur cells could be computationally separated into discrete clusters of cells with similar expression profiles, we found many examples where cells instead formed a continuous gradient of gene expression profiles indicating a gradual transition from one molecular identity to another within the tissue. Some of these reflect a spatial gradient of cell identity in the tissue, whereas others correspond to an ongoing developmental process or the induction of a physiological or pathological cell state.

The kidney provided a dramatic example of spatial gradients of cell types that are key to organ function. Coordinated gradients of renal epithelial and endothelial cell types define the

bioRxiv preprint doi: https://doi.org/10.1101/2021.12.12.469460; this version posted August 7, 2022. The copyright holder for this preprint (which was not certified by peer review) is the author/funder. All rights reserved. No reuse allowed without permission.

position-specific molecular features and functions along the nephron that set fluid and electrolyte balance and other aspects of renal physiology. Among the ~14,800 cells profiled from lemur kidneys, we identified lemur cognates of almost every important cell type known from human and mouse in each of the major tissue compartments. These included cell types of the renal tubule and collecting duct, macula densa cells, and podocytes from the epithelium, and cells of the glomerulus and the vasa recta from the endothelium (Fig. 3 a-f). The only cell types we did not identify were parietal epithelial cells of the glomerulus, renin-secreting juxtaglomerular complex cells, and mesangial cells (see Section 4). However, most notable among the profiled kidney cells were the many epithelial cells that formed a long continuous gradient of molecular identity (Fig. 3 b-c, Fig. S3 a, g-h). With canonical renal markers, we determined that this gradient corresponds to the spatial gradient of epithelial cell types along the mouse lemur nephron, starting from proximal convoluted tubule cells, through the loop of Henle, and ending with principal cells of the collecting duct. Interestingly, macula densa cells, the sodium-sensing cells that regulate glomerular blood flow and filtration rate that are typically physically located at the distal end of the loop of Henle before the start of the distal convoluted tubule[37], surprisingly localized in the lemur molecular cell gradient between cells of the thin and thick loop of Henle. We also found a prominent cell gradient in the endothelial compartment, with arterial markers (*GJA5+*, *BMX+*) expressed at one end of the gradient and venous markers (*ACKR1+*, *VCAM1+*) at the other, and capillary markers (*CA4+*) in between (Fig. 3 d-e, Fig. S3 b, i-j). This appears to comprise the vasa recta, a network of arterioles and venules intermingled with the loop of Henle in the renal medulla, because it expressed some specific vasa recta markers (e.g., *AQP1*, *SLC14A1* for vasa recta descending arterioles) and was molecularly distinct from the clusters of glomerular endothelial cells (*EDH3+*), other capillary endothelial cells (possibly peritubular),

bioRxiv preprint doi: https://doi.org/10.1101/2021.12.12.469460; this version posted August 7, 2022. The copyright holder for this preprint (which was not certified by peer review) is the author/funder. All rights reserved. No reuse allowed without permission.

and lymphatic endothelial cells (*CCL21+*). This deep molecular map of the lemur nephron also revealed region-specific hormonal regulation of nephron function (see accompanying hormone atlas manuscript[38]).

Several other gradients of gradually changing gene expression profiles represent cells differentiating in adult stem cell lineages. Two such gradients observed among immune cell populations of bone marrow represent the ongoing development and maturation of hematopoietic progenitors (Fig. 3 i-j, Fig. S3 d-f, k-l). One gradient bifurcates into the monocyte/macrophage and the granulocyte/neutrophil lineages (accompanying Tabula Microcebus manuscript 2), whereas the other represents the erythroid lineage. Some common but more subtle gradients marked differentiation of basal epithelial cells in the skin and at least four other organs (small intestine, colon, tongue, bladder) into their corresponding mature epithelial cell types along the suprabasal/luminal axis of each organ.

The most striking developmental gradient appeared in the male gonad. Among the ~6500 cells profiled from mouse lemur testes, we found on computational clustering that all except stromal and immune cells formed a single long continuous gradient, which the gene expression profiles indicated was a continuum of germline cells progressing through spermatogenesis (Fig. 3 g-h, Fig. S3c). The gradually changing expression levels of genes across the continuum allowed us to reconstruct the full gene expression program of mouse lemur spermatogenesis, assigning seven canonical stages from stem cells (spermatogonia) to mature spermatids using orthologs of stage-specific markers from human and mouse (see Section 6). In addition to the essential role of male germ cell differentiation in reproduction, the mouse lemur spermatogenesis program is of special interest because such programs are rapidly evolving during primate

bioRxiv preprint doi: https://doi.org/10.1101/2021.12.12.469460; this version posted August 7, 2022. The copyright holder for this preprint (which was not certified by peer review) is the author/funder. All rights reserved. No reuse allowed without permission.

speciation, with several notable evolutionary specializations already recognized for mouse lemur, including seasonal regulation and sperm competition[39].

4. Previously unknown or uncharacterized cell types and subtypes

Although we were able to assign a provisional identity to the vast majority of the cell populations based on expression of orthologs of canonical markers of human and mouse cell types, there were dozens of cases in which more than one cluster in a tissue expressed markers of the same cell type and their separation could not be attributed to technical differences (e.g., cell quality, batch effect, cell doublets) (Fig. 4a). In some cases these appear to be multiple states of the same cell type because the differentially-expressed genes that distinguished the clusters included proliferation markers (e.g., *MKI67, TOP2A)* indicating a proliferative state (hence PF was added to cell type name) or differentiation markers indicating a differentiating state. In most cases, however, the additional clusters appear to represent previously unknown or little characterized cell types or subtypes, and a distinguishing gene (or more) was added to the name of the minor cluster (e.g. B cell (*SOX5+*) in pancreas), or to both clusters if they were similar in abundance. Such clusters were uncovered in all compartments except the germline and in most profiled organs and tissues (Fig. 4a, Fig. 2b).

Fibroblast subtypes were particularly diverse (Fig. 4a). In the lung, we identified adventitial and alveolar fibroblasts, as well as two other clusters of fibroblasts. We also uncovered four molecular subtypes of fibroblasts in bladder, fat, and small intestine, three in kidney, and two in pancreas and tongue, most of which did not have known parallels in human or mouse. Most appear to be organ-specific because there was little co-clustering across organs. Similarly, macrophages formed multiple distinct molecular clusters in many tissues, with substantial diversity within lung, liver, and kidney (Fig. 4a, and accompanying Tabula

bioRxiv preprint doi: https://doi.org/10.1101/2021.12.12.469460; this version posted August 7, 2022. The copyright holder for this preprint (which was not certified by peer review) is the author/funder. All rights reserved. No reuse allowed without permission.

Microcebus manuscript 2). There was also molecular diversity among T and natural killer cells that could not be readily harmonized with classical T cell subtypes defined in humans and mice[40,41].

We also identified interesting molecular subtypes of epithelial cells. These include three molecular types of pancreatic acinar cells (main, *FDX1+*, *PNISR+*) and two pancreatic ductal types (*SPOCK3+*, *UPK1A+*), three types of kidney collecting duct principal cells (main, *FXDY4+*, *KCNE1+*), and two types of small intestine enterocytes (main, *CA2+*) (Fig. 4a). We also found two molecular types of hepatocytes (Fig. 4 b-c): the *APOB+* population expressed higher levels of many classical liver proteins (e.g., apolipoprotein B (*APOB*), fibrinogen gene activator (*FGA*), histidine-rich glycoprotein (*HRG*)) and certain hormones (e.g. angiotensin (*AGT*), *FGF21*) and receptors (glucagon receptor (*GCGR*), hepcidin receptor (*SLC40A1*), androgen receptor (*AR*), growth hormone receptor (*GHR*), and prolactin receptor (*PRLR*)), whereas the *PHYH+* type expressed higher levels of some metabolic genes (e.g. *PHYH*, fatty acid degradation) and methylation regulator (*GNMT)* (Fig. 4c) (see also accompanying hormone atlas paper[38]). The two types do not correspond to the known zonal heterogeneity of human and mouse hepatocytes[42], but notably the *APOB+* hepatocytes expressed more transcripts and genes than *PHYH+* hepatocytes so the *APOB+* cells could correspond to the larger, polyploid hepatocytes and *PHYH+* cells to the smaller, diploid hepatocytes found in human and mouse[43] (Fig. S4). We uncovered a similar molecular distinction among hepatocytes in our mouse scRNA-seq dataset (Fig. S4)[19], indicating these are conserved but previously unrecognized molecular subtypes of hepatocytes.

In the endothelial compartment, there was substantial diversity among blood capillary cells including molecular subtypes found in multiple tissues. *FABP5+ RBP7+* capillary cells

bioRxiv preprint doi: https://doi.org/10.1101/2021.12.12.469460; this version posted August 7, 2022. The copyright holder for this preprint (which was not certified by peer review) is the author/funder. All rights reserved. No reuse allowed without permission.

were found in 10 tissues, *FABP5- RBP7-* cells in seven, variants dubbed *FABP5+ RBP7-* and *FABP5+ RBP7*lo in five and four, respectively, and a *CXCL10+* population in four (Fig. 2b). In some tissues endothelial cells were comprised exclusively of one of these types (e.g. heart, *FABP5+ RBP7+*; brain cortex, *FABP5- RBP7-*; mammary gland, *FABP5+ RBP7*lo), but other tissues (e.g., kidney) contained a mix of two or more (Fig. 2b, Fig. 4a). *FABP5+ RBP7+* capillary cells appear to be specialized for energy storage because they are enriched in genes for fatty acid uptake and binding (e.g., retinol-binding protein 7 (*RBP7*), *FABP1*, *FABP4-like*, *FABP5*), as well as for transcriptional factors *MEOX2* and *TCF15* (Fig. 4d), all genes that are enriched in capillary cells of several high energy-demand tissues in human and mouse[44–47]. *CXCL10+* capillary cells express genes associated with interferon activation (*CXCL9, CXCL10, CX3CLl, GBP1, GBP2, IFIT3*)[48] indicating an inflammatory state in the fat, kidney, and limb muscle of L2 and the lung of L4 (accompanying Tabula Microcebus manuscript 2). We also identified molecular subtypes of lymphatic endothelial cells: *CCL21+* and *CCDC80+* in various tissues and *CCDC80+ ACKR4+* in pancreas (Fig. 4a), perhaps representing different lymphatic cell types in peripheral vessels and lining lymph node sinuses[49–51] (also see accompanying Tabula Microcebus manuscript 2).

For eight of the 768 molecular cell types (~1%) we were unable to assign a specific identity, so they were designated "unknown" along with the organ they were isolated from and the compartment inferred from expression of canonical compartment markers. These include mysterious stromal types in tongue (cell type designation #142) and kidney (#143), and epithelial types in fat (#15) and blood (#16) (Fig. 4 a, e-f, Fig. S5 c-m). The remaining four stromal types, from bone, mammary gland, pancreas, and tongue, were given the same designation (#141, "unknown stromal *NGFR+ TNNT2+*") because they shared similar transcriptomic profiles

bioRxiv preprint doi: https://doi.org/10.1101/2021.12.12.469460; this version posted August 7, 2022. The copyright holder for this preprint (which was not certified by peer review) is the author/funder. All rights reserved. No reuse allowed without permission.

(including high expression of *NGFR*, *IGFBP6*, *OGN*, *ALDH3A1*, *CLDN1*, *ITGB4*) and curiously also expressed high levels of cardiac troponin T (*TNNT2*), a component of the actomyosin contractile apparatus that is a sensitive and specific cardiac myocyte marker used clinically as a diagnostic marker for myocardial infarction[52–54] (Fig. S5 a-e). Some of these unknown cell types (#15, #141, #142) could be specialized mesothelial cells, or at least cells that share features with them, because many of their differentially-expressed genes were enriched in mesothelial cells (Fig. S5 e, j). However, some of the differentially-expressed genes were also expressed by other cell types (e.g. leptomeningeal and Schwann cells for #141 and 142, urothelial cells for #15), and in the global comparison of cell types (Section 5) they did not closely localize with any of these cell types. The unknown kidney stromal type (#143) might be mesangial cells because they expressed high levels of *LMO7* and *ITGA8*, recently reported to be enriched in mouse mesangial cells[55] (Fig. 4 e-f, Fig. S5 f-g). The most perplexing unknown was the epithelial (*EPCAM+*) population from blood (#16) of one individual (L2). It had a unique gene signature including *PGAP1*, *PTPRG*, *FGF13*, *SOX2*, *CPNE6*, *CDH3*, many of which are also expressed by brain ependymal cells, astrocytes, and oligodendrocytes; however, this population did not express canonical markers of those cell types (Fig. S5 k-m).

Some of the molecular subtypes and unknown cell types described above may represent previously unrecognized or sparsely characterized cell states including pathological states (accompanying Tabula Microcebus manuscript 2). Others may be new cell types or subtypes, like the novel lung capillary (aerocyte) and epithelial (ionocyte) populations recently uncovered by scRNA-seq[56–58]. It will be important to characterize each of these potentially novel molecular cell types and determine which are conserved across species but previously unrecognized, and which are mouse lemur or primate innovations.

bioRxiv preprint doi: https://doi.org/10.1101/2021.12.12.469460; this version posted August 7, 2022. The copyright holder for this preprint (which was not certified by peer review) is the author/funder. All rights reserved. No reuse allowed without permission.

5. Global molecular comparison of cell types across the body

To elucidate the molecular relationships of the over 750 defined lemur molecular cell types across the organism identified by our scRNA-seq, we compared and visualized the cell type expression profiles in two ways. Typically such relationships are visualized as 2D representations (e.g., UMAP, tSNE) of expression profiles of all cells, in which the distance between cells (dots) indicates the relatedness of their expression profiles and all cells of a particular type are highlighted in their own color. However, such representations of massive datasets like ours are overly complicated and dominated by the most abundant cell types, obscuring all but the most superficial relationships (Fig. 1g, traditional UMAP of all 244,081 cells colored by tissue, see online portal for UMAP colored by molecular cell type). We found that simplified UMAPs, with each molecular cell type condensed into a single point representing the average expression value of all cells of that type ("pseudo-bulk" expression profile), allowed easy visualization of cell relationships across the entire body (Fig. 5 a-f, Fig. S6). Cell relationships could also be discerned in heatmaps showing pairwise correlation coefficients of all cell type "pseudo-bulk" expression profiles displayed as a large (~750x750) matrix, provided that the molecular cell types were arranged in a biologically sensible order, such as by tissue, compartment, or hierarchical clustering of similarity (Fig. 5 g-h, Fig. S7, https://tabula-microcebus.ds.czbiohub.org/). Both plots revealed global patterns of similarity as well as unexpected cell relationships.

Molecular cell types within a tissue compartment generally showed more related expression profiles, even those from different organs. Endothelial cell types across the body formed the most coherent compartment. Next was the neural compartment including CNS glial cells, which the comparisons showed are surprisingly similar to neurons (Fig. 5 a, g, Fig. S6a).

bioRxiv preprint doi: https://doi.org/10.1101/2021.12.12.469460; this version posted August 7, 2022. The copyright holder for this preprint (which was not certified by peer review) is the author/funder. All rights reserved. No reuse allowed without permission.

Immune compartment cell types were by far the most divergent, and particularly so between lymphoid and myeloid populations. But the global analyses also identified specific cell types that were more closely related to cell types in another compartment than to those in its own compartment. Some of these cross-compartment similarities were predictable. For example, neuroepithelial cells of the airway (neuroendocrine cells) and gut (enteroendocrine cells) were found to be more closely related to neurons and pituitary neuroendocrine cells than to most other epithelial cell types (Fig. 5 a, g, Fig. S7, https://tabula-microcebus.ds.czbiohub.org/). Likewise, proliferating skin intrafollicular cells were more similar to certain proliferative cells in other compartments (e.g., proliferating B cells, T cells, and neutrophils, and erythroid progenitors and skeletal muscle stem cells) than to other non-proliferating epithelial cell types (Fig. 5h); indeed such global comparisons of transcriptomic profiles are a facile way of identifying progenitors and proliferating cell populations.

Other identified cross-compartment similarities were surprising. The most striking was that male germ cells (spermatogonia) are more closely related to immune progenitor cells than to any other cells in the atlas, including progenitors and proliferating cells of other compartments (e.g., intestinal enterocyte progenitors, skin proliferating interfollicular cells, skeletal muscle stem cells) (Fig. 5 a, h). Maturing male germ line cells formed a developmental trajectory emanating out from the immune progenitor cluster just like the various immune cell lineages (Fig. 5a). Differential gene expression analysis showed that this similarity included the common enrichment in both spermatogonia and hematopoietic progenitors of specific cell cycle genes, particularly genes involved in M phase (e.g., *CCNB1*, *VRK1*, *GINS2*, *CEP55*, *BUB1*, *TTK*, *FOXM1*, *CDCA3*, *DEPDC1B*, *SPAG5*, *BRCA1*, *NUDT1*, *CENPS*, *MKI67*, and *DBF4*) (Fig. 5b, Fig. S6b), indicating similarity in the mitotic machinery of proliferating spermatogonia and

bioRxiv preprint doi: https://doi.org/10.1101/2021.12.12.469460; this version posted August 7, 2022. The copyright holder for this preprint (which was not certified by peer review) is the author/funder. All rights reserved. No reuse allowed without permission.

hematopoietic progenitors. Compared to progenitors and proliferating cells of other compartments, spermatogonia and immune progenitors also showed selective expression of non-cell-cycle genes (e.g., *TESMIN, RSPH14, ASB9, ARHGAP15, HEMGN, PLD6, ACAP1, NARF, PHACTR1, PLPPR3, EGFL7, DKC1, LOC105869343* (serine protease 40), *LOC105861000*) (Fig. 5c, Fig. S6c).

Another surprising example of cross-compartment similarity was myelinating and non-myelinating Schwann cells of the peripheral tissues, which segregated with stromal cells and away from other neural compartment cells including non-myelinating Schwann cells of brain cortex (Fig. 5a). Differential expression analysis identified genes enriched in stromal and Schwann cells but not other neural compartment cells (e.g., *COL3A1, LAMC1, SOCS3, COL1A2, COL5A2, ID3, ID1, CDC42EP5, MMP2, TGFBR2, CCN1, TBX3, LOC105874070 (IFITM1-3), LOC105876248*) (Fig. 5d, Fig. S6d) and a complementary set enriched in neurons and CNS glial cells but not the PNS Schwann cells (e.g., *OMG, GPR137C, TCEAL3, MAPK10, ASTN1, NALCN, MAP7, CXXC4*). Many of the genes expressed in common by Schwann and stromal cells are components or regulators of extracellular matrix, suggesting an important and distinctive function of peripheral glia in collaborative remodeling of the extracellular matrix with surrounding stromal cells.

Within a compartment, cells of the same designated type or subtype also generally clustered closely despite their different tissue origins, most notably for endothelial, stromal, neural, and immune compartment cell types and subtypes (e.g., vascular smooth muscle cells, pericytes, mesothelial cells, five types of dendritic cells (conventional, plasmacytoid, mature, *FLT3+ IGSF6+* dendritic cells, and a skin and tongue population), three types of neutrophils (main, *IL18BP+*, *CCL13+*), and two major types of lymphatic endothelial cells (*CCDC80+* and

bioRxiv preprint doi: https://doi.org/10.1101/2021.12.12.469460; this version posted August 7, 2022. The copyright holder for this preprint (which was not certified by peer review) is the author/funder. All rights reserved. No reuse allowed without permission.

CCL21+), and adipocytes (*UCP1*low, *UCP1*high) (Fig. 5 a, f, Fig. S6 e-f). In contrast, epithelial cell types were highly tissue-specific and generally clustered with other epithelial cells from the same organ, even those for which there were cell types of the same designation in another organ (e.g., skin and tongue basal and suprabasal cell types) (Fig. 5e). One example of initially perplexing cross-organ similarity was a distinctive population of epithelial cells from the lung of one individual (L2), which curiously clustered closely with uterine epithelial cells; these were later shown to be lung metastases of a uterine endometrial cancer (accompanying Tabula Microcebus manuscript 2).

6. Evolution of gene expression in primate cell types

To elucidate how gene expression has changed during primate evolution, we compared the transcriptomic profiles of mouse lemur cell types to the corresponding cell types of human and mouse, using mouse as the non-primate outgroup. To ensure comparisons were made across truly homologous cell types and to minimize technical artifacts, we used our own human[20,59] and mouse datasets[18,19] obtained with the same scRNA-seq method and clustered and annotated by canonical markers in a similar way by the same tissue experts. We focused our analysis on lung and on skeletal (limb) muscle cell types for which we had high quality profiles and annotations from all three species. Our assignments of homologous cell types were verified by SAMap analysis (Fig. S8 a, c), which uses a self-assembling manifold algorithm and graph-based data integration to identify homologous (reciprocally-connected) cell types with shared expression programs across species[25], and also by showing that the corresponding cell types from the three organisms co-clustered when their expression profiles were adjusted by BBKNN batch correction[60] and compared and displayed by dimensionality reduction (Fig. S8 b, d). We restricted the analysis at the gene level to the 13,302 one-to-one-to-one gene orthologs across all

bioRxiv preprint doi: https://doi.org/10.1101/2021.12.12.469460; this version posted August 7, 2022. The copyright holder for this preprint (which was not certified by peer review) is the author/funder. All rights reserved. No reuse allowed without permission.

three species that we curated by assigned gene names from the ENSEMBL and NCBI databases (Table 4).

For each cell type, we computed the Xi correlation[61] of the expression profiles of 1000 trios of randomly-selected cells from human, lemur, and mouse, and then calculated the difference in correlation values between each pair of species. We found that the transcriptomic profiles of most lemur lung cell types analyzed (13 of 22, 59%) were significantly more similar to the homologous cell type of human than to that of mouse (e.g. ciliated cells, plasma cells, capillary aerocytes), although the degree of divergence from mouse varied by cell type (Fig. 6a). For five lung cell types (5 of 22, 23%), the lemur expression profile was equally similar to both. Surprisingly, the profiles of the other lemur lung cell types analyzed (alveolar macrophages and proliferating macrophages, NK T cells, CD4+ T cells) were significantly more similar to the corresponding mouse cell type than to the human, suggesting a high degree of evolutionary adaptation in gene expression for those cell types in the human lineage. Likewise, we found that the expression profiles of human and mouse lung lymphatic endothelial cells and CD8+ T cells were more similar to each other than to the corresponding cell types in lemur, suggesting a high degree of evolutionary adaptation in gene expression in those two cell types in the lemur lineage. The patterns of evolutionary adaptation in cell type gene expression varied substantially even within a compartment. For example, the recently identified capillary endothelial “aerocytes” that mediate alveolar gas exchange[56] showed among the highest degree of primate specialization of any lung cell type, whereas arterial and venous endothelial cells showed similar divergences across all three species and lymphatic endothelial cells showed the highest degree of lemur specialization. Likewise in the lymphoid compartment, plasma cells showed among the highest degree of primate specialization of any cell type, whereas B cells (from which plasma cells arise)

bioRxiv preprint doi: https://doi.org/10.1101/2021.12.12.469460; this version posted August 7, 2022. The copyright holder for this preprint (which was not certified by peer review) is the author/funder. All rights reserved. No reuse allowed without permission.

showed only limited primate specialization, and CD4+ T cells showed the highest degree of human specialization and CD8+ T cells among the highest degree of lemur specialization. The same cross-species comparison of limb (skeletal) muscle cell types gave similar results, although 40% (4 of 10) of the analyzed lemur cell types were closer to the corresponding mouse cell type than to the human, and nearly all human cell types (80%, 8 of 10) were closer to the corresponding lemur cell type and none were closer to those of mouse (Fig. S8e). Interestingly, although human muscle *CD8+* T cells were more similar to those in lemur, human lung *CD8+* T cells were more similar to those in mouse, suggesting potential species differences in organ-specific influences on *CD8+* T cells. Thus, expression patterns of each cell type have apparently changed at different rates and to different degrees during primate evolution, including cell types in the same compartment as well as related cell types in different organs.

To provide molecular insight into these cell type specializations in primate evolution, we identified for each of the lung and muscle cell types the genes with expression levels in lemur and human substantially differ from those in mouse (>10-fold difference, $p < 1e\text{-}5$). These included general primate differences (both lemur and human vs mouse) as well as lemur-specific and human-specific differences (Table 5, Fig. S9). Dozens of genes showed such primate-specific expression patterns for each cell type (58±31, mean±SD; range 11 - 113 genes for each lung cell type; 57±30, range 11 - 103 genes for each muscle cell type), many of which are selectively expressed in the cell type or its compartment and serve canonical functions (Fig. 6b). Examples for lung include genes involved in immune (*PIGR, CXCL17*) and stem/progenitor (*RASGRF1, ERBB3*) functions of alveolar type 2 (AT2) cells; cilia structure (*SPATA4, WDR38, WDR54*)[62,63] and mucin production genes (*MUC20*) of ciliated cells; extracellular matrix genes (*LUM, DCN, SGCA*) in stromal compartment cell types (adventitial and alveolar fibroblasts,

bioRxiv preprint doi: https://doi.org/10.1101/2021.12.12.469460; this version posted August 7, 2022. The copyright holder for this preprint (which was not certified by peer review) is the author/funder. All rights reserved. No reuse allowed without permission.

pericytes); pore forming cytolytic protein (*PRF1*), granzyme M (*GZMM*), and other immune-related genes (*PTGDR, KLF12, TIGIT*) in T and NK cells; and bacterial receptor *CD163*, *OSCAR*, and other immune-related genes (*CXCL16, IL7R, MSR1, PTAFR, RAB20, VSIG4*) in monocytes and macrophages.

Other genes enriched in primate cell types suggest primate-specific communication between cell types. For example, the classical vasopressor angiotensin II can target pericytes of lung and muscle via its receptor *AGTR1*, and vasoactive intestinal peptide (VIP) can target vascular endothelial cells of lung (but not those of muscle) via its receptor *VIPR1*. Also, insulin growth factor signaling can originate from lymphatic cells via the ligand *IGF1*, and Hedgehog signaling can be modulated in the lung by AT2 cell expression of the secreted inhibitor *HHIP*, implicated in chronic obstructive pulmonary disease (COPD)[64]. We also identified many genes that were more broadly expressed in the lung and showed primate-specialization across many or all lung cell types (e.g., *ABHD2, BTG3, GNG7, KCNA3, TYMP*) (Fig. 6b, Fig. S9a, Table 5); many of these were also broadly expressed and primate enriched in muscle (Table 5, Fig. S9g). The complementary analysis of genes highly enriched in mouse cell types relative to the corresponding primate cell types identified hundreds of such genes (Fig. S9b, Table 5), suggesting that cell type gain of expression in the mouse lineage (or loss in the primate lineage) also contributed substantially to primate-specific patterns of gene expression.

We also compared the lemur spermatogenesis program (Section 3) with the corresponding expression programs recently elucidated in human and mouse[65–67]. Many of the marker genes that demarcate canonical stages of spermatogenesis are similarly expressed in all three species (e.g., *KIT, SOHLH1*, spermatogonia; *SYCP3*, early spermatocytes; *ACR*, pachytene/diplotene spermatocytes; *TNP1*, early/mid spermatids; *GAPDHS*, mid/late spermatids;

bioRxiv preprint doi: https://doi.org/10.1101/2021.12.12.469460; this version posted August 7, 2022. The copyright holder for this preprint (which was not certified by peer review) is the author/funder. All rights reserved. No reuse allowed without permission.

Fig. 6c), defining a conserved core program of mammalian spermatogenesis. However, our analysis also identified primate-specific features of the program. Dozens of "primate-only" genes (orthologs identified in human and mouse lemur but missing in mouse) are selectively expressed during spermatogenesis, indeed these were the dominant class of "primate-only" genes (accompanying Tabula Microcebus manuscript 2). We also uncovered genes that have undergone heterochronic changes in expression such that orthologous genes are expressed at different stages of the male germ cell differentiation program in different species, indicating re-wiring of aspects of the spermatogenesis program during evolution. Examples include *NME8*, which peaks in expression in pachytene spermatocytes of primates but in early spermatids of mice; *ID4*, which is expressed only in spermatogonia for primates but continues to be expressed in spermatocytes for mice; *GFRA1*, which is expressed in spermatogonia of all species but re-expressed in late spermatocytes and spermatids of primates (Fig. 6c); and the chromosome-wide down regulation of X-chromosome genes (meiotic sex chromosome inactivation, MSCI)[68] that occurs in pre-pachytene spermatocytes in primates (Fig. 6e) but pachytene spermatocytes in mouse[69]. One lemur-specific heterochronic change is in expression of *PIWIL1* (also known as MIWI in mice), a repressor of retrotransposons during meiosis[70]. In both humans and mouse the gene is expressed throughout meiosis from early spermatocytes to diplotene and even in secondary spermatocytes with peak expression in pachytene spermatocytes[71,72]. In contrast, *PIWIL1* expression in lemur was restricted to early spermatocytes, with reduced expression in pachytene spermatocytes (Fig. 6 c-d). Lemur-specific specializations like this in the spermatogenesis program are of particular interest because of their potential role in the remarkable radiation of the Lemuroidea clade (over 100 lemur species, nearly one-quarter of all primate species), and because several notable evolutionary specializations have already been recognized for mouse

bioRxiv preprint doi: https://doi.org/10.1101/2021.12.12.469460; this version posted August 7, 2022. The copyright holder for this preprint (which was not certified by peer review) is the author/funder. All rights reserved. No reuse allowed without permission.

lemur, including the dramatic seasonal regulation of the testes and the role of sperm competition in reproduction[39].

One particularly prominent set of lemur specializations we uncovered in the spermatogenesis program was in the small subset of X-chromosome genes that become active after MSCI, ones that 'escape' postmeiotic sex chromatin silencing[73–75]. We identified 62 such 'escape' genes in mouse lemur by searching among X-chromosome genes for ones that are highly expressed selectively in the early spermatid stage (Table 6, Fig. 6f), as done for mouse and human spermatogenesis[74,75]. Remarkably, 49 (79%) of the identified lemur 'escape' genes were unique to lemur, whereas only 3 (5%) were conserved across all three species (testes-specific histone variant *HYPM* (H2A.P), scaffold protein *AKAP4* required for sperm flagella function and fertility in mouse, and uncharacterized protein *CXHXorf65*), 8 (13%) were shared only with human, and 2 (3%) were shared only with mouse (Table 6, Fig. 6f).

Extending such comparisons to all homologous cell types and more broadly across phylogeny may provide insight into the selection pressures that underlie the evolutionary differences among cell types. Even at this stage the three-way comparisons (lemur, human, mouse) described here suggest interesting biological hypotheses and identify many cell types and genes for which lemur provides a human modeling advantage over mice.

bioRxiv preprint doi: https://doi.org/10.1101/2021.12.12.469460; this version posted August 7, 2022. The copyright holder for this preprint (which was not certified by peer review) is the author/funder. All rights reserved. No reuse allowed without permission.

DISCUSSION

Our single cell RNA-sequencing and analytical pipeline defined over 750 mouse lemur molecular cell types and their expression profiles, comprising nearly all major cell types for most (27) tissues. The cell types include cognates of most canonical human cell types plus stem and progenitor cells and their developmental programs for spermatogenesis, hematopoiesis, and other adult tissues, many of which did not form discrete molecular types but merged into continuous gradients of cell intermediates along the developmental pathway. Biologically-guided expert curation also uncovered dozens of previously unidentified or little characterized cell types and subtypes, some of which appear to be conserved (e.g., two types of hepatocytes, several capillary types specialized for energy storage or activated by inflammation) but others may be primate or lemur-specific innovations.

By organizing the mouse lemur cell types by organ, compartment, and function, and then globally comparing their expression profiles in a simplified UMAP or matrix of all pairwise comparisons, we defined the molecular relationships of cell types across the body. This revealed global features like the high similarity of cell types within some compartments (e.g., endothelial) but marked divergence of cell types in others (e.g., immune), as well as the surprising similarity of a few cell types across compartments, such as spermatogonia to hematopoietic progenitors and peripheral glia to stromal populations.

The atlas provides a broad cellular and molecular foundation for studies of this emerging primate model organism. Although the first steps in establishing a new model organism have traditionally been mutant screens and generation of a genetic map or reference genome, with the technological advances and declining cost of scRNA-seq the creation of a reference transcriptomic cell atlas like ours can now be prioritized. It comprehensively defines cell types

bioRxiv preprint doi: https://doi.org/10.1101/2021.12.12.469460; this version posted August 7, 2022. The copyright holder for this preprint (which was not certified by peer review) is the author/funder. All rights reserved. No reuse allowed without permission.

and aids elucidation of their functions (accompanying muscle stem cell manuscript), and allows molecular comparisons of mouse lemur cell types to each other and to their orthologs in human and mice, allowing exploration of primate biology and evolution at cellular resolution. This revealed cell type specific patterns of primate cell specialization even within a single organ and compartment, and identified the many cell types for which mouse lemur provides a human modeling advantage over mice, as well as cases like sperm with a multitude of primate- and lemur-specific expression innovations. But the atlas also provides a powerful new way of detecting genes, defining their structures and splicing, and assigning their function, as well as elucidating organism-wide processes such as hormonal signaling, immune cell activation and dysregulation, and primate-specific physiology, diseases, and genes, as we show in the accompanying papers (accompanying Tabula Microcebus manuscript 2; hormone atlas[38]).

Our cell atlas strategy can be adapted to other emerging model organisms. This strategy should include the opportunistic identification of donors and systematic procurement of tissues from each; application of the scRNA-seq technologies and analytical pipeline including computational cell clustering, integration, and expert cell annotation; and the biological organization of cell types and comparisons across the organism and between organisms. Importantly, extensive clinical and histopathological metadata should be collected from each donor and tissue to mitigate against complexities arising from genetic and environmental differences, as this can provide insight into individual-specific features of the atlas, as we exploit in the accompanying paper (Tabula Microcebus manuscript 2). Application of this strategy to a wide variety of organisms[76–79] will rapidly expand our cellular, genetic, and molecular understanding of biology that has been dominated for a half century by a small number of model organisms.

bioRxiv preprint doi: https://doi.org/10.1101/2021.12.12.469460; this version posted August 7, 2022. The copyright holder for this preprint (which was not certified by peer review) is the author/funder. All rights reserved. No reuse allowed without permission.

ACKNOWLEDGMENTS

This work was supported by funding from The Chan-Zuckerberg Biohub, Howard Hughes Medical Institute and Vera Moulton Wall Center for Pulmonary Vascular Disease; unrestricted grant from Research to Prevent Blindness and NEI P30-EY026877 to the Stanford Department of Ophthalmology to Albert Y. Wu; The Hong Kong University of Science and Technology start-up grant R9364, The Hong Kong University of Science and Technology Big Data for Bio Intelligence Laboratory (BDBI), and The Chau Hoi Shuen Foundation (R9056) to Angela Wu; NSF-DBI-1701984 to Anne D. Yoder; funding from Developmental and Stem Cell Biology Graduate Program to Aris Taychameekiatchai; funding from Hong Kong Research Grant Council (16307818, 16301419, 16308120, 16307221, C6021-19E), the Hong Kong University of Science and Technology (startup grant R9405), and The Hong Kong University of Science and Technology Big Data for Bio Intelligence Laboratory (BDBI) to Can Yang; funding from Shanghai Sailing Program to Jingsi Ming (21YF1410600); NIA 1K99AG066963 to Thomas Ambrosi; NIH DP2AI138242 to Iwijn De Vlaminck; National Sciences and Engineering Research Council of Canada fellowship PGS-D2 to Michael F.Z. Wang; NIH R35 GM139517, R01 GM116847, R35 GM139517, NSF MCB1552196 to Julia Salzman; NSF Graduate Research Fellowship DGE-1656518 and a Stanford Graduate Fellowship to Julia Olivieri; Cancer Systems Biology Scholars Fellowship (Grant R25 CA180993) and Clinical Data Science Fellowship (Grant T15 LM7033-36) to Roozbeh Dehghannasiri; Urology Care Foundation Research Scholar Award Program and AUA Western Section Research Scholar Fund II to Hosu Sin; Stanford Graduate Fellowship/HHMI/NIH CMB Training Grant to Yue Zhang; American Cancer Society Postdoctoral Fellowship to SoRi Jang; Walter V. and Idun Berry Postdoctoral Fellowship to Andrea R. Yung; NSF Graduate Research Fellowship and Stanford Graduate Fellowship to

bioRxiv preprint doi: https://doi.org/10.1101/2021.12.12.469460; this version posted August 7, 2022. The copyright holder for this preprint (which was not certified by peer review) is the author/funder. All rights reserved. No reuse allowed without permission.

Youcef Ouadah; the Wu Tsai Neurosciences Institute Interdisciplinary Scholar Award to Shixuan Liu; European Community's 7th Framework Programme (FP7/2007-2013) under grant agreement Nbr 278486 (DEVELAGE), from the Fonds Unique Interministériel and Région Languedoc-Roussillon under grant agreement Nbr 110284 (DiaTrAl), and from the Fondation Plan Alzheimer (PRADNET) to Jean-Michel Verdier and Corinne Lautier; NIH R01 AI024258 to Peter Parham and Lisbeth A. Guethlein; NIH R01DC016892 to Wan-Jin Lu; NIH P30DK116074 to Yan Hang; NSF Graduate Research Fellowship to Connor V. Duffy; Postdoctoral Fellowships from the DFG (NE 2006/1-1) and California TRDRP (25FT-0011) to Patrick Neuhöfer; funding from Independent Research Fund Denmark (DFF–5053-00195) and Lundbeck Foundation (R232-2016-2459) to Jean Faru; NIH AG068667, AR073248 and AG036695 to Thomas A. Rando; funding from Wu Tsai Neurosciences Institute to Tony Wyss-Coray; NSF BCS 0647402 to Liza Shapiro and E. Christopher Kirk.

bioRxiv preprint doi: https://doi.org/10.1101/2021.12.12.469460; this version posted August 7, 2022. The copyright holder for this preprint (which was not certified by peer review) is the author/funder. All rights reserved. No reuse allowed without permission.

METHODS

Animal husbandry

Microcebus murinus gray mouse lemurs originated from the closed captive breeding colony at the Muséum National d'Histoire Naturelle in Brunoy, France, and transferred to the University of Texas (Austin) and then Stanford University and maintained for noninvasive phenotyping and genetic research as approved by the Stanford University Administrative Panel on Laboratory Animal Care (APLAC #27439) and in accordance with the Guide for the Care and Use of Laboratory Animals, as detailed in Casey et al.[21]. Briefly, mouse lemurs were individually or group housed indoors in an AAALAC-accredited facility in a temperature (24°C) and light-controlled environment (daily 14:10 h and 10:14 h light:dark alternating every 6 months to stimulate photoperiod-dependent breeding behavior and metabolic changes) with perches and nest boxes, and were fed fresh fruits and vegetables, crushed primate chow plus live insect larvae as enrichment items. Health and welfare were routinely monitored and clinical care provided by the Veterinary Service Center.

Tissue procurement and processing

Animals in declining health that did not respond to standard therapy were euthanized by pentobarbital overdose under isoflurane anesthesia as described in Casey et al.[21]. Prior to euthanasia, a veterinary examination was performed, and animal body weight and electrocardiogram (ECG) were obtained (KardiaMobile 6L, AliveCor). Blood was immediately collected via cardiocentesis for serum chemistry, complete blood count, biobanking, and single cell RNA-sequencing. In three animals (L2, L3, and L4), transcardial perfusion of the lungs with phosphate buffered saline (PBS) was done to reduce circulating cells. Organs and tissues were sequentially removed and divided by a veterinary pathologist. One sample of each tissue was

bioRxiv preprint doi: https://doi.org/10.1101/2021.12.12.469460; this version posted August 7, 2022. The copyright holder for this preprint (which was not certified by peer review) is the author/funder. All rights reserved. No reuse allowed without permission.

immediately placed in formalin fixative for histopathology[21], and a second was embedded in Optimal Cutting Temperature compound (OCT) and then flash frozen on dry ice and stored at -80°C for biobanking. A third sample was placed directly in cold (4ºC) PBS pH 7.4 and immediately distributed to the tissue expert for cell dissociation and preparation for scRNA-seq as detailed below. Additional diagnostics such as microbiological cultures were performed where clinically indicated. The entire necropsy was completed within 1-2 hrs, with ischemia-sensitive tissues prioritized as described in Supplementary Methods.

Histological and pathological analysis

Tissues were immersion-fixed in 10% neutral buffered formalin for 72 hours. Formalin-fixed tissues were processed routinely, embedded in paraffin, sectioned at 5 µm, and stained with hematoxylin and eosin (H&E). Tissues included the following: heart, aorta, lungs, trachea, thyroid gland, parathyroid gland, kidneys, urinary bladder, male reproductive tract (testicle, epididymis, seminal vesicle, prostate, and penile urethra), female reproductive tract (uterus, cervix, vagina, and ovaries), salivary glands, tongue, epiglottis, esophagus, stomach, small and large intestine, liver (with gallbladder), adrenal gland, spleen, lymph nodes, white adipose, brown adipose, bone, spinal cord, eyes, and bone marrow. Selected tissues stained with Von Kossa (for mineralization), Masson's trichrome (for collagen), Congo Red (for amyloid), and Gram stain (for bacteria) as part of the pathological analysis. H&E stained slides were scanned with a Leica Aperio AT2 High Volume Digital Whole Slide Scanner (40x objective), uploaded into Napari image viewer[80], software adapted by CZB, and posted on the Tabula Microcebus portal https://tabula-microcebus.ds.czbiohub.org/.

bioRxiv preprint doi: https://doi.org/10.1101/2021.12.12.469460; this version posted August 7, 2022. The copyright holder for this preprint (which was not certified by peer review) is the author/funder. All rights reserved. No reuse allowed without permission.

Preparation of single cell suspensions and FACS-sorting for scRNA-seq

Fresh tissue samples procured as described above were placed on ice, received by organ/tissue experts and immediately dissociated and processed into single cell suspensions, except for samples from L3, which were kept cool overnight after necropsy and processed the next morning (see Supplementary Methods). For each solid tissue, this involved a standard combination of enzymatic digestion and mechanical disruption methods that were optimized for the specific tissue, many of which were adapted from procedures used for the corresponding mouse tissue[18,19]. For blood, immune cells were isolated using a high density ficoll gradient (Histoplaque-1119, Sigma-Aldrich) to include peripheral blood mononuclear cells (PBMCs) and polymorphonuclear leukocytes (PMNs)[20].

The specific protocols for each of the 27 tissues are detailed in Supplementary Methods. Cell number and concentration for each single cell suspension were determined by manual counts using a hemocytometer, and then adjusted with 2% fetal bovine serum (FBS) in PBS to a target concentration of about 10^6 cells/mL. Samples were then used for droplet-based 10x library preparation and/or flow sorted for single live cells (Sytox blue negative; ThermoFisher S34857) for plate-based Smart-seq2 library preparation. To enrich for cardiomyocytes, the standard procedure for cardiac cell isolation was supplemented by hand-picking cardiomyocytes (Supplementary Methods). Residual cell suspensions were diluted 1:1 with serum-free Bambanker cell freezing media (GC Lymphotec #BB01) and cryopreserved at -80°C.

scRNA-seq library preparation, quality control, and sequencing

For 10x, single cells were profiled using the 10x Genomics single cell RNA-sequencing pipeline (Chromium Single Cell 3’ Library and Gel Bead v2 Chemistry kit) and sequenced on a NovaSeq 6000 System as previously described[18–20] and detailed in Supplementary Methods. For

bioRxiv preprint doi: https://doi.org/10.1101/2021.12.12.469460; this version posted August 7, 2022. The copyright holder for this preprint (which was not certified by peer review) is the author/funder. All rights reserved. No reuse allowed without permission.

SS2, single cells were sorted into 384- or 96-well lysis plates, reverse transcribed to complementary DNA (cDNA) and amplified, as previously described[18,19]. cDNA libraries were prepared using the Nextera XT Library Sample Preparation kit (Illumina, FC-131-1096) or (for L4) an in-house protocol detailed in Supplementary Methods; no significant differences between protocols were observed in library read depth or quality. Pooling of individual libraries and subsequent quality control and DNA sequencing were done as previously described[18–20] with minor modifications (Supplementary Methods).

Genome alignment of scRNA-seq sequencing reads and gene counts

Microcebus murinus genome assembly (Mmur 3.0) with NCBI annotation release 101 (date acquired, September 21, 2018) was used for downstream alignment and data analysis. A total of 31,509 genes were detected, including annotated genes and unannotated loci but excluding mitochondrial and Y-chromosome genes (unannotated at our acquisition date).

For 10x samples, downstream data was processed by standard methods using Cell Ranger (version 2.2, 10x Genomics). Raw base call (BCL) files directly generated by the NovaSeq were demultiplexed and converted to FASTQ files, and then aligned to the 10x genome index, with barcode and UMI counting performed to generate a gene counts table. Alignment files were outputted in standard BAM format.

For SS2 samples, demultiplexed fastq files were mapped to the genome using STAR aligner (version 2.6.1a). Briefly, the genome FASTA file was augmented with ERCC sequences to create a STAR genome index with 99 bp overhangs (optimized for Illumina 2 x 100 bp paired-end reads). Two-pass mapping was executed, with specific STAR options and parameters detailed in Supplementary Methods.

bioRxiv preprint doi: https://doi.org/10.1101/2021.12.12.469460; this version posted August 7, 2022. The copyright holder for this preprint (which was not certified by peer review) is the author/funder. All rights reserved. No reuse allowed without permission.

Contamination filtering of 10x data

We performed stringent contamination filtering to resolve cross-sample contamination in an Illumina sequencing run caused by cell barcode hopping among multiplexed 10x samples[81]. Such cross-sample contamination can occur when low levels of ambient mRNA containing the 10x cell barcode in one sample gets added onto the transcript of other samples during Illumina sequencing amplification, resulting in the incorrect assignment of a cell barcode to other samples; hence in subsequent analyses, a cell from one tissue could falsely appear as multiple cells from different tissues (samples). To exclude such artifacts, for each sequencing run we identified all cell barcodes that were assigned to multiple samples, and for each such barcode identified we compared the number of UMIs in each sample. If there was one dominant sample index (i.e., number of UMIs of the dominant sample was 10 times or more greater than that of the second most abundant sample), then the cell with the dominant sample index was kept (but labeled in its metadata as 'potentially contaminated') whereas all other instances of that "cell" were removed. If there was no dominant sample index, then all instances of the "cell" with that barcode were removed from the dataset. (This was not an issue for SS2 samples because they were sequenced using dual unique indices for each cell.)

Cell clustering, annotation, and cluster markers from scRNA-seq profiles

Step 1 - Cell clustering and annotation of each tissue processed by 10x. Transcriptomic profiles of cells from each tissue from each individual lemur were clustered separately using Seurat software package (version 2.3.0) for R studio (version 3.6.1). We included in this step all cells with >100 genes or >1000 UMIs detected, a minimal threshold that was used to ensure inclusion of all cell types including ones in which the cells (or RNA) were unstable (see below for more stringent criteria used for final cell quality control). For each cell, expression of a gene

bioRxiv preprint doi: https://doi.org/10.1101/2021.12.12.469460; this version posted August 7, 2022. The copyright holder for this preprint (which was not certified by peer review) is the author/funder. All rights reserved. No reuse allowed without permission.

g is normalized in 10x data as: $\ln(UMI_g/UMI_{total} *1e4 +1)$, abbreviated as ln(UP10K+1); in SS2: $\ln(reads_g/reads_{total} *1e4 +1)$, abbreviated as ln(CP10K+1). Next, data scaling, dimensionality reduction (PCA), clustering, and visualization (t-SNE, UMAP) were performed following the standard Seurat pipeline as previously described[20] with parameters including the numbers of principal components, perplexity, and resolution adjusted manually for each iteration of cell clustering. Resultant cell clusters were manually assigned to a compartment (endothelial, epithelial, stromal, lymphoid, myeloid, megakaryocyte-erythroid, neural, germ) based on expression of the mouse lemur orthologs of canonical marker genes for each compartment in human and mouse (see Table S2). Clusters expressing markers from more than one compartment were annotated as "doublets." Cells within each assigned compartment were then subclustered, repeating the data processing steps above, and then the clusters in each compartment were annotated separately. To annotate (determine) the cell type of each cluster, a list of canonical human and mouse gene markers for each cell type in each tissue was curated from the literature (Table S2), including genes previously validated by in situ hybridization and/or immunohistochemistry as well as differentially-expressed genes culled from recent scRNA-seq studies, and the orthologous mouse lemur genes were identified and their expression visualized on the t-SNE plots. Based on the enriched expression of marker genes, each cluster of cells within a compartment was manually assigned a cell type identity. Clusters that contained more than one cell type were further subclustered to better resolve the cell types. Cell types represented by only a small number of cells that did not form a separate cluster were manually curated, aided by the cellxgene gene expression visualization tool[82] as detailed below.

Each cluster was assigned both a 'cell ontology' cell type designation using the standardized and structured nomenclature[24], and a 'free annotation' that resolves biologically

bioRxiv preprint doi: https://doi.org/10.1101/2021.12.12.469460; this version posted August 7, 2022. The copyright holder for this preprint (which was not certified by peer review) is the author/funder. All rights reserved. No reuse allowed without permission.

significant clusters not contained in the current cell ontology. Free annotations were assigned as follows. In cases where a smaller cluster stemmed off a larger ("main") cluster in t-SNE embedded space, the smaller cluster was distinguished with one or more differentially-expressed genes added to the cell type name (e.g. B cell (*SOX5+*) clustered near the main population of B cells in the pancreas); differentially-expressed genes driving the subtype clustering were ascertained by Wilcoxon rank-sum tests. In cases where two approximately equal-sized clusters separated on the t-SNE plot, a marker gene was added to the cell type name for both clusters (e.g. hepatocyte (*APOB+*) and hepatocyte (*PHYH+*) in the liver). Clusters with a small number of cells that contained more than one cell type but could not be partitioned into separate clusters by subclustering with the Louvain algorithm or manually with cellxgene (see step 3) were labeled as a 'mix' cell type (e.g. the cluster labeled 'endothelial cell' in the uterus contains a mixture of artery, vein, and capillary cells). Clusters with cells that expressed markers for more than one cell type and it was biologically plausible they were not a technical artifact (e.g., doublet of two distinct cell types) were labeled as a 'hybrid' cell type (e.g. the cluster labeled as 'monocyte/macrophage' in the trachea contains cells that expressed markers of both cell types and could not be further distinguished based on current molecular definitions of these cell types). After examining the human/mouse markers for all known cell types in a tissue, clusters that could not be assigned a cell type were labeled 'unknown,' with the tissue, compartment, and one or more differentially-expressed genes added to the cell type name (e.g. 'unknown_Bone_stromal_G1 (*NGFR+ TNNT2+*)' are bone stromal cells that do not correspond to any extant stromal cell type reported for human and mouse). To detect the differentially-expressed genes of an unknown cell type, we compared the unknown cell type to all other cells of the same compartment and tissue (see Fig. S5). Clusters containing a majority of cells that

bioRxiv preprint doi: https://doi.org/10.1101/2021.12.12.469460; this version posted August 7, 2022. The copyright holder for this preprint (which was not certified by peer review) is the author/funder. All rights reserved. No reuse allowed without permission.

expressed cell proliferation markers (e.g. *TOP2A, MKI67, STMN1*) were appended the abbreviation "PF." Clusters that separated from a main cluster but did not express any distinguishing markers and differed only in parameters of technical quality (i.e. fewer genes and counts detected per cell) were considered low quality and "LQ" was appended to the cell type name.

After annotations were assigned, the cutoff for the minimum number of genes per cell was increased from 100 to 500 and only the qualifying cells were further analyzed. For most tissues, this more stringent cutoff only resulted in removal of some erythrocytes and neutrophils; the only exception were cardiac cardiomyocytes, most of which expressed fewer than 500 genes per cell so separate filtering criteria were applied (see Supplementary Methods).

Step 2 - Annotation of each tissue processed by SS2. Cells processed by the SS2 protocol with <500 genes or <5000 reads were excluded from further analysis, and gene expression levels in the remaining cells were scaled and log transformed as described above for the 10x datasets. Cells from a particular tissue and individual were integrated with the 10x dataset of the same tissue and individual into the same UMAP embedded space using the FIRM algorithm (detailed below). Cells from SS2 were automatically annotated with the same label as the nearest neighboring 10x cell. Annotations were manually verified in Step 3 aided by cellxgene gene expression visualization. SS2 datasets for which there were no corresponding 10x dataset from the same individual/tissue were manually annotated using the method described in Step 1 for 10x datasets.

Step 3 – Integration of datasets across individuals. For each tissue, the combined 10x/SS2 datasets from each individual were further integrated into the same UMAP embedded space using the FIRM algorithm[23]. This step resulted in 27 separate tissue UMAPs, each

bioRxiv preprint doi: https://doi.org/10.1101/2021.12.12.469460; this version posted August 7, 2022. The copyright holder for this preprint (which was not certified by peer review) is the author/funder. All rights reserved. No reuse allowed without permission.

containing data from up to 4 individuals. To ensure consistency of cell type labeling across all individuals, annotations were verified and adjusted manually using cellxgene, an interactive tool to visualize and annotate single cell RNA-sequencing data (https://chanzuckerberg.github.io/cellxgene/)[82].

Step 4 – Integration of datasets across tissues. All 27 tissue-level objects were integrated into a single UMAP embedded space using the FIRM algorithm. As above, annotations were verified/adjusted manually in cellxgene to ensure consistency of cell designations across all tissues. In most instances, each cell type clustered separately, irrespective of the tissue of origin, and the same designation was used across all tissues. Occasionally, similar cells types (e.g. fibroblasts, macrophages) clustered separately by tissue of origin, making it challenging to distinguish whether the separation was due to tissue-level batch effect or because of true biological differences. In these cases, the original tissue-level annotation label was kept for each cluster.

Step 5 – Detect differentially-expressed genes for each cell type. We calculated the top 300 differentially-expressed genes (adjusted p-value<0.05) for each cell type in the 10x dataset (represented by at least 5 individual cells, after removing doublets, low quality, and mixed cell types) using the Wilcoxon rank-sum test with Benjamini-Honchberg FDR correction (Table 3). We compared each cell type to: (i) all other cell types from the same tissue (e.g., capillary cell type of the lung compared to all other lung cell types, 'tissue-wide' comparison), (ii) all other cell types from the same compartment of that tissue (e.g., capillary cell type of the lung compared to all other lung endothelial cell types, 'tissue-compartment-wide' comparison), (iii) all other cell types from the atlas (capillary cell type of the lung to all other cells in the atlas, 'atlas-wide' comparison), (iv) all other cell types from the same compartment across the atlas

bioRxiv preprint doi: https://doi.org/10.1101/2021.12.12.469460; this version posted August 7, 2022. The copyright holder for this preprint (which was not certified by peer review) is the author/funder. All rights reserved. No reuse allowed without permission.

(capillary cell type of the lung to all other endothelial cell types in the atlas, 'atlas-compartment-wide' comparison).

FIRM integration

FIRM is a newly developed algorithm that integrates multiple scRNA-seq datasets[23] (e.g., from different sequencing platforms, tissue types, and experimental batches). In brief, FIRM optimizes dataset integration by computing the dataset-specific scale factors for gene-level normalization. Different datasets generally have varied cell-type compositions, resulting in dataset disparity when scaling the gene expression levels to unit variance for each dataset. Different from classical scaling procedures, FIRM computes the scale factors based on subsets of cells which have matched cell-type compositions between datasets. To construct these subsets, FIRM detects paired clusters between datasets based on similar overall gene expression and then samples the cells so that paired cell types have the same proportional representation in each dataset. Parameters used for integration are given in Supplementary Methods. The integrated datasets generated using FIRM show accurate mixing of shared cell-type identities and preserve the structure of the original datasets, as confirmed by expert manual inspection during cell annotation.

Trajectory analysis

We developed a custom in-house program in Matlab to detect and characterize spatial and developmental pseudotime cell trajectories, which were similar but noisier when analyzed with existing programs such as Monocle 3 (https://github.com/cole-trapnell-lab/monocle3). For the mouse lemur kidney nephron spatial trajectory, all kidney epithelial cells were included in the analysis; podocytes, macula densa cells, intercalated cells, and urothelial cells were not part of nephron gradient and hence excluded from trajectory detection. For vasa recta endothelium

bioRxiv preprint doi: https://doi.org/10.1101/2021.12.12.469460; this version posted August 7, 2022. The copyright holder for this preprint (which was not certified by peer review) is the author/funder. All rights reserved. No reuse allowed without permission.

spatial trajectory, all four vasa recta cell types were used. For spermatogenesis pseudotime trajectory, all seven sperm and sperm progenitor cell types were used. For the myeloid cell developmental pseudotime trajectory, hematopoietic precursor cells and all myeloid cell types except dendritic cells (which did not form part of the continuum) were used. Analysis was performed independently for each trajectory using values from the 10x scRNA-seq profiles of the indicated cells (low quality cells and technical doublets were excluded) that had been pre-processed (scaled: (ln(UP10K +1), normalized) as described above.

Principal component analysis (PCA) with highly-variable genes (dispersion > 0.5) was done with the PCA function of Matlab, and the high quality principal components (not driven by extreme outlier data points or immediate early genes) were selected from the top 20 principal components and used to generate a 2D UMAP using cell-cell Euclidean distances as input (https://www.mathworks.com/matlabcentral/fileexchange/71902). The trajectory of the cell continuum was detected as the probability density ridge of the data points in the UMAP, using automated image processing (Matlab Image Processing Toolbox™); any interruptions in the detected density ridge line were connected manually along the direction of the ridge line and guided by prior knowledge of the biological process, and the direction of the trajectory was assigned based on expression of marker genes. Individual cells were then aligned to the trajectory by the shortest connecting point to the trajectory; if the trajectory branched (e.g., in myeloid cell development), cells were assigned to the closest branch. Individual cells that were too distant from the trajectory (adaptive thresholding along the trajectory) were deemed outliers and removed from further analysis.

To detect genes whose expression followed the trajectory, we calculated the Spearman correlation coefficient and corresponding *p*-values (Bonferroni corrected) between the

bioRxiv preprint doi: https://doi.org/10.1101/2021.12.12.469460; this version posted August 7, 2022. The copyright holder for this preprint (which was not certified by peer review) is the author/funder. All rights reserved. No reuse allowed without permission.

expression level of each gene and 20 preassigned unimodal patterns that smoothly change along the trajectory (with their single peaks uniformly distributed from the beginning of the trajectory to its end point). Expression patterns of the top ranking (top 1000 with *p*-value<0.01) and highly variable (dispersion > 0.5) genes were smoothed with a moving average filter and clustered by k-means clustering to detect the major trajectory-dependent expression patterns. The trajectory differentially-expressed genes were then ranked by the associated cluster (ranked by trajectory location of peak expression), and within the cluster by *p*-value from smallest to largest, and with the same *p*-value by mean expression level from highest to lowest.

For the myeloid cell analysis, four trajectories were independently detected: 1) from hematopoietic precursors to granulocyte monocyte progenitors, 2) from granulocyte monocyte progenitors, proliferating neutrophils, to neutrophils, 3) from granulocyte monocyte progenitors, proliferating macrophages/monocytes, proliferating monocytes, to monocytes and macrophages, and 4) from megakaryocyte progenitors, erythroid progenitor cells, proliferating erythroid lineage cells, to erythroid lineage cells. On the UMAP, trajectory 1 branched into trajectories 2 and 3, so two longer trajectories were generated (1+2, 1+3). Differential gene expression analysis was then independently performed for each of the constituent trajectories (1+2, neutrophil lineage; 1+3, monocyte/macrophage lineage; 4, erythrocyte lineage).

Comparison of expression profiles among mouse lemur cell types

UMAP of cell types - To visualize similarities among the mouse lemur cell type expression profiles, we applied uniform manifold approximation and projection (UMAP) and embedded the high dimensional scRNA-seq expression data (~30,000 genes) to 2D. For this analysis, the 10x scRNA-seq dataset was used and molecular cell types that were low quality (labeled with LQ in free annotation) or represented by less than 4 individual cells were excluded,

bioRxiv preprint doi: https://doi.org/10.1101/2021.12.12.469460; this version posted August 7, 2022. The copyright holder for this preprint (which was not certified by peer review) is the author/funder. All rights reserved. No reuse allowed without permission.

resulting in a comparison of 681 molecular cell types. Molecular cell types were treated as pseudo bulk, with gene expression levels calculated by averaging the expression level of each gene for all cells of that type and then natural log transformed (ln(Avg Count Per 10K UMIs +1)). Expression levels were further normalized by the maximal value of each gene across all cell types, so that all ranged from 0 to 1. The cell type gene expression matrix was then projected onto a 2D space with cosine distances between pairs of cell types used in the UMAP function (https://www.mathworks.com/matlabcentral/fileexchange/71902). The Wilcoxon rank-sum test was used to identify differentially-expressed genes that distinguished related molecular cell types identified in the cell type UMAP from other cell types (e.g., sperm/sperm progenitor cells and immune progenitor/proliferating cells vs. proliferating cells of other compartments) as described in Supplementary Methods.

Heat map of cell type pairwise correlation scores - To compare the overall gene expression profiles of molecular cell types, Pearson's correlation scores were calculated for every pair of molecular cell types. To compare data from different sequencing platforms (10x and SS2), we used the FIRM integrated dataset as described above which contains FIRM-generated principal component (PC) coefficients for each cell. Cell types were treated as pseudo-bulk and the cell type average PC coefficients were calculated and used to determine the correlation coefficients. The cell type pairwise correlation scores were plotted as heat map matrices with cell types arranged in three different orders in the matrices to facilitate comparison (Fig. 5 g-h and Fig. S7). Interactive forms of the heat map matrices are available online (Tabula Microcebus portal, https://tabula-microcebus.ds.czbiohub.org/).

bioRxiv preprint doi: https://doi.org/10.1101/2021.12.12.469460; this version posted August 7, 2022. The copyright holder for this preprint (which was not certified by peer review) is the author/funder. All rights reserved. No reuse allowed without permission.

SAMap analysis

SAMap (Self-Assembling Manifold mapping), a cross-species mapping method[25,83], was used to calculate cell type similarity scores across species (Fig. S8 a, c). SAMap measures the similarity between cell types by calculating an alignment score (edge width in Fig. S8 a, c), which is defined as the average number of cross-species neighbors of each cell relative to the maximum possible number of neighbors in the combined manifold. For application of SAMap to lung and muscle cells, the 10x scRNA-seq datasets for lemurs L1-L4 were used together with the corresponding mouse and human data from 10x scRNA-seq datasets of Tabula Muris Senis[19] and Tabula Sapiens[59], respectively. The defaut SAMap parameters were used in the analysis, and similarity scores less than 0.1 were removed.

Comparison of mouse lemur, human, and mouse cell type expression profiles

For the comparisons, we used published mouse and human scRNA-seq datasets obtained using approaches and standards similar to those described above for mouse lemur, and re-annotated where necessary for consistency with the mouse lemur annotations. Human and mouse lung cell 10x datasets[20] (annotations as published) were compared to lemur lung 10x datasets provided here. Human and mouse limb muscle cell 10x datasets[19,59] (re-annotated here) were compared to lemur limb muscle 10x datasets provided here. Mouse hepatocyte SS2 datasets[19] (re-annotated here) were compared to mouse lemur hepatocyte SS2 profiles provided here.

For each tissue, selection of equivalent cell types for comparison across the three species was done by grouping subtypes of the same cell type (with the exception of proliferating cell types, which were kept separate) and reassigning them the same cell type designation, with the labeling convention kept consistent across all three species (column unified_annotation in h5ad files available on Figshare). Only cell types with more than 20 profiled cells in each of the three

bioRxiv preprint doi: https://doi.org/10.1101/2021.12.12.469460; this version posted August 7, 2022. The copyright holder for this preprint (which was not certified by peer review) is the author/funder. All rights reserved. No reuse allowed without permission.

species were selected for use in the comparisons. To validate that the selected cell types were truly comparable across species, we used the SAMap algorithm (see above) to calculate cell type similarity scores across species, which confirmed that cells with the same cell type designation had the highest similarity score[25]. This was further corroborated by aligning tissue datasets across the three species (after removing cell types that were not selected for comparison) using the BBKNN (batch balanced k nearest neighbours) batch correction algorithm[60] on the 13,302 one-to-one-to-one genes orthologs described below. The resulting UMAP showed that cells with the same cell type designation across the three species almost always clustered nearest to each other (the exceptions were intermixing of lung monocytes, alveolar macrophages, and dendritic cells; lung and muscle *CD4+* and *CD8+* T cells; and muscle tendon and fibroadipoegnic progenitor cells).

For comparison of the transcriptomic profiles of homologous cell types, a list of human, mouse lemur, and mouse one-to-one-to-one gene orthologs (Table 4,5) was compiled by merging mouse lemur, human and mouse homology assignments from the National Center for Biotechnology Information (NCBI) and Ensembl databases. We began by compiling all mouse lemur genes annotated in NCBI (mouse lemur taxonomy ID: 30608) , then merged the corresponding human and mouse orthologs from NCBI (gene_info.gz and gene_orthologs.gz from https://ftp.ncbi.nlm.nih.gov/gene/DATA/, February 2020). We next added Ensembl gene ID numbers, gene names, and human/mouse ortholog assignments from Ensembl Biomart (Ensembl Genes version 99, February 2020) using the Ensembl gene ID (variable 'Gene_stable_ID') for each NCBI gene ID (variable 'NCBI_gene_ID ') in Ensembl Biomart. Mouse lemur genes that did not have an assigned human and mouse ortholog in either Ensembl or NCBI were removed (15,297 out of 31,966 unique mouse lemur NCBI gene IDs), as were

bioRxiv preprint doi: https://doi.org/10.1101/2021.12.12.469460; this version posted August 7, 2022. The copyright holder for this preprint (which was not certified by peer review) is the author/funder. All rights reserved. No reuse allowed without permission.

mouse lemur genes that had more than one human or mouse ortholog assigned, or that shared the same human or mouse ortholog with another mouse lemur gene. Note that unlike NCBI, Ensembl specifies the type of ortholog assignment (e.g., 'ortholog_one2one', 'ortholog_one2many'); however, we did not use the Ensembl specification to filter one-to-one-to-one orthologs because occasionally a mouse lemur gene name was assigned by homology to multiple currently unnamed loci in Ensembl and because of this imperfect genome annotation was labeled as sharing an 'ortholog_one2many' with human/mouse instead of 'ortholog_one2one'. A total of 15,518 one-to-one-to-one gene orthologs were thus uncovered, and of those, 13,302 were found in the human and mouse scRNA-seq datasets described above (Table 4).

Similarity of the transcriptomic profiles between species for each homologous cell type was determined by randomly selecting (by bootstrapping) 1000 trios of cells of the same cell type designation from human, lemur, and mouse, and then calculating the pairwise similarities (human & lemur, lemur & mouse, and human & mouse) of the transcriptomic profiles (of the one-to-one-to-one gene orthologs) in each trio by Xi correlation (Chatterjee 2019) (https://github.com/czbiohub/xicor). Xi correlation is a rank-based algorithm that breaks ties randomly to handle the data sparsity of scRNA-seq datasets. For each of the homologous cell types, differences in Xi correlation values (ΔXi) between each pair of species was used to determine the relative similarity between species (e.g., $Xi_{(lemur, human)} - Xi_{(lemur, mouse)} > 0$) indicates that the lemur cell type is more similar to the corresponding human cell type than to the corresponding mouse cell type). *p*-values were calculated using a t-test under the null hypothesis $\Delta Xi=0$.

bioRxiv preprint doi: https://doi.org/10.1101/2021.12.12.469460; this version posted August 7, 2022. The copyright holder for this preprint (which was not certified by peer review) is the author/funder. All rights reserved. No reuse allowed without permission.

To detect gene orthologs with species-specific expression patterns, we performed differential gene expression analysis using the one-tailed Wilcoxon rank-sum test of lemur vs human, lemur vs mouse, and human vs mouse, independently for each of the homologous cell types. Using a fold change threshold of 10 and a *p*-value threshold of 10^-5, we identified genes with species-selective expression patterns in at least one cell type, excluding genes that were lowly expressed (cell type ln(avgUP10K+1) < 0.5) in the corresponding cell type for all three species. We categorized 6 species-selective expression patterns: 1) high in human and lemur compared to mouse (HumanLemur), 2) high in human and mouse compared to lemur (HumanMouse), 3) high in lemur and mouse compared to human (LemurMouse), 4) high in human compared to lemur and mouse (Human), 5) high in lemur compared to human and mouse (Lemur), and 6) high in mouse compared human and lemur (Mouse). Note that these patterns are not mutually exclusive and a gene may appear within multiple categories for different cell types or identical cell types. Next, within a category, we grouped genes according to whether its species-selective expression pattern was specific to only one cell type or in multiple cell types. For genes with a species-selective pattern in multiple cell types, we further categorized them according to whether the cell types were from the same compartment (e.g., epithelial cells) or different compartments (cross-compartment). The full list of species-specific genes is provided in Table 5, and examples of the cell type-specific, compartment-specific, and cross-compartment expression patterns shown in Fig. S9.

Evolutionary comparison of gene expression during spermatogenesis

To identify spermatid-specific genes that ‘escape’ post meiotic sex chromatin (PMSC) silencing, the expression level (10x dataset, L4) of the 1,453 X-chromosome genes (including non-protein coding genes) was compared across three stages of spermatogenesis: spermatogonia

bioRxiv preprint doi: https://doi.org/10.1101/2021.12.12.469460; this version posted August 7, 2022. The copyright holder for this preprint (which was not certified by peer review) is the author/funder. All rights reserved. No reuse allowed without permission.

(SG), pachytene spermatocytes (PS), and early spermatids (ES). Expression patterns were categorized into 5 groups (A-E) as described for human and mouse[74,75]. Group E is comprised of spermatogenesis-suppressed genes defined by low or undetectable expression (average expression <0.05) across all three stages. The remaining (spermatogenesis-expressed) genes were classified into four groups (A-D). Group A and B genes are repressed in PS (genes likely subject to MSCI), as defined by $E_{PS}<0.5E_{SG}$, with E representing the natural log transform of the average expression of a gene for the cell type denoted by the subscript. To determine if a pachytene-repressed gene was reactivated in ES, we calculated its recovery rate defined by $(E_{ES}-E_{PS})/(E_{SG}-E_{PS})$. PS-repressed genes that remained repressed in ES (recovery rate <0.5) were classified group A, and PS-repressed genes that were reactivated (recovery rate >0.5) were classified group B. Group C and D genes were not repressed in PS ($E_{PS}>0.5E_{SG}$). Genes whose expression increased in spermatid stages compared to pachytene stage ($E_{ES}>E_{PS}$) were classified group C (likely spermatid-specific genes that escape PMSC silencing) and the remaining spermatogenesis-expressed genes that did not follow one of these patterns were classified group D. Mouse lemur group C 'escape' genes were manually compared to the list of human and mouse group C genes obtained by similar classification methods using human and mouse microarray data[74,75] (Table 6). Note genes and unannotated loci from one species that lacked identified orthologs in either of the other two species were included as "species-specific expression patterns" in our classification. Similar results obtained when this analysis was applied to the mouse lemur SS2 dataset.

Data and code availability

scRNA-seq gene expression Counts/UMI tables, and cellular metadata are available on figshare (https://figshare.com/projects/Tabula_Microcebus/112227). Data can be explored

bioRxiv preprint doi: https://doi.org/10.1101/2021.12.12.469460; this version posted August 7, 2022. The copyright holder for this preprint (which was not certified by peer review) is the author/funder. All rights reserved. No reuse allowed without permission.

interactively using cellxgene on the Tabula Microcebus portal: https://tabula-microcebus.ds.czbiohub.org/. Raw sequencing data and genome alignments are available on request.

bioRxiv preprint doi: https://doi.org/10.1101/2021.12.12.469460; this version posted August 7, 2022. The copyright holder for this preprint (which was not certified by peer review) is the author/funder. All rights reserved. No reuse allowed without permission.

FIGURE LEGENDS

Figure 1. Experimental scheme for constructing the mouse lemur cell atlas

a. Overview of four mouse lemurs profiled (name, age, sex), associated metadata collected, and uses of the procured tissues. L1, mouse lemur 1; yo, years old; M, male; F, female; CBC, complete blood count.

b. Representative tissue histology. Micrographs of hematoxylin-and-eosin-stained (H&E) lung section (left) and close-up (second from left) from L1 and small intestine (second from right) and close-up (right) from L3. Full histological atlas of all tissues analyzed from all individuals is available online (the Tabula Microcebus portal, https://tabula-microcebus.ds.czbiohub.org/), and identified histopathology is described in Casey et al.[21]. Scale bars (left to right) 1 mm, 100 μm, 100 μm, 25 μm.

c. The 27 mouse lemur tissues harvested, organized by system, showing for each tissue the number of high-quality cells obtained by 10x scRNA-seq protocol, by SS2 scRNA-seq protocol, number of biological replicates (individuals), and number of molecular cell types identified.

d. Flow diagram for obtaining and processing single cell RNA-sequencing data.

e. Flow diagram for clustering cells with related transcriptomic profiles and annotating the molecular cell types.

f. Representative tissue UMAP showing scRNA-seq profiles of kidney cells (dots) integrated in the same embedded space via FIRM across 10x and SS2 datasets (top left, Step 2) and three individuals (top right, Step 3). Compartment identities of the cell clusters are shown (bottom left) along with heat maps of expression levels (ln(UP10K+1) for 10x data and ln(CP10K+1) for SS2 data, see Methods) of the indicated compartment marker genes (bottom right; *EPCAM*, epithelial; *PTPRC*, immune lymphoid/myeloid; *PECAM*, endothelial; *COL1A1*, stromal).

bioRxiv preprint doi: https://doi.org/10.1101/2021.12.12.469460; this version posted August 7, 2022. The copyright holder for this preprint (which was not certified by peer review) is the author/funder. All rights reserved. No reuse allowed without permission.

g. UMAP of all 244,081 cells in the atlas integrated by FIRM algorithm across all 27 tissues analyzed from four individuals.

Figure 2. Taxonomy of identified mouse lemur molecular cell types

a. Dendrogram of the 256 assigned designations of molecular cell types across cell atlas. Designations are arranged by compartment (epithelial, endothelial, stromal, immune, neural, germ) and then ordered by organ system (epithelial compartment) or biological relatedness (other compartments). Designation number is given below the abbreviation and full names listed in box at right. Some closely related molecular cell types and states are grouped together but shown separately in panel b and Fig. S1, and described further in Section 4. PF, group includes a proliferative cell state; H1-12, hybrid cell types with symbol placed between the two types whose expression signatures the hybrid type shares; M1-7, mixed clusters of distinct cell types too few to assign separately; *, pathological cell states, lung tumor metastasized from uterus (L2) and uterine tumor (L3), as described in accompanying Tabula Microcebus manuscript 2.

b. Dot plot showing number of profiled cells (dot intensity shown by heat map scale, small red dot indicates <10 cells) for each of the 768 identified molecular cell types (including 38 hybrid types) plus 24 mixed clusters isolated from the tissues indicated at left. Molecular cell types in each tissue (rows) are arranged (columns) by cell type number/designation and separated by compartment as in panel a. Black bars, closely related molecular types/subtypes/states (see Fig. 4). +, unknown molecular cell type (Section 4).

Figure 3. Cell types with gene expression gradients

bioRxiv preprint doi: https://doi.org/10.1101/2021.12.12.469460; this version posted August 7, 2022. The copyright holder for this preprint (which was not certified by peer review) is the author/funder. All rights reserved. No reuse allowed without permission.

a. Dendrogram of the 71 molecular cell types identified by scRNA-seq of kidney, arranged as in Fig. 2a.

b. UMAP of kidney epithelial cells (L4, 10x dataset) showing a detected molecular trajectory. Dots, individual cells colored by molecular cell type as indicated; thick black line, cell density ridge (trajectory line); thin gray lines, shortest connecting point of cell to trajectory line. Trajectory shows spatial continuum of molecular cell identities along nephron, beginning with proximal convoluted tubule (PCT, cell type designation #55; see panel a) and ending with principal cells of collecting duct (CDp, #64-66). Macula densa cells (MD, #62) cluster between thin and thick ascending loop of Henle (LoH) cell types (#57-60), and urothelial cells (#69) cluster near CDp cells. Intercalated cells of collecting duct (CDi, #67, 68) and podocytes (#54) cluster separately from trajectory. PCT, proximal convoluted tubule; PST, proximal straight tubule; LoH thin D, loop of Henle thin descending limb; LoH thin A, loop of Henle thin ascending limb; LoH thick A, loop of Henle thick ascending limb; DCT, distal convoluted tubule; CDp, principal cell; CDi alpha, alpha intercalated cell; CDi beta, beta intercalated cell; MD, macula densa.

c. Heat map of relative expression of indicated canonical nephron cell marker genes in cells along nephron trajectory in panel b. Colored bar at top shows cell type designations (colors as in panel b). Gene expression values (ln(UP10K+1) are normalized to stable maximal value (99.5 percentile) for each gene across all cells in trajectory. See panel e for heat map scale (for panels c, e, and j).

d. UMAP of kidney vasa recta endothelial cells (L4, 10x dataset) showing another detected molecular trajectory as in panel b. Trajectory shows spatial continuum of molecular cell identities along vasa recta. VR D, vasa recta descending limb; VR A, vasa recta ascending limb.

bioRxiv preprint doi: https://doi.org/10.1101/2021.12.12.469460; this version posted August 7, 2022. The copyright holder for this preprint (which was not certified by peer review) is the author/funder. All rights reserved. No reuse allowed without permission.

e. Heat map of relative expression of indicated canonical marker genes normalized to stable maximum (99.5 percentile) in cells along vasa recta trajectory in panel d. Bar (at top), cell type designations (colors as in panel d). Note transitions along trajectory (left to right) from artery/arteriole (*GJA5+*) to capillary (*CA4+*) to vein (*ACKR1+*) markers.

f. Micrographs of H&E-stained sections of kidney medulla and cortex analyzed in panels b-e. Scale bars: 100 μm (left), 50 μm (right).

g. UMAP of germ cells from testis (L4, 10x dataset) showing detected molecular trajectory as in panel b. Trajectory shows developmental continuum (developmental pseudotime) of molecular cell identities during spermatogenesis, beginning with stem cells (spermatogonium, #250) and progressing to late spermatids (#256). See Fig. 6c for dot plot of expression of canonical marker genes along trajectory.

h. Micrographs of H&E-stained sections of testis seminiferous tubules analyzed in panel g. Scale bars: 200 μm (left), 50 μm (right).

i. UMAP of myeloid cells from bone and bone marrow (L2, 10x dataset) showing two detected molecular trajectories. One (at left) shows developmental continuum (developmental pseudotime) of molecular cell identities beginning with hematopoietic precursor cells (HPC, #169) and bifurcates at granulocyte-monocyte progenitor cells (GMP, #181) into neutrophil lineage (#175-176) and monocyte/macrophage lineage (#182-184,187). Another trajectory (at right) connects the erythroid progenitor and lineage cells (#172-174), with megakaryocyte progenitor cells (#170) nearby.

j. Heat map of relative expression of indicated canonical marker genes normalized to stable maximal values (99.5 percentile) of each gene in cells (uniformly subsampled for neutrophils) along developmental pseudotime trajectories in panel i (top left, neutrophil trajectory; top right,

bioRxiv preprint doi: https://doi.org/10.1101/2021.12.12.469460; this version posted August 7, 2022. The copyright holder for this preprint (which was not certified by peer review) is the author/funder. All rights reserved. No reuse allowed without permission.

monocyte/macrophage trajectory; bottom: erythroid trajectory). [], description of gene identified by NCBI as a gene locus (LOC105862649 [CD14], LOC105883507 [HBB], LOC105856254 [HBA2]).

Heat maps of genes differentially-expressed along each of the six trajectories are provided in Fig. S3.

Figure 4. Previously unknown and understudied molecular cell types

a. Expansion of molecular cell type dendrogram in Fig. 2a showing individually each of the molecular cell types that are grouped in Fig. 2a. These include molecular types related to a known cell type but distinguished from the major population ("main") or each other indicated by a distinguishing marker gene (e.g., B cell (*SOX5*+), hepatocytes (*APOB*+), hepatocytes (*PHYH*+)) or by a proliferative gene signature (PF), and unidentified ("unknown") molecular cell types. *, molecular types found in only one individual. (), tissue abbreviation indicated for molecular types found in <3 tissues. Bla, Bladder; Blo, Blood; Bon, Bone; BM, Bone marrow; Col, Colon; Cor, Brain cortex; Fat, Fat; Pit, Pituitary; Kid, Kidney; Liv, Liver; Lun, Lung; MG, Mammary gland; Pan, Pancreas; Ski, Skin; SI, Small intestine; Spl, Spleen; Ste, Brainstem; Ton, Tongue; Tra, Trachea; Ute, Uterus.

b. UMAP of liver hepatocytes and cholangiocytes from three individuals (L2, L3, L4, 10x dataset) integrated by FIRM.

c. Dot plot of expression of indicated cell type markers and other differentially-expressed genes in liver *APOB*+ and *PHYH*+ hepatocytes and cholangiocytes of panel b. +, hormone receptor, ligand, and synthase genes. [], description of gene identified by NCBI as a gene locus (LOC105859005 [HP], LOC105861535 [A2M]).

bioRxiv preprint doi: https://doi.org/10.1101/2021.12.12.469460; this version posted August 7, 2022. The copyright holder for this preprint (which was not certified by peer review) is the author/funder. All rights reserved. No reuse allowed without permission.

d. Dot plot of expression of indicated endothelial and capillary markers and differentially-expressed genes for all *FABP5+ RBP7+* and *FABP5- RBP7-* capillary molecular types in atlas (L1-L4, 10x dataset). Note the two sets of differentially-expressed genes (CNS, Peripheral) that distinguish *FABP5- RBP7-* capillary cells from CNS (Cortex (Cor), Brainstem (Ste), Pituitary (Pit)) and peripheral tissues (Blood (Blo), Lung (Lun), Kidney (Kid)), c. [], description of gene designated in NCBI as a gene locus (LOC105857591 [FABP4-like], LOC105879342 [CD36]).

e. UMAP of kidney stromal cells (L2, L3, L4; 10x dataset) integrated by FIRM. Dashed circle, unknown molecular cell type (#143, *ST6GAL2+*; potentially mesangial cells).

f. Dot plot of expression of indicated cell type markers and differentially-expressed genes for kidney stromal cells (L2, L3, L4, 10x dataset). Note unknown molecular cell type (#143) and the set of differentially-expressed genes(Unkn) that distinguish it from the other molecular types.

Figure 5. Relationships of molecular cell types across the mouse lemur cell atlas

a. UMAP of all molecular cell types (dots) in the atlas based on their transcriptomic profiles (mean expression level of each gene for all cells of that type in atlas (L1-L4, 10x dataset)). Dot fill color indicates tissue compartment; black outline, progenitor cell types; gray outline, proliferating cell types; +, unknown cell types. Dashed gray contours, groups of the related cell types indicated.

b-d. UMAP of panel a showing mean expression level of indicated gene in each cell type as heat map, with expression normalized across all cell types. Shown here are examples of genes with expression pattern specific to immune progenitor/proliferating cells and germ cells compared to cell types in other compartments (*CCNB1*, panel b), or to proliferating cells in other compartment (*TESMIN*, panel c), and genes with expression pattern specific to Schwann and

bioRxiv preprint doi: https://doi.org/10.1101/2021.12.12.469460; this version posted August 7, 2022. The copyright holder for this preprint (which was not certified by peer review) is the author/funder. All rights reserved. No reuse allowed without permission.

stromal cells, compared to non-Schwann cell types in the neural compartment (*COL3A1*, panel d).

e-f. Close up of portions of UMAP in panel a showing segregation of the two types of lymphatic cells indicated (e), and segregation of skin and tongue epithelial cell types including those with similar locations/functions in the two tissues (e.g., basal cells) (f).

g. Heat maps of pairwise Pearson correlation coefficients between the transcriptomic profiles of each of the 749 molecular cell type in atlas (10x and SS2 datasets, excluding all cardiac cells), calculated from principal component values of FIRM-integrated UMAP (Fig. 1g) averaged across all cells of each type. Cell types ordered by compartment, then cell type designation/number, and then tissue.

h. Close up of heat map from panel d showing pairwise correlations between skin epithelial cells and all other cell types (top), and between testis germ cells and all other cell types (bottom). Note proliferating skin interfollicular suprabasal cells show high correlation with proliferating and progenitor cell types across all compartments in atlas. Testis spermatogonia also show high correlation with proliferating cell types in the atlas, but especially with hematopoietic stem cells.

Figure 6. Comparison of the transcriptomic profiles of lemur, human, and mouse molecular cell types

a. Comparison of the transcriptomic profiles (10x scRNA-seq datasets generated and annotated in same way for all three species) of orthologous lemur (Tabula Microcebus, this paper), human[20], and mouse (Tabula Muris Senis[19]) lung cell types. Pairwise (human-lemur, lemur-mouse, human-mouse) Xi correlations of the profiles of 1000 randomly-selected trios of the indicated cell types were computed using the 13,302 one-to-one-to-one gene orthologs in the

bioRxiv preprint doi: https://doi.org/10.1101/2021.12.12.469460; this version posted August 7, 2022. The copyright holder for this preprint (which was not certified by peer review) is the author/funder. All rights reserved. No reuse allowed without permission.

three species, and ΔXi values with 95% confidence intervals are shown (left plot, (lemur, human) - (lemur, mouse) ΔXi values, with positive values indicating lemur cell type is more similar to human cell type than to mouse cell type; right plot, (human, lemur) - (human, mouse) ΔXi values, with positive values indicating human cell type is more similar to lemur cell type than to mouse cell type). *P*-values, t-test with null hypothesis ΔXi=0. Similar comparisons of orthologous muscle cell types are provided in Fig. S9. AT2, alveolar type 2 cells; Adv: adventitial; Alv: alveolar; NK, natural killer cells; NKT, natural killer T cells; NK/T(PF): proliferating NK and T cell hybrid; cDC, conventional dendritic cells; pDC: plasmacytoid dendritic cells.

b. Dot plots of expression levels (datasets as in panel a) in indicated lung cell types from human (H), lemur (L), and mouse (M) of selected one-to-one-to-one gene orthologs (gene symbol is that of human ortholog) that show primate-selective expression (>10-fold higher expression in human and lemur than in mouse, p <10^-5) in one or more lung cell types. Cell types are colored by compartment as in Fig. 2, and genes are labeled with the same compartment color if it is selectively expressed in cell type(s) of that compartment, or black for the cross-compartment genes. See Fig. S9 for similar analyses of human-, lemur-, and mouse-selective genes.

c. Dot plot of expression in testis sperm cells (L4, 10x dataset) of the indicated lemur gene orthologs of regulators and marker genes of spermatogenesis previously identified in human[74] and mouse[75]. Filled arrowhead, temporal pattern of expression similar for human and lemur; open arrowhead, pattern similar for lemur and mouse; bold font, pattern specific to lemur; all other genes shown, pattern similar for all three species (comparison data for human and mouse

bioRxiv preprint doi: https://doi.org/10.1101/2021.12.12.469460; this version posted August 7, 2022. The copyright holder for this preprint (which was not certified by peer review) is the author/funder. All rights reserved. No reuse allowed without permission.

spermatogenesis were curated from published studies[65–67,69,71,72,84–91]; description of gene identified by NCBI as a gene locus (e.g., LOC105858542 [DMC1], LOC105858168 [HSPA1L]).

d. UMAP of testis germ cells (L4, 10x dataset) colored by cell type designation (top) and as heatmap showing expression level of *PIWIL1* (bottom). Note *PIWIL1* expression is restricted to early and pachytene spermatocytes.

e. Box (mean and interquartile range) and whisker (outlier cells) plot showing relative expression of all genes on the X-chromosome normalized to all genes on a control autosome (chromosome 2) (mean(ChrX genes)/mean(Chr2 genes)), calculated for each cell during spermatogenesis (L4, 10x and SS2 datasets included in plot), with stages as indicated in panel d. Note sharp diminution in expression of X-chromosome genes in early spermatocytes (#251, corresponding to "meiotic sex chromosome inactivation", MSCI) followed by gradual restoration to about one-third the original value in maturing spermatids during postmeiotic sex chromatin silencing (#254-256).

f. Gene expression levels (ln(UP10K+1) during mouse lemur spermatogenesis for each identified X-chromosome gene that "escapes" postmeiotic silencing during spermatogenesis. Mouse lemur escape gene profiles are separated into four panels according to whether the orthologous gene in the species indicated (human, mouse) is also an escape gene[74,75]. Note most escape genes in lemur are unique to lemur (49 genes) or primate-specific (8 genes). [], description of gene identified by NCBI as a gene locus (e.g., LOC105868203 [TCP11X2], LOC105855602 [H2AB1], LOC105862836 [uncharacterized 1], LOC105855134 [TNP3]).

bioRxiv preprint doi: https://doi.org/10.1101/2021.12.12.469460; this version posted August 7, 2022. The copyright holder for this preprint (which was not certified by peer review) is the author/funder. All rights reserved. No reuse allowed without permission.

TABLES

Table 1. Marker genes from human and/or mouse used to annotate the lemur cells from the atlas

The table lists for each classically defined histological cell type (rows) the known marker genes from corresponding human and/or mouse cell types as well as related references. Marker genes are listed in lemur symbols followed by special notes in brackets (see "Marker gene key"). Cell types are ordered by source tissue with cell types that exist in multiple tissues on the top. For each cell type, the table also lists the corresponding cell ontology assignments, tissue source, compartment assignment, and whether it is identified in the atlas from this study. The "comments" column also describes details regarding the annotation of the cell type.

Table 2. Summary of number of cells and cell types sequenced per individual and tissue

The first sheet ("Summary") provides for each tissue (rows) and for all tissues combined (last row) the total number of cells, number of high quality cells (excluding cells labeled as doublets or low quality) in each individual separately and combined, mean gene count per high quality cell and standard deviation, mean sequencing read (Smart-seq2) or UMI count (10x) per high quality cell and standard deviation, and number of cell types (excluding cells labeled as mix, doublets or low quality). This information is provided for the 10x and SS2 datasets separately and combined. The subsequent sheets are labeled by tissue and provide a list of the cell types annotated in that tissue (including cells labeled as doublets, mix, hybrid, and low quality) with the corresponding assigned tissue system (organized as in Fig. 1c), compartment, and cell ontology designation, dendrogram_annotation_number, order__compartment_freeannotation_tissue, order__tissue_compartment_freeannotation

bioRxiv preprint doi: https://doi.org/10.1101/2021.12.12.469460; this version posted August 7, 2022. The copyright holder for this preprint (which was not certified by peer review) is the author/funder. All rights reserved. No reuse allowed without permission.

(variables explained in "Data" tab of https://tabula-microcebus.ds.czbiohub.org). The number of cells labeled for that cell type are provided for the 10x and SS2 datasets separately and combined, as well as for each individual separately and combined.

Table 3. Differentially-expressed genes for each mouse lemur molecular cell type

Four tables list the top 300 significant (adjusted *p*-value<0.05) differentially-expressed genes (DEGs) detected for each cell type in the 10x dataset (≥5 cells) using four different comparisons: vs. all other cell types in the atlas ("Table 3a DEG_atlas-wide"), vs. all other cell types from the same compartment across the atlas ("Table 3b DEG_atlas-compartment-wide"), vs. all other cell types from the same tissue (sheet "Table 3c DEG_tissue-wide"), or vs. all other cell types from the same compartment of that tissue (sheet "Table 3d DEG_tissue-compartment-wide"). For each cell type, three columns are included: gene symbol (ordered with ascending *p*-values), adjusted *p*-value, and log2-transformed fold-change of the DEGs. Columns of cell types with fewer than 5 10x cells or with no significant DEGs were left blank.

Table 4. Lemur genes and their human and mouse orthology assignments

Table 4a (Summary of lemur one-to-one-to-one orthologs) lists the mouse lemur genes annotated in NCBI that have a corresponding one-to-one-to-one gene orthologs with human and mouse assigned by NCBI and/or Ensembl (15,518 genes, as described in Methods). For each lemur gene, the corresponding NCBI gene ID, gene name, gene description, gene type is provided. The presence of a human ortholog assigned by NCBI and/or Ensembl is indicated in columns 'LemurHuman_NCBI_Homology Type' and 'LemurHuman_Ensembl_HomologyType', respectively, with the corresponding human NCBI and/or Ensembl gene ID and gene name. Similar columns are provided for mouse orthologs assigned by NCBI and/or Ensembl. Column

bioRxiv preprint doi: https://doi.org/10.1101/2021.12.12.469460; this version posted August 7, 2022. The copyright holder for this preprint (which was not certified by peer review) is the author/funder. All rights reserved. No reuse allowed without permission.

'present_in_Human_Mouse_scRNAseq_datasets' indicates whether the gene exists in all three scRNA-seq datasets used for the comparison of gene expression across human, lemur, and mouse in section 6 (true for 13,302 genes).

Table 4b (All lemur orthology assignments) lists all mouse lemur genes annotated in NCBI (31,966) with corresponding NCBI gene ID, synonym, external database cross references (dbXrefs), chromosome location, gene description, and gene type, as well as corresponding Ensembl gene ID and gene name. The presence of human orthologs assigned by NCBI and/or Ensembl (as detailed in Methods) is indicated in columns 'LemurHuman_NCBI_Homology Type' and 'LemurHuman_Ensembl_HomologyType', respectively, with the corresponding human NCBI gene ID, gene name, and synonym as well as corresponding Ensembl gene ID and gene name listed for lemur genes with an assigned ortholog in either of these databases. Similar columns are provided for mouse orthologs assigned by NCBI and/or Ensembl. Rows are duplicated for each lemur NCBI gene with more than one corresponding Ensembl gene, or that is assigned to more than one ortholog human/mouse ortholog.

Table 5. Ortholog genes with species expression patterns in lung and muscle cell types

Each sheet lists the orthologs with one of the six examined species-specific expression patterns of one tissue. The first sheet, for example, named "HumanLemur, Lung" lists the genes that are selectively expressed in human and lemur lung cell types compared to the corresponding cell types of the mouse. Within each sheet, each row lists an ortholog gene. The columns list the ortholog symbols in human (symbol_human), mouse lemur (symbol_lemur), and mouse (symbol_mouse), as well as the information on the cell type(s) and compartment(s) that the ortholog shows the species-specific expression pattern. Columns "Celltypes" and "Compartments" list the cell type(s) and compartment(s) detected, "Ncell type" and

bioRxiv preprint doi: https://doi.org/10.1101/2021.12.12.469460; this version posted August 7, 2022. The copyright holder for this preprint (which was not certified by peer review) is the author/funder. All rights reserved. No reuse allowed without permission.

"Ncompartment" the count, and "celltype" and "compartment" list the corresponding cell type and compartment if they are specific (i.e., Ncelltype or Ncompartment = 1) or "nan" if not.

Table 6. Expression pattern of X-chromosome genes during spermatogenesis in lemur, human, and mouse

The first sheet ("Group C genes_summary") provides the number of X-chromosome genes that are categorized into group C (likely spermatid-specific genes that escape PMSC silencing, as detailed in Methods) for human, lemur, and/or mouse. Numbers are categorized by expression pattern among the species (consistent in all species, or specific to one/two species), and are listed separately for analyses using the lemur testes 10x and SS2 datasets. Sheets "Group C genes_10x" and "Group C genes_SS2" provide a list of all group C genes in each of the three species, categorized by expression pattern among species (expression_pattern). For genes that are categorized as group C in only one/two species, the alternate group is provided for the remaining species when known (and otherwise listed as NA). The sheet "Lemur_Xchr genes by group" lists all lemur X-chromosome genes and the group they are assigned to (as detailed in Methods) using the lemur testes 10x and SS2 datasets separately.

bioRxiv preprint doi: https://doi.org/10.1101/2021.12.12.469460; this version posted August 7, 2022. The copyright holder for this preprint (which was not certified by peer review) is the author/funder. All rights reserved. No reuse allowed without permission.

SUPPLEMENTAL MATERIAL

Legends for Supplementary Figures

Figure S1. Full dendrogram of cell type designations in mouse lemur atlas

Expansion of Fig. 2a showing full dendrogram of the 256 assigned designations of molecular cell type across atlas. Designations are arranged by compartment (epithelial, endothelial, stromal, immune-lymphoid/hematopoietic/myeloid, neural, germ) and then ordered by tissue system (epithelial compartment) or biological relatedness (other compartments). PF, proliferative cell state; H1-12, hybrid cell types (cell clusters with gene signature of two cell types); M1-7, mixed clusters of distinct cell types too few to assign separately; (), tissue abbreviation indicated for cell types present in <4 tissues with full tissue name in black box; *, pathological cell states, lung tumor metastasized from uterus (L2) and uterine tumor (L3), as described in accompanying Tabula Microcebus manuscript 2.

Figure S2. Dendrogram of cell types in brain cortex, brainstem, retina, hypothalamus/pituitary, and limb muscle.

a, b. Dendrograms of the 23 molecular cell types identified from scRNA-seq of brain cortex (3120 10x cells, 292 SS2 cells; L1, L2, L4) (a), and the 25 molecular cell types from brainstem (1988 10x cells, 122 SS2 cells; L2, L4) (b). The cortex and brainstem samples captured 1099 neurons including excitatory (*SLC17A6+*, *SLC17A7+*) and inhibitory (*GAD1+*, *GAD2+*, *SLC32A1+*) neurons that with further resolved by subclustering into at least 10 major molecular types including four cortex-specific excitatory, one brainstem-specific excitatory, one cortex-specific inhibitory, three brainstem-specific inhibitory, and one hybrid population expressing both excitatory and inhibitory markers. Different glial cell types were also identified including

bioRxiv preprint doi: https://doi.org/10.1101/2021.12.12.469460; this version posted August 7, 2022. The copyright holder for this preprint (which was not certified by peer review) is the author/funder. All rights reserved. No reuse allowed without permission.

three molecular types of astrocytes, oligodendrocytes and their precursors (OPCs), choroid plexus cells, ependymal cells, as well as surprisingly Schwann cells (myelinating and non-myelinating) which are generally associated with peripheral nervous system. In the endothelial compartment we identified vein cells as well as capillary cells (*FABP5*- *RBP7*-) that showed distinct gene signatures compared to capillary cells of peripheral tissues (Fig. 4d). In the stromal compartment, vascular smooth muscle cells, pericytes, and leptomeningeal cells were identified. For the immune compartment, major classes of lymphoid and myeloid cells (B, NK/T, macrophages/microglia, neutrophils, and erythroid cells) were identified.

c. Dendrogram of the 11 molecular cell types identified from retina scRNA-seq (938 10x cell, 120 SS2 cells, L4). Identified cells include two types of photoreceptors (dim-light monochromatic rod cells and bright-light multichromatic cones), ON- and OFF- bipolar cells[92] that rods or cones synapse on plus a hybrid bipolar cell type, a type of horizontal neurons, two types of glial cells (Muller and non-myelinating Schwann cells), and three immune populations (macrophages/microglia, neutrophils, erythroid cells). We found that the photoreceptor cells of the mouse lemur retina is rod-dominated (99.4% rods vs. 0.6% cones in the 10x scRNA-seq unsorted sample), which fits the nocturnal behavior of the mouse lemur and is consistent with reported photoreceptor cell densities[93]. Lemurs (and new world monkeys) have only two opsins (unlike old world monkeys and apes which have three[93]), and two of the six sequenced cone cells expressed the long-wave-sensitive cone opsin (*OPN1LW*) but none expressed the short/medium-wave-opsin (*OPN1SW*). Two cell types not obtained are the ganglion cells on which bipolar cells synapse and amacrine cells which serve as inhibitory interneurons that modulate and shape signaling.

bioRxiv preprint doi: https://doi.org/10.1101/2021.12.12.469460; this version posted August 7, 2022. The copyright holder for this preprint (which was not certified by peer review) is the author/funder. All rights reserved. No reuse allowed without permission.

d. Dendrogram of the 34 molecular cell types identified from hypothalamus/pituitary scRNA-seq (2431 10x cells, L4). Identified cells include all five canonical neuroendocrine cell types of the anterior pituitary (based on expression of their corresponding hormones and other classical markers, see Table 2); interestingly, a few cells (labeled "hybrid") expressed markers for more than one neuroendocrine cell type. We also identified a GABAergic neuron and multiple glial molecular types including oligodendrocytes, OPCs, ependymal cells, and astrocytes. In the endothelial compartment, two capillary types were identified, one (capillary *FABP5*- *RBP7*-) shared with brain cortex and brainstem and another (sinusoid *MAFB*+) likely the fenestrated sinusoidal capillaries of the pituitary gland. Stromal compartment cell types identified include vascular smooth muscle cells, pericytes, leptomeningeal cells, and fibroblasts, and immune cell types spanned diverse lymphoid and myeloid cells including several types of immune progenitors and proliferating cells.

e. Dendrogram of the 31 molecular cell types identified from limb muscle scRNA-seq (2968 10x cells, 994 SS2 cells; L2, L4). Identified cells include 10 distinct stromal molecular types as described in the main text, as well as diverse endothelial, lymphoid, and myeloid cells. One significant cell type that was not identified is Schwann cells, which cover the neuromuscular junction and the terminal axon. This might be because, as in humans, the neuromuscular junctions in mouse lemurs may be small[94] and have few associated Schwann cells.

f. UMAPs of limb muscle cells (L2, 10x dataset, L2) separated by compartment. Left to right: endothelial, stromal, lymphoid, and myeloid compartments.

Figure S3. Expression profiles of selected differentially-expressed genes along cell trajectories in Fig. 3.

bioRxiv preprint doi: https://doi.org/10.1101/2021.12.12.469460; this version posted August 7, 2022. The copyright holder for this preprint (which was not certified by peer review) is the author/funder. All rights reserved. No reuse allowed without permission.

a-f. Heat map showing relative expression (10x dataset from lemur, tissue, and compartment indicated at top of panel) of the indicated differentially-expressed genes normalized to stable maximal value (99.5 percentile) of the gene along trajectories of Fig. 3. Genes shown are top three genes from each of the detected trajectory-dependent expression patterns described in Methods. Cells are ordered left to right by their trajectory coordinates, and their cell type designations are indicated by color in top bar (color key as in UMAPs of Fig. 3). Trajectories in panels d and e include bone and bone marrow hematopoietic precursor cells (HPC) and granulocyte/monocyte progenitors (GMP), and heat map in panel f includes bone and bone marrow erythroid progenitors and lineage cells. [], description of gene identified by NCBI as a gene locus (LOC105884179 [BEX1], LOC105877478 [CCSAP], LOC105862715 [DCUN1D1], LOC105881500 [DEFA1], LOC105865511 [FCGR1A], LOC105867419 [GSTP1], LOC105856255 [HBA1], LOC105883507 [HBB], LOC105859005 [HP], LOC105872012 [HLA-DRB1-1], LOC105859819 [HRNR], LOC105874071 [IFITM3], LOC105882927 [LRRC9], LOC105884612 [NAT8B], LOC105880511 [PTMA], LOC105883741 [SERPINB3], LOC105876721 [SERPINB3], LOC105859377 [TMEM45A], LOC105865212 [TMEM14C], LOC105871594 [RGCC], LOC105865610 [RDH7], LOC105865617 [RDH16], LOC105864771 [RNASE2], LOC105876678 [uncharacterized 1], LOC105873147 [uncharacterized 2], LOC105862290 [uncharacterized 3], LOC105858108 [uncharacterized 4], LOC105880776 [uncharacterized 5], LOC105881161 [uncharacterized 6], LOC105871650 [uncharacterized 7]).
g-l. UMAPs and detected molecular trajectories of cells from the indicated tissues and compartments as in Fig. 3, but from other lemur individuals as indicated at bottom left of each UMAP.

bioRxiv preprint doi: https://doi.org/10.1101/2021.12.12.469460; this version posted August 7, 2022. The copyright holder for this preprint (which was not certified by peer review) is the author/funder. All rights reserved. No reuse allowed without permission.

Figure S4. Hepatocyte molecular subtypes in mouse and lemur

a. UMAP of kidney hepatocytes and cholangiocytes (L2, L3, and L4, 10x dataset) integrated by FIRM. Top to bottom: cells colored by molecular cell type annotation, by individual mouse lemur from which each was isolated, by heatmap showing normalized expression of indicated marker genes: *SPP1*, cholangiocyte marker; *APOB*, hepatocyte (*APOB*+) marker; *PHYH*, hepatocyte (*PHYH*+) enriched gene.

b. UMAP of mouse kidney hepatocytes (Tabula Muris Senis SS2 dataset; 9 individuals including 3 females and 6 males, aged 3-24 months)[19]. Note two main clusters that we designate hepatocyte (*Apob*+) and hepatocyte (*Phyh*+), corresponding to differentially-expressed genes and molecular type designations in lemur. Top to bottom: cells colored by molecular cell type annotation, by sex and by age of animal cell was isolated from, and by heatmap showing normalized expression of indicated marker genes (*Apob*, *Phyh*).

c. Dot plot of expression in the indicated lemur (10x dataset as above) and mouse (SS2 dataset as above) hepatocyte molecular types of the indicated hepatocyte markers, differentially-expressed genes between the two molecular types, liver zonation markers[95,96], and cell stress markers including immediate-early genes and heat shock proteins. Note that in both species, hepatocyte molecular types do not correspond to expression of liver zonation markers and do not differ significantly in expression of cell stress markers. +, known hormone receptor, ligand, or synthase gene; [], description of gene identified by NCBI as a gene locus (LOC105859005 [HP], LOC105861535 [A2M], LOC105854822 [CYP1A2], LOC105861495 [CYP2E1]).

d, e. Box and whisker plots of relative number of UMIs (lemur, 10x dataset as above) or transcripts (mouse, SS2 dataset as above) (d) and number of genes (e) detected per cell for each hepatocyte molecular type indicated. Note that in both species, more transcripts/UMIs and genes

bioRxiv preprint doi: https://doi.org/10.1101/2021.12.12.469460; this version posted August 7, 2022. The copyright holder for this preprint (which was not certified by peer review) is the author/funder. All rights reserved. No reuse allowed without permission.

were detected in *APOB+* hepatocytes compared to *PHYH+* hepatocytes. The greater number of genes detected in mouse hepatocytes relative to that of lemur is due to the greater sensitivity of the SS2 scRNA-seq method used for mouse samples.

Figure S5. UMAP and marker genes of previously unknown cell types

a, b. UMAP (a) of the bone stromal and neural cells (L2 and L4, 10x dataset), integrated by FIRM and colored according to molecular cell types. Dashed circle, unknown (*NGFR+ TNNT2+*) stromal cell type (#141). Dot plot (b) showing fraction of expressing cells and average expression in the molecular cell types in panel a for the indicated compartment/cell type marker genes and genes differentially-expressed in the unknown stromal cell type (#141) relative to all other cells from bone.

c, d. UMAP (c) of the tongue stromal and neural cells (L2 and L4, 10x dataset) integrated by FIRM and colored according to molecular cell types. Dashed circles, unknown stromal (*NGFR+ TNNT2+*) cell type (#141) and (*COL15A1+ PTGDS+*) cell type (#142). Dot plot (d) as above showing expression in the molecular cell types in panel c of compartment/cell type marker genes and genes differentially-expressed in the unknown stromal cell types (#141, 142) relative to all other cells from tongue.

e. Dot plot as above showing expression (L1-L4, 10x dataset) of indicated marker genes and differentially-expressed genes in the unknown stromal (*NGFR+ TNNT2+*) populations (#141) from mammary gland, bone, tongue, and pancreas, and the (*COL15A1+ PTGDS+*) population (#142) found in tongue. Also included are cardiomyocytes, mesothelial cells, leptomeningeal cells, and Schwann cells from all tissues, which express high levels of the two unknown populations' tissue-specific, differentially-expressed genes.

bioRxiv preprint doi: https://doi.org/10.1101/2021.12.12.469460; this version posted August 7, 2022. The copyright holder for this preprint (which was not certified by peer review) is the author/funder. All rights reserved. No reuse allowed without permission.

f-g. UMAP (f) of kidney stromal cells (L2, L3, and L4, 10x dataset), integrated by FIRM and colored according to molecular cell types. Dashed circle, unknown stromal (*ST6GAL2+*) cell type (#143). Dot plot (g) as above showing expression in kidney epithelial, endothelial, and stromal cell types of indicated compartment/cell type markers and genes differentially-expressed in the unknown stromal cell type (#143) relative to all other cells from kidney.

h, i. UMAP (h) of epithelial and stromal cells from gonadal fat adipocyte tissue (GAT) (L2, 10x dataset), integrated by FIRM and colored according to molecular cell types. Dashed circle, unknown epithelial (*CRISP3+*) cell type (#15). Dot plot (i) as above showing expression in the molecular cell types in panel h of indicated compartment/cell type marker genes and genes differentially-expressed in the unknown epithelial molecular cell type (#15) relative to all other cells in the GAT.

j. Dot plot as above showing expression of indicated compartment/cell type marker genes (and genes differentially-expressed in epithelial (*CRISP3+*) cell type) in the epithelial (*CRISP3+*) population (#15) from GAT, as well as urothelial cells and mesothelial cells from all tissues (L1-L4, 10x dataset), which share expression of some of the genes differentially-expressed in the unknown epithelial (*CRISP3+*) population (#15). Fibroblasts are also included for comparison. [], description of gene identified by NCBI as a gene locus (LOC109730246 [uncharacterized 1]).

k, l. UMAP (k) of the blood cells (L2 and L4, SS2 dataset), integrated by FIRM and colored according to molecular cell types. Dashed circle, unknown epithelial (*PGAP1+*) cell type (#16). Dot plot (l) as above showing expression of the molecular cell types in panel k of indicated compartment/cell type marker genes and genes differentially-expressed in the unknown epithelial molecular cell type (#16) relative to all other cells from blood. [], description of gene identified by NCBI as a gene locus (LOC105861777 [uncharacterized 2], LOC105884518 [TTC39B]).

bioRxiv preprint doi: https://doi.org/10.1101/2021.12.12.469460; this version posted August 7, 2022. The copyright holder for this preprint (which was not certified by peer review) is the author/funder. All rights reserved. No reuse allowed without permission.

m. Dot plot as above showing expression of indicated compartment/cell type marker genes (and genes differentially-expressed in epithelial (*PGAP1+*) cell type) in the epithelial (*PGAP1+*) cell type (#16) from blood, as well as astrocytes, oligodendrocyte precursor cells (OPC), oligodendrocytes, and ependymal cells from all tissues (L1-L4, SS2 dataset), which express high levels of some of the epithelial (*PGAP1+*) tissue-specific, differentially-expressed genes.

Figure S6. UMAP of lemur molecular cell types showing expression of compartment genes and differentially-expressed genes, and clustering of neutrophil and adipocyte molecular types

a. UMAP of all molecular cell types identified from 10x dataset showing mean expression level of compartment (e.g., epithelial, endothelial, stromal) markers as heat map, with expression values normalized across all cell types. Colors below data points indicate tissue compartment (see Fig. 5a for compartment color legend and more detailed cell type labels).

b-d. UMAP as in panel a showing expression level of indicated differentially-expressed genes. Examples shown include genes enriched in immune progenitor/proliferating cells and germ cells relative to cell types in other compartments (*VRK1*, *CINS2*, b) or to proliferating cells in other compartments (*RSPH14*, *ASB9*, c), and genes enriched in Schwann and stromal cells relative to non-Schwann cell types in neural compartment (*LAMC1*, *SOCS3*, d).

e, f. Close up of portions of UMAP in panel a showing segregation of three types of neutrophils (e) and of two types of adipocytes (f).

Figure S7. Pairwise comparisons of the relationships of the transcriptomic profiles of all molecular cell types across the mouse lemur atlas

bioRxiv preprint doi: https://doi.org/10.1101/2021.12.12.469460; this version posted August 7, 2022. The copyright holder for this preprint (which was not certified by peer review) is the author/funder. All rights reserved. No reuse allowed without permission.

Heat maps as in Fig. 5g of pairwise Pearson correlation coefficients between the transcriptomic profiles of each of the 749 molecular cell type in atlas (10x and SS2 datasets, excluding all cardiac cells because of low quality), calculated from principal component values of FIRM-integrated UMAP (Fig. 1g) averaged across all cells of each type. Cell types ordered by compartment, then cell type annotation number, then tissue (a); by tissue, then compartment, then cell type annotation number (b); and by hierarchical clustering of cell type expression profiles (c). Interactive forms of the heat maps are available at the Tabula Microcebus portal https://tabula-microcebus.ds.czbiohub.org/.

Figure S8. Molecular relationship of human, lemur, and mouse lung and limb muscle cell types

a, c. Sankey plot showing the relationship between human, mouse lemur, and mouse cell types (L1-L4, 10x dataset) for lung (a) and for limb muscle (c) as determined by SAMap algorithm[25] (see Methods). Each cell type in lemur is connected (gray line) to the cell types it maps to in human and mouse datasets; thickness of line indicates similarity score (0-1) between connected cell types. A cell type with no connecting lines indicates it did not map with similarity score > 0.1 to any cell type in the other species.

b, d. UMAP of the indicated homologous cell types in human, lemur, and mouse from lung (b) and from limb muscle (d) corrected for batch effect by BBKNN integration algorithm[60] based on the 13,302 one-to-one-to-one gene orthologs. UMAP colored by compartment (left panel), cell type designation (center), and species (right).

e. Comparison of the transcriptomic profiles (10x scRNA-seq datasets generated and annotated in the same way for all three species) of orthologous lemur (Tabula Microcebus, this paper),

bioRxiv preprint doi: https://doi.org/10.1101/2021.12.12.469460; this version posted August 7, 2022. The copyright holder for this preprint (which was not certified by peer review) is the author/funder. All rights reserved. No reuse allowed without permission.

human (Tabula Sapiens[59]), and mouse (Tabula Muris Senis[19]) muscle cell types, as in Fig. 6a for lung cell types. ΔXi values and 95% confidence intervals are shown, with (lemur, human) - (lemur, mouse) ΔXi values in left plot (positive values indicate lemur cell type is more similar to human cell type than to mouse cell type), and (human, lemur) - (human, mouse) ΔXi values in right plot (positive values indicate human cell type is more similar to lemur cell type than to mouse cell type). *P*-values are from t-test with null hypothesis ΔXi=0.

Figure S9. Orthologous genes with species-selective expression patterns in lung and muscle cell types

Dot plots showing expression of the indicated one-to-one-to-one gene orthologs (symbol is for human ortholog) in human (H), lemur (L), and mouse (L) lung (a-f) and muscle (g-l) cell types showing human/lemur-enriched (a, g), mouse-enriched (b, h), human/mouse-enriched (c, i), lemur-enriched (d, j), lemur/mouse-enriched (e, k), and human-enriched (f, l) expression while also displaying selective expression in the corresponding cell type and/or compartment (genes and cell types labeled in compartment colors of Fig. 2). See Table 5 for full list of species-enriched genes for each lung and muscle cell type. In addition to the primate-enriched genes of lung cell types described in Section 6, note in panel g primate-enriched expression in muscle stromal cells (including MuSCs, FAPs, and tenocytes) of splicing factor *NOVA1*, a proposed driver of human divergence in neuronal cells[97]). Note in panel h the primate-reduced expression in tenocytes of ECM proteins *FBLN7*, *OGN*, and *FMOD*, and matrix processing enzyme *HAS1*, suggesting evolutionarily divergent remodeling mechanisms of tenocyte ECM. Primate MuSCs show reduced expression of *VCAM1*, *SDC4*, and *CD34*, known cell surface markers for mouse

bioRxiv preprint doi: https://doi.org/10.1101/2021.12.12.469460; this version posted August 7, 2022. The copyright holder for this preprint (which was not certified by peer review) is the author/funder. All rights reserved. No reuse allowed without permission.

MuSCs[30,31,98], and enriched expression of *MYF6* and *DLK1*. Note also primate enrichment of type 1 angiotensin II receptor (*AGTR1*) in muscle pericytes, as in lung pericytes (Fig. 6b), and of genes that affect tumor angiogenesis including *IGFBP2*[99], *NOSTRIN*[100], and *HEG1*[101] in vein and capillary endothelial cells. Primate muscle macrophages are enriched for *VSIG4*, an inflammatory response suppressor[102].

bioRxiv preprint doi: https://doi.org/10.1101/2021.12.12.469460; this version posted August 7, 2022. The copyright holder for this preprint (which was not certified by peer review) is the author/funder. All rights reserved. No reuse allowed without permission.

REFERENCES

1. Elsea, S. H. & Lucas, R. E. The mousetrap: what we can learn when the mouse model does not mimic the human disease. *ILAR J.* **43**, (2002).
2. Mestas, J. & Hughes, C. C. Of mice and not men: differences between mouse and human immunology. *J. Immunol.* **172**, (2004).
3. Watase, K. & Zoghbi, H. Y. Modelling brain diseases in mice: the challenges of design and analysis. *Nat. Rev. Genet.* **4**, 296–307 (2003).
4. Ezran, C. *et al.* The Mouse Lemur, a Genetic Model Organism for Primate Biology, Behavior, and Health. *Genetics* **206**, 651–664 (2017).
5. Hozer, C., Pifferi, F., Aujard, F. & Perret, M. The Biological Clock in Gray Mouse Lemur: Adaptive, Evolutionary and Aging Considerations in an Emerging Non-human Primate Model. *Front. Physiol.* **10**, 1033 (2019).
6. Perret, M. & Aujard, F. Daily hypothermia and torpor in a tropical primate: synchronization by 24-h light-dark cycle. *Am. J. Physiol. Regul. Integr. Comp. Physiol.* **281**, (2001).
7. Génin, F., Schilling, A. & Perret, M. Social inhibition of seasonal fattening in wild and captive gray mouse lemurs. *Physiol. Behav.* **86**, 185–194 (2005).
8. Kraska, A. *et al.* Age-associated cerebral atrophy in mouse lemur primates. *Neurobiol. Aging* **32**, 894–906 (2011).
9. Terrien, J. *et al.* Metabolic and genomic adaptations to winter fattening in a primate species, the grey mouse lemur (Microcebus murinus). *Int. J. Obes.* **42**, 221–230 (2018).
10. Languille, S. *et al.* The grey mouse lemur: a non-human primate model for ageing studies. *Ageing Res. Rev.* **11**, 150–162 (2012).
11. Radespiel, U. Sociality in the gray mouse lemur (Microcebus murinus) in northwestern Madagascar. *Am. J. Primatol.* **51**, (2000).
12. Yoder, A. D. *et al.* Remarkable species diversity in Malagasy mouse lemurs (primates, Microcebus). *Proc. Natl. Acad. Sci. U. S. A.* **97**, 11325–11330 (2000).
13. Rina Evasoa, M. *et al.* Variation in reproduction of the smallest-bodied primate radiation, the mouse lemurs (Microcebus spp.): A synopsis. *Am. J. Primatol.* **80**, e22874 (2018).
14. Atsalis, S. *A Natural History of the Brown Mouse Lemur*. vol. 6 (Prentice Hall, 2015).
15. Larsen, P. A. *et al.* Hybrid de novo genome assembly and centromere characterization of the gray mouse lemur (Microcebus murinus). *BMC Biol.* **15**, 110 (2017).
16. Jain, M. *et al.* Nanopore sequencing and assembly of a human genome with ultra-long reads. *Nat. Biotechnol.* **36**, 338–345 (2018).
17. Wu, A. R. *et al.* Quantitative assessment of single-cell RNA-sequencing methods. *Nat. Methods* **11**, 41–46 (2013).
18. The Tabula Muris Consortium. Single-cell transcriptomics of 20 mouse organs creates a Tabula Muris. *Nature* vol. 562 367–372 (2018).
19. The Tabula Muris Consortium. A single-cell transcriptomic atlas characterizes ageing tissues in the mouse. *Nature* **583**, 590–595 (2020).
20. Travaglini, K. J. *et al.* A molecular cell atlas of the human lung from single-cell RNA sequencing. *Nature* **587**, 619–625 (2020).
21. Casey, K. M., Karanewsky, C. J., Pendleton, J. L., Krasnow, M. R. & Albertelli, M. A. Fibrous Osteodystrophy, Chronic Renal Disease, and Uterine Adenocarcinoma in Aged Gray Mouse Lemurs (Microcebus murinus). *Comp. Med.* **71**, 256–266 (2021).
22. Larsson, A. J. M., Stanley, G., Sinha, R., Weissman, I. L. & Sandberg, R. Computational correction of index switching in multiplexed sequencing libraries. *Nat. Methods* **15**, 305–307 (2018).
23. Ming, J. *et al.* FIRM: Flexible integration of single-cell RNA-sequencing data for large-scale multi-tissue cell atlas datasets. *Brief. Bioinform.* bbac167 (2022).

bioRxiv preprint doi: https://doi.org/10.1101/2021.12.12.469460; this version posted August 7, 2022. The copyright holder for this preprint (which was not certified by peer review) is the author/funder. All rights reserved. No reuse allowed without permission.

24. Diehl, A. D. *et al.* The Cell Ontology 2016: enhanced content, modularization, and ontology interoperability. *J. Biomed. Semantics* **7**, (2016).
25. Tarashansky, A. J. *et al.* Mapping single-cell atlases throughout Metazoa unravels cell type evolution. *bioRxiv* 2020.09.28.317784 (2021) doi:10.1101/2020.09.28.317784.
26. Pisani, D. F., Bottema, C. D. K., Butori, C., Dani, C. & Dechesne, C. A. Mouse model of skeletal muscle adiposity: a glycerol treatment approach. *Biochem. Biophys. Res. Commun.* **396**, 767–773 (2010).
27. Tuttle, L. J., Sinacore, D. R. & Mueller, M. J. Intermuscular adipose tissue is muscle specific and associated with poor functional performance. *J. Aging Res.* **2012**, 172957 (2012).
28. Alexander, M. S. *et al.* CD82 Is a Marker for Prospective Isolation of Human Muscle Satellite Cells and Is Linked to Muscular Dystrophies. *Cell Stem Cell* **19**, 800–807 (2016).
29. Xu, X. *et al.* Human Satellite Cell Transplantation and Regeneration from Diverse Skeletal Muscles. *Stem Cell Reports* **5**, 419–434 (2015).
30. Liu, L., Cheung, T. H., Charville, G. W. & Rando, T. A. Isolation of skeletal muscle stem cells by fluorescence-activated cell sorting. *Nat. Protoc.* **10**, 1612–1624 (2015).
31. Sacco, A., Doyonnas, R., Kraft, P., Vitorovic, S. & Blau, H. M. Self-renewal and expansion of single transplanted muscle stem cells. *Nature* **456**, 502–506 (2008).
32. Joe, A. W. B. *et al.* Muscle injury activates resident fibro/adipogenic progenitors that facilitate myogenesis. *Nat. Cell Biol.* **12**, 153–163 (2010).
33. Uezumi, A., Fukada, S.-I., Yamamoto, N., Takeda, S. ’ichi & Tsuchida, K. Mesenchymal progenitors distinct from satellite cells contribute to ectopic fat cell formation in skeletal muscle. *Nat. Cell Biol.* **12**, 143–152 (2010).
34. Wosczyna, M. N. *et al.* Mesenchymal Stromal Cells Are Required for Regeneration and Homeostatic Maintenance of Skeletal Muscle. *Cell Rep.* **27**, 2029–2035.e5 (2019).
35. Uezumi, A. *et al.* Cell-Surface Protein Profiling Identifies Distinctive Markers of Progenitor Cells in Human Skeletal Muscle. *Stem Cell Reports* **7**, 263–278 (2016).
36. Italiani, P. & Boraschi, D. From Monocytes to M1/M2 Macrophages: Phenotypical vs. Functional Differentiation. *Front. Immunol.* **5**, 514 (2014).
37. Peti-Peterdi, J. & Harris, R. C. Macula densa sensing and signaling mechanisms of renin release. *J. Am. Soc. Nephrol.* **21**, 1093–1096 (2010).
38. Liu, S. *et al.* An organism-wide atlas of hormonal signaling based on the mouse lemur single-cell transcriptome. *bioRxiv* 2021.12.13.472243 (2021) doi:10.1101/2021.12.13.472243.
39. Andrès, M., Solignac, M. & Perret, M. Mating system in mouse lemurs: theories and facts, using analysis of paternity. *Folia Primatol.* **74**, (2003).
40. Martin, M. D. & Badovinac, V. P. Defining Memory CD8 T Cell. *Front. Immunol.* **9**, 2692 (2018).
41. Farber, D. L., Yudanin, N. A. & Restifo, N. P. Human memory T cells: generation, compartmentalization and homeostasis. *Nat. Rev. Immunol.* **14**, 24–35 (2014).
42. Ben-Moshe, S. & Itzkovitz, S. Spatial heterogeneity in the mammalian liver. *Nat. Rev. Gastroenterol. Hepatol.* **16**, 395–410 (2019).
43. Celton-Morizur, S. & Desdouets, C. Polyploidization of liver cells. *Adv. Exp. Med. Biol.* **676**, (2010).
44. Coppiello, G. *et al.* Meox2/Tcf15 heterodimers program the heart capillary endothelium for cardiac fatty acid uptake. *Circulation* **131**, 815–826 (2015).
45. Iso, T. *et al.* Capillary endothelial fatty acid binding proteins 4 and 5 play a critical role in fatty acid uptake in heart and skeletal muscle. *Arterioscler. Thromb. Vasc. Biol.* **33**, 2549–2557 (2013).
46. Caprioli, A., Zhu, H. & Sato, T. N. CRBP-III:lacZ expression pattern reveals a novel heterogeneity of vascular endothelial cells. *Genesis* **40**, 139–145 (2004).
47. Hu, C. *et al.* Retinol-binding protein 7 is an endothelium-specific PPAR cofactor mediating an antioxidant response through adiponectin. *JCI Insight* **2**, e91738 (2017).
48. Du, Y. *et al.* Single-Cell Transcriptome Atlas of Murine Endothelial Cells. *Cell* **180**, 764–779.e20 (2020).

bioRxiv preprint doi: https://doi.org/10.1101/2021.12.12.469460; this version posted August 7, 2022. The copyright holder for this preprint (which was not certified by peer review) is the author/funder. All rights reserved. No reuse allowed without permission.

49. Takeda, A. *et al.* Single-Cell Survey of Human Lymphatics Unveils Marked Endothelial Cell Heterogeneity and Mechanisms of Homing for Neutrophils. *Immunity* **51**, 561–572.e5 (2019).
50. Fujimoto, N. *et al.* Single-cell mapping reveals new markers and functions of lymphatic endothelial cells in lymph nodes. *PLoS Biol.* **18**, e3000704 (2020).
51. Jalkanen, S. & Salmi, M. Lymphatic endothelial cells of the lymph node. *Nat. Rev. Immunol.* **20**, 566–578 (2020).
52. Neumann, J. T. *et al.* Application of High-Sensitivity Troponin in Suspected Myocardial Infarction. *N. Engl. J. Med.* **380**, 2529–2540 (2019).
53. Jarolim, P. High sensitivity cardiac troponin assays in the clinical laboratories. *Clin. Chem. Lab. Med.* **53**, 635–652 (2015).
54. Zipes, D. P., Libby, P., Bonow, R. O., Mann, D. L. & Tomaselli, G. F. *Braunwald's Heart Disease E-Book: A Textbook of Cardiovascular Medicine*. (Elsevier Health Sciences, 2018).
55. He, B. *et al.* Single-cell RNA sequencing reveals the mesangial identity and species diversity of glomerular cell transcriptomes. *Nat. Commun.* **12**, 2141 (2021).
56. Gillich, A. *et al.* Capillary cell-type specialization in the alveolus. *Nature* **586**, (2020).
57. Plasschaert, L. W. *et al.* A single-cell atlas of the airway epithelium reveals the CFTR-rich pulmonary ionocyte. *Nature* **560**, 377–381 (2018).
58. Montoro, D. T. *et al.* A revised airway epithelial hierarchy includes CFTR-expressing ionocytes. *Nature* **560**, 319–324 (2018).
59. The Tabula Sapiens Consortium. The Tabula Sapiens: a single cell transcriptomic atlas of multiple organs from individual human donors. *bioRxiv* 2021.07.19.452956 (2021) doi:10.1101/2021.07.19.452956.
60. Polański, K. *et al.* BBKNN: fast batch alignment of single cell transcriptomes. *Bioinformatics* **36**, 964–965 (2020).
61. Chatterjee, S. A new coefficient of correlation. (2019).
62. Choksi, S. P., Lauter, G., Swoboda, P. & Roy, S. Switching on cilia: transcriptional networks regulating ciliogenesis. *Development* **141**, 1427–1441 (2014).
63. Albee, A. J. *et al.* Identification of cilia genes that affect cell-cycle progression using whole-genome transcriptome analysis in Chlamydomonas reinhardtti. *G3* **3**, 979–991 (2013).
64. Van Durme, Y. M. T. A. *et al.* Hedgehog-interacting protein is a COPD susceptibility gene: the Rotterdam Study. *Eur. Respir. J.* **36**, 89–95 (2010).
65. Hermann, B. P. *et al.* The Mammalian Spermatogenesis Single-Cell Transcriptome, from Spermatogonial Stem Cells to Spermatids. *Cell Rep.* **25**, (2018).
66. Wang, M. *et al.* Single-Cell RNA Sequencing Analysis Reveals Sequential Cell Fate Transition during Human Spermatogenesis. *Cell Stem Cell* **23**, (2018).
67. Shami, A. N. *et al.* Single-Cell RNA Sequencing of Human, Macaque, and Mouse Testes Uncovers Conserved and Divergent Features of Mammalian Spermatogenesis. *Dev. Cell* **54**, 529–547.e12 (2020).
68. Turner, J. M. A. Meiotic Silencing in Mammals. *Annu. Rev. Genet.* **49**, 395–412 (2015).
69. Ernst, C., Eling, N., Martinez-Jimenez, C. P., Marioni, J. C. & Odom, D. T. Staged developmental mapping and X chromosome transcriptional dynamics during mouse spermatogenesis. *Nat. Commun.* **10**, 1–20 (2019).
70. Reuter, M. *et al.* Miwi catalysis is required for piRNA amplification-independent LINE1 transposon silencing. *Nature* **480**, 264–267 (2011).
71. Jan, S. Z. *et al.* Unraveling transcriptome dynamics in human spermatogenesis. *Development* **144**, 3659–3673 (2017).
72. Watanabe, T., Cheng, E.-C., Zhong, M. & Lin, H. Retrotransposons and pseudogenes regulate mRNAs and lncRNAs via the piRNA pathway in the germline. *Genome Res.* **25**, 368–380 (2015).
73. Sin, H.-S. & Namekawa, S. H. The great escape: Active genes on inactive sex chromosomes and their evolutionary implications. *Epigenetics* **8**, 887–892 (2013).

bioRxiv preprint doi: https://doi.org/10.1101/2021.12.12.469460; this version posted August 7, 2022. The copyright holder for this preprint (which was not certified by peer review) is the author/funder. All rights reserved. No reuse allowed without permission.

74. Sin, H.-S., Ichijima, Y., Koh, E., Namiki, M. & Namekawa, S. H. Human postmeiotic sex chromatin and its impact on sex chromosome evolution. *Genome Res.* **22**, 827–836 (2012).
75. Namekawa, S. H. *et al.* Postmeiotic sex chromatin in the male germline of mice. *Curr. Biol.* **16**, 660–667 (2006).
76. Han, L. *et al.* Cell transcriptomic atlas of the non-human primate Macaca fascicularis. *Nature* **604**, 723–731 (2022).
77. Bakken, T. E. *et al.* Comparative cellular analysis of motor cortex in human, marmoset and mouse. *Nature* **598**, 111–119 (2021).
78. Hilton, H. G. *et al.* Single-cell transcriptomics of the naked mole-rat reveals unexpected features of mammalian immunity. *PLoS Biol.* **17**, e3000528 (2019).
79. Cao, C. *et al.* Comprehensive single-cell transcriptome lineages of a proto-vertebrate. *Nature* **571**, 349–354 (2019).
80. Sofroniew, N. *et al. napari/napari: 0.4.12rc2*. (Zenodo, 2021). doi:10.5281/ZENODO.3555620.
81. Farouni, R., Djambazian, H., Ferri, L. E., Ragoussis, J. & Najafabadi, H. S. Model-based analysis of sample index hopping reveals its widespread artifacts in multiplexed single-cell RNA-sequencing. *Nat. Commun.* **11**, 2704 (2020).
82. Megill, C. *et al.* cellxgene: a performant, scalable exploration platform for high dimensional sparse matrices. *bioRxiv* 2021.04.05.438318 (2021) doi:10.1101/2021.04.05.438318.
83. Tarashansky, A. J., Xue, Y., Li, P., Quake, S. R. & Wang, B. Self-assembling manifolds in single-cell RNA sequencing data. (2019) doi:10.7554/eLife.48994.
84. Jung, M. *et al.* Unified single-cell analysis of testis gene regulation and pathology in five mouse strains. *Elife* **8**, (2019).
85. Thul, P. J. & Lindskog, C. The human protein atlas: A spatial map of the human proteome. *Protein Science* vol. 27 233–244 (2018).
86. Sun, Y. H., Jiang, F. & Li, X. Z. Disruption of Tdrd5 decouples the stepwise processing of long precursor transcripts during pachytene PIWI-interacting RNA biogenesis. *Biol. Reprod.* **99**, 684–685 (2018).
87. Sun, F., Xu, Q., Zhao, D. & Degui Chen, C. Id4 Marks Spermatogonial Stem Cells in the Mouse Testis. *Sci. Rep.* **5**, 17594 (2015).
88. Oatley, M., Chan, F., Kaucher, A. & Oatley, J. Functional and molecular features of the ID4 germline stem cell population in mouse testes. *Reproduction Abstracts* (2014) doi:10.1530/repabs.1.p177.
89. Ravnik, S. E. & Wolgemuth, D. J. The Developmentally Restricted Pattern of Expression in the Male Germ Line of a MurineCyclin A, Cyclin A2,Suggests Roles in Both Mitotic and Meiotic Cell Cycles. *Dev. Biol.* **173**, 69–78 (1996).
90. Miranda-Vizuete, A. *et al.* Cloning and developmental analysis of murid spermatid-specific thioredoxin-2 (SPTRX-2), a novel sperm fibrous sheath protein and autoantigen. *J. Biol. Chem.* **278**, 44874–44885 (2003).
91. Desvignes, T., Pontarotti, P., Fauvel, C. & Bobe, J. Nme protein family evolutionary history, a vertebrate perspective. *BMC Evolutionary Biology* vol. 9 (2009).
92. Shekhar, K. *et al.* Comprehensive Classification of Retinal Bipolar Neurons by Single-Cell Transcriptomics. *Cell* **166**, (2016).
93. Peichl, L. *et al.* Diversity of photoreceptor arrangements in nocturnal, cathemeral and diurnal Malagasy lemurs. *J. Comp. Neurol.* **527**, (2019).
94. Boehm, I. *et al.* Comparative anatomy of the mammalian neuromuscular junction. *J. Anat.* **237**, 827–836 (2020).
95. Halpern, K. B. *et al.* Erratum: Single-cell spatial reconstruction reveals global division of labour in the mammalian liver. *Nature* **543**, 742 (2017).
96. Aizarani, N. *et al.* A human liver cell atlas reveals heterogeneity and epithelial progenitors. *Nature* **572**, 199–204 (2019).

bioRxiv preprint doi: https://doi.org/10.1101/2021.12.12.469460; this version posted August 7, 2022. The copyright holder for this preprint (which was not certified by peer review) is the author/funder. All rights reserved. No reuse allowed without permission.

97. Trujillo, C. A. *et al.* Reintroduction of the archaic variant of in cortical organoids alters neurodevelopment. *Science* **371**, (2021).
98. Cornelison, D. D., Filla, M. S., Stanley, H. M., Rapraeger, A. C. & Olwin, B. B. Syndecan-3 and syndecan-4 specifically mark skeletal muscle satellite cells and are implicated in satellite cell maintenance and muscle regeneration. *Dev. Biol.* **239**, 79–94 (2001).
99. Azar, W. J. *et al.* IGFBP-2 enhances VEGF gene promoter activity and consequent promotion of angiogenesis by neuroblastoma cells. *Endocrinology* **152**, 3332–3342 (2011).
100. Wang, J. *et al.* Endothelial Nitric Oxide Synthase Traffic Inducer (NOSTRIN) is a Negative Regulator of Disease Aggressiveness in Pancreatic Cancer. *Clin. Cancer Res.* **22**, 5992–6001 (2016).
101. Zhao, Y.-R. *et al.* HEG1 indicates poor prognosis and promotes hepatocellular carcinoma invasion, metastasis, and EMT by activating Wnt/β-catenin signaling. *Clin. Sci.* **133**, 1645–1662 (2019).
102. Li, J. *et al.* VSIG4 inhibits proinflammatory macrophage activation by reprogramming mitochondrial pyruvate metabolism. *Nat. Commun.* **8**, 1322 (2017).

bioRxiv preprint doi: https://doi.org/10.1101/2021.12.12.469460; this version posted August 7, 2022. The copyright holder for this preprint (which was not certified by peer review) is the author/funder. All rights reserved. No reuse allowed without permission.

Fig. 1

a

Mouse lemur (M. *murinus*)

- L1: 9 yo, M
- L2: 10 yo, F
- L3: 11 yo, F
- L4: 11 yo, M

→ Clinical history & physical exam

→ Blood → Metabolic panel & CBC; Single cell RNAseq; Biobank (cells)

→ 26 other organs → Histology & pathology; Single cell RNAseq; Biobank (tissue, cells); Culture (when indicated)

b

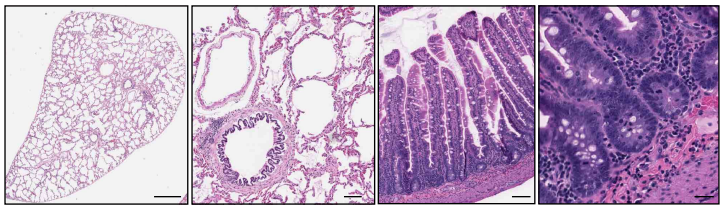

c

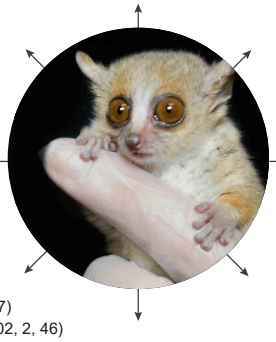

Nervous
1. Brain cortex (3120 10x cells, 292 SS2 cells, 3 individuals, 23 molecular types)
2. Brainstem (1988, 122, 2, 25)
3. Hypothalamus/Pituitary (2431, 0, 1, 34)
4. Retina (938, 120, 1, 11)

Reproductive
26. Uterus (1672, 0, 1, 18)
27. Testis (5639, 705, 1, 12)

Integumentary
5. Skin (23480, 676, 2, 19)
6. Fat (12601, 0, 2, 50)
7. Mammary gland (5396, 0, 1, 25)

Urinary
24. Kidney (13404, 1120, 3, 71)
25. Bladder (6708, 354, 2, 35)

Musculoskeletal
8. Limb muscle (2968, 994, 2, 31)
9. Diaphragm (76, 150, 2, 12)
10. Bone (14585, 1037, 2, 36)

Gastrointestinal
19. Tongue (5952, 449, 2, 27)
20. Small intestine (5825, 302, 2, 46)
21. Colon (1362, 194, 2, 10)
22. Liver (8024, 62, 3, 31)
23. Pancreas (7448, 324, 2, 54)

Circulatory
11. Bone marrow (29948, 1434, 3, 33)
12. Blood (17607, 569, 4, 23)
13. Spleen (8806, 1292, 3, 31)
14. Thymus (0, 66, 1, 8)
15. Heart (2785, 535, 3, 19)
16. Aorta (111, 0, 1, 7)

Respiratory
17. Lung (31527, 1014, 4, 64)
18. Trachea (489, 0, 3, 13)

d

Single Cell RNA sequencing pipeline

Tissue single cell suspension → Droplet-based cDNA library (10x protocol); FACS sorting for live cells → Plate-based cDNA library (SS2 protocol) → Illumina sequencing → Genome alignment (NCBI Mmur3) 10x - cellranger SS2 - STAR → Quality filtering → 244,081 total cells; 226,701 high quality cells (10x: 214,890; SS2: 11,811) → Cell annotation → 256 cell names; 768 molecular types

e

Cell annotation pipeline

Step 1 Manual annotation of each 10x object: cells from one tissue of one individual →

2 FIRM integration of 10x & SS2 within same individual & tissue → Automatically annotate SS2 cells based on manual 10x annotation

3 FIRM integration of all individuals within same tissue → Review annotations for consistency across individuals →

4 FIRM integration of all tissues → Review annotations for consistency across tissues →

Visualize and cluster cells based on molecular expression (2-D tSNE/UMAP) → Compartment separation
- *Epithelial*
- *Endothelial*
- *Stromal*
- *Immune*
- *Neural*
- *Germ*

→ Cluster cells in compartment (Louvain) → *Unique molecular type in each cluster + expert curation* → Assign cell type name and corresponding cell ontology based on cannonical human and mouse marker genes → Add qualifier

Molecular diversity within cluster → Iteratively subcluster

- *Cell type*
- *Unknown*
- *Hybrid*
- *Mix*
- *Doublet*

Marker gene if >1 molecular cluster

f

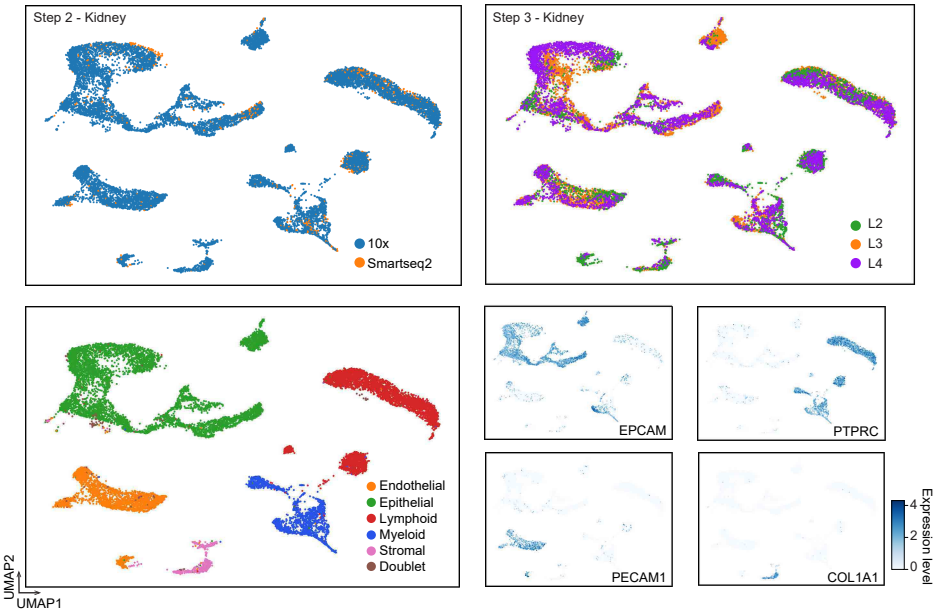

g

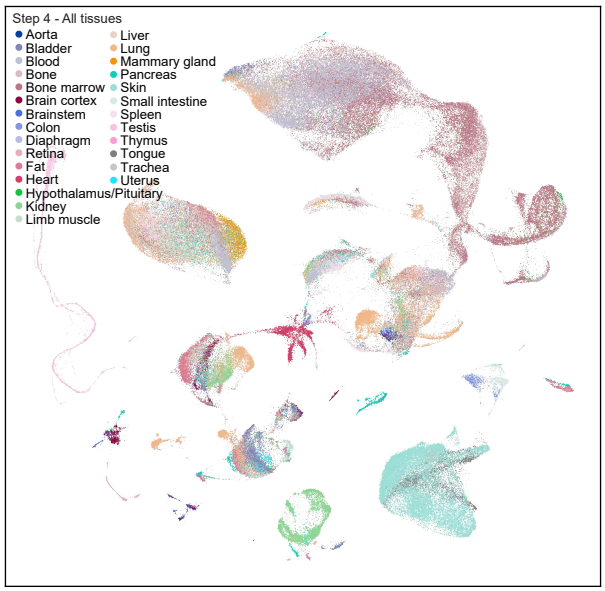

bioRxiv preprint doi: https://doi.org/10.1101/2021.12.12.469460; this version posted August 7, 2022. The copyright holder for this preprint (which was not certified by peer review) is the author/funder. All rights reserved. No reuse allowed without permission.

Fig. 2

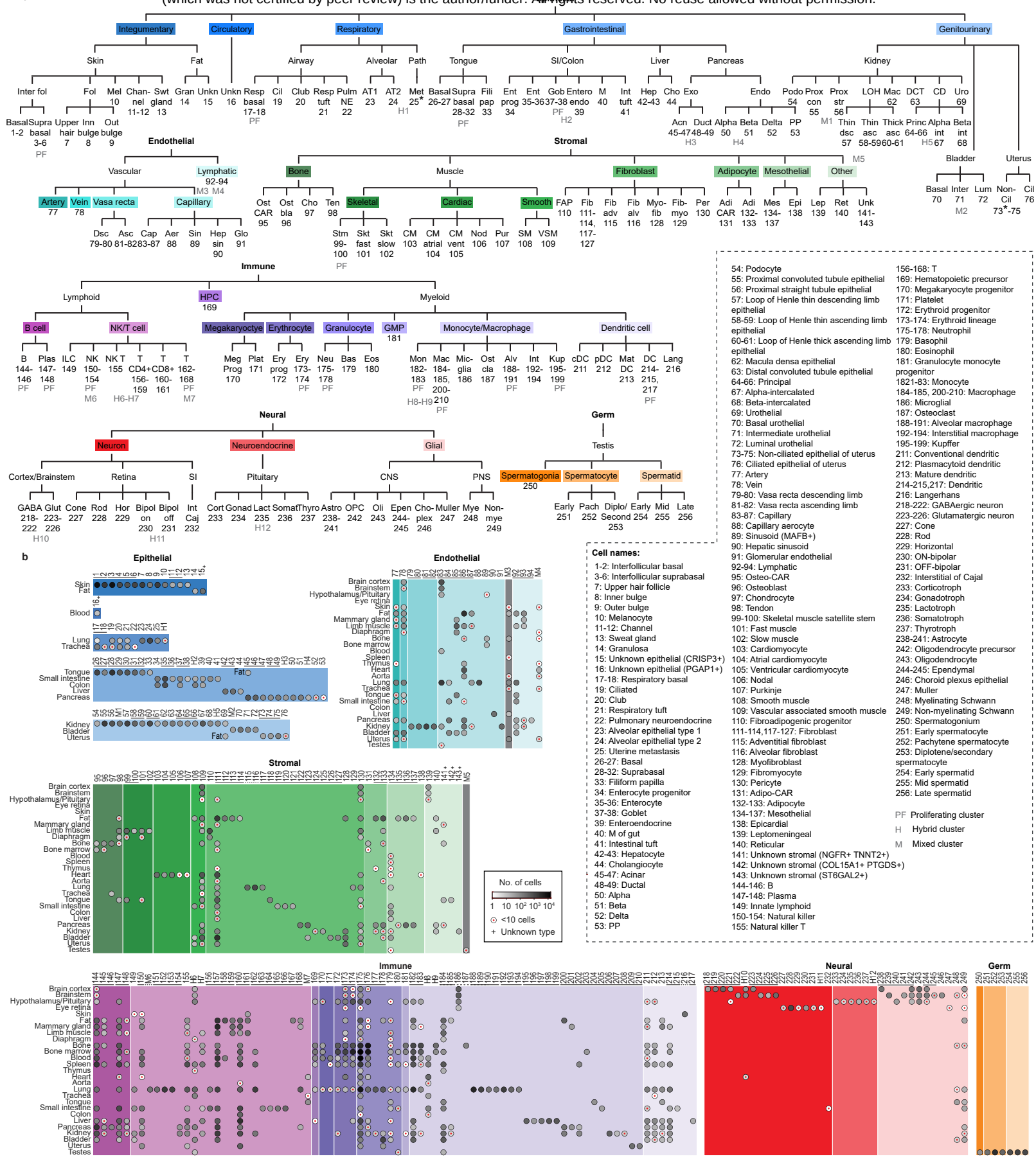

Cell names:

1-2: Interfollicular basal
3-6: Interfollicular suprabasal
7: Upper hair follicle
8: Inner bulge
9: Outer bulge
10: Melanocyte
11-12: Channel
13: Sweat gland
14: Granulosa
15: Unknown epithelial (CRISP3+)
16: Unknown epithelial (PGAP1+)
17-18: Respiratory basal
19: Ciliated
20: Club
21: Respiratory tuft
22: Pulmonary neuroendocrine
23: Alveolar epithelial type 1
24: Alveolar epithelial type 2
25: Uterine metastasis
26-27: Basal
28-32: Suprabasal
33: Filiform papilla
34: Enterocyte progenitor
35-36: Enterocyte
37-38: Goblet
39: Enteroendocrine
40: M of gut
41: Intestinal tuft
42-43: Hepatocyte
44: Cholangiocyte
45-47: Acinar
48-49: Ductal
50: Alpha
51: Beta
52: Delta
53: PP
54: Podocyte
55: Proximal convoluted tubule epithelial
56: Proximal straight tubule epithelial
57: Loop of Henle thin descending limb epithelial
58-59: Loop of Henle thin ascending limb epithelial
60-61: Loop of Henle thick ascending limb epithelial
62: Macula densa epithelial
63: Distal convoluted tubule epithelial
64-66: Principal
67: Alpha-intercalated
68: Beta-intercalated
69: Urothelial
70: Basal urothelial
71: Intermediate urothelial
72: Luminal urothelial
73-75: Non-ciliated epithelial of uterus
76: Ciliated epithelial of uterus
77: Artery
78: Vein
79-80: Vasa recta descending limb
81-82: Vasa recta ascending limb
83-87: Capillary
88: Capillary aerocyte
89: Sinusoid (MAFB+)
90: Hepatic sinusoid
91: Glomerular endothelial
92-94: Lymphatic
95: Osteo-CAR
96: Osteoblast
97: Chondrocyte
98: Tendon
99-100: Skeletal muscle satellite stem
101: Fast muscle
102: Slow muscle
103: Cardiomyocyte
104: Atrial cardiomyocyte
105: Ventricular cardiomyocyte
106: Nodal
107: Purkinje
108: Smooth muscle
109: Vascular associated smooth muscle
110: Fibroadipogenic progenitor
111-114,117-127: Fibroblast
115: Adventitial fibroblast
116: Alveolar fibroblast
128: Myofibroblast
129: Fibromyocyte
130: Pericyte
131: Adipo-CAR
132-133: Adipocyte
134-137: Mesothelial
138: Epicardial
139: Leptomeningeal
140: Reticular
141: Unknown stromal (NGFR+ TNNT2+)
142: Unknown stromal (COL15A1+ PTGDS+)
143: Unknown stromal (ST6GAL2+)
144-146: B
147-148: Plasma
149: Innate lymphoid
150-154: Natural killer
155: Natural killer T
156-168: T
169: Hematopoietic precursor
170: Megakaryocyte progenitor
171: Platelet
172: Erythroid progenitor
173-174: Erythroid lineage
175-178: Neutrophil
179: Basophil
180: Eosinophil
181: Granulocyte monocyte progenitor
1821-83: Monocyte
184-185, 200-210: Macrophage
186: Microglial
187: Osteoclast
188-191: Alveolar macrophage
192-194: Interstitial macrophage
195-199: Kupffer
211: Conventional dendritic
212: Plasmacytoid dendritic
213: Mature dendritic
214-215,217: Dendritic
216: Langerhans
218-222: GABAergic neuron
223-226: Glutamatergic neuron
227: Cone
228: Rod
229: Horizontal
230: ON-bipolar
231: OFF-bipolar
232: Interstitial of Cajal
233: Corticotroph
234: Gonadotroph
235: Lactotroph
236: Somatotroph
237: Thyrotroph
238-241: Astrocyte
242: Oligodendrocyte precursor
243: Oligodendrocyte
244-245: Ependymal
246: Choroid plexus epithelial
247: Muller
248: Myelinating Schwann
249: Non-myelinating Schwann
250: Spermatogonium
251: Early spermatocyte
252: Pachytene spermatocyte
253: Diplotene/secondary spermatocyte
254: Early spermatid
255: Mid spermatid
256: Late spermatid

PF Proliferating cluster
H Hybrid cluster
M Mixed cluster

bioRxiv preprint doi: https://doi.org/10.1101/2021.12.12.469460; this version posted August 7, 2022. The copyright holder for this preprint (which was not certified by peer review) is the author/funder. All rights reserved. No reuse allowed without permission.

Fig. 3

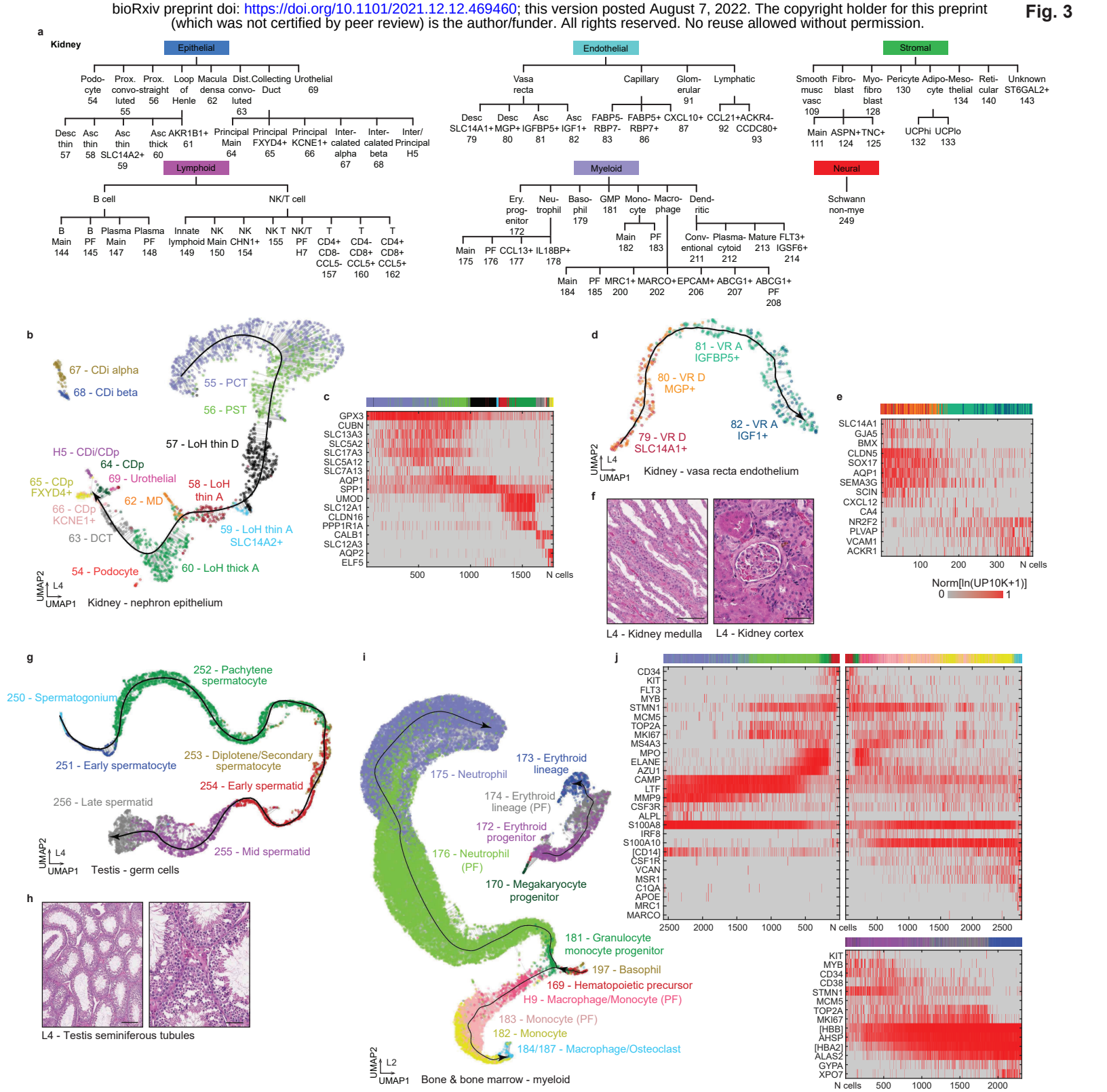

bioRxiv preprint doi: https://doi.org/10.1101/2021.12.12.469460; this version posted August 7, 2022. The copyright holder for this preprint (which was not certified by peer review) is the author/funder. All rights reserved. No reuse allowed without permission.

Fig. 4

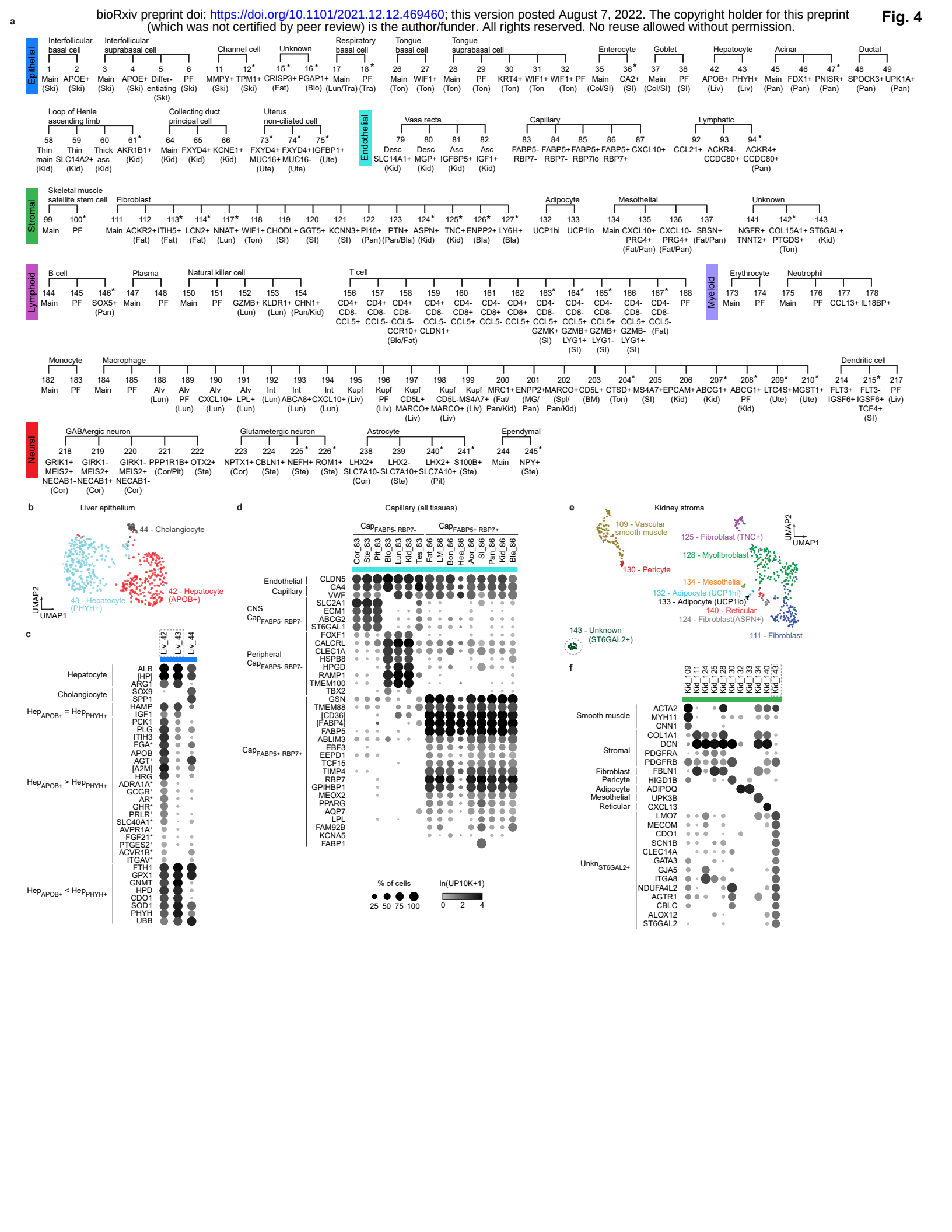

bioRxiv preprint doi: https://doi.org/10.1101/2021.12.12.469460; this version posted August 7, 2022. The copyright holder for this preprint (which was not certified by peer review) is the author/funder. All rights reserved. No reuse allowed without permission.

Fig. 5

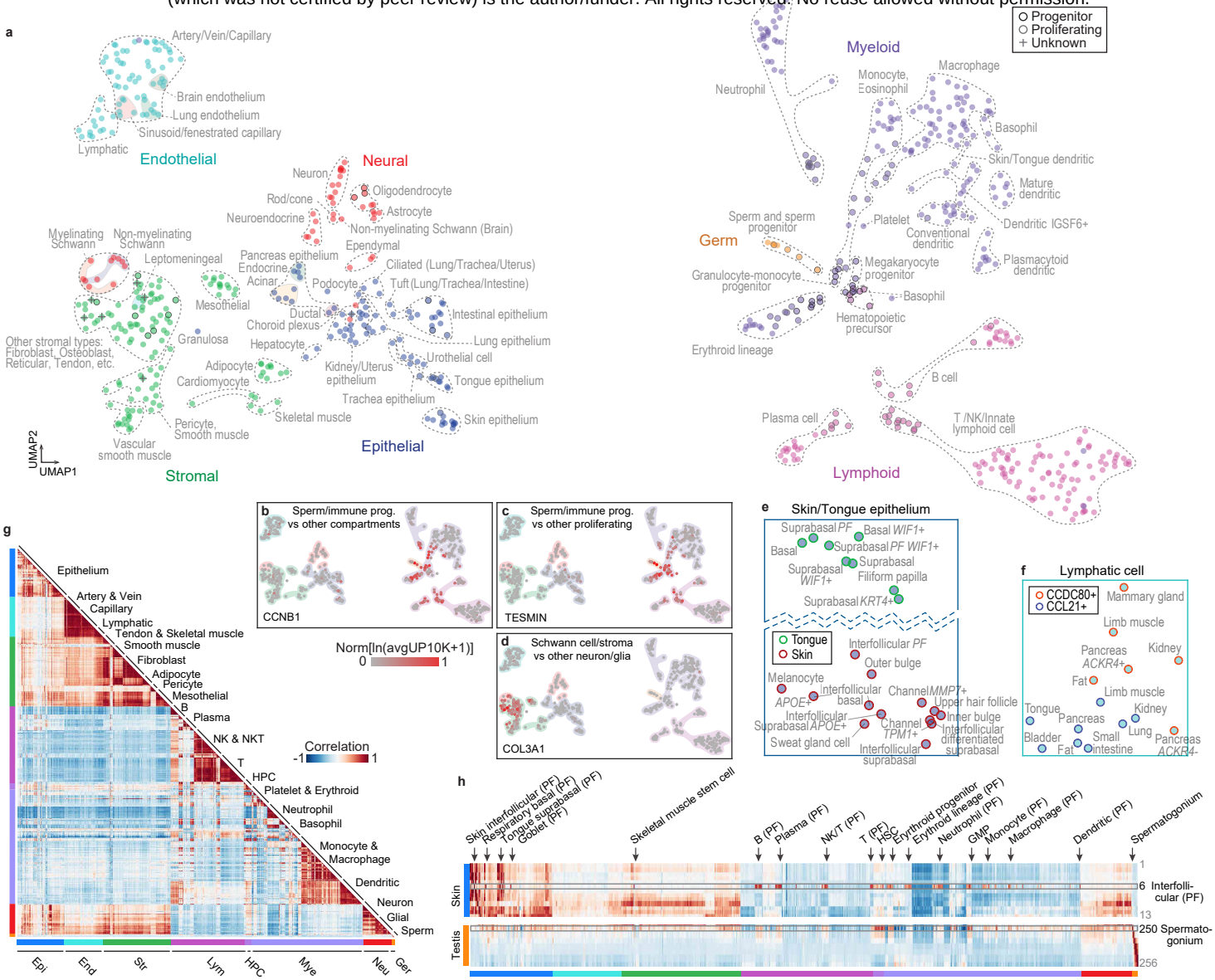

bioRxiv preprint doi: https://doi.org/10.1101/2021.12.12.469460; this version posted August 7, 2022. The copyright holder for this preprint (which was not certified by peer review) is the author/funder. All rights reserved. No reuse allowed without permission.

Fig. 6

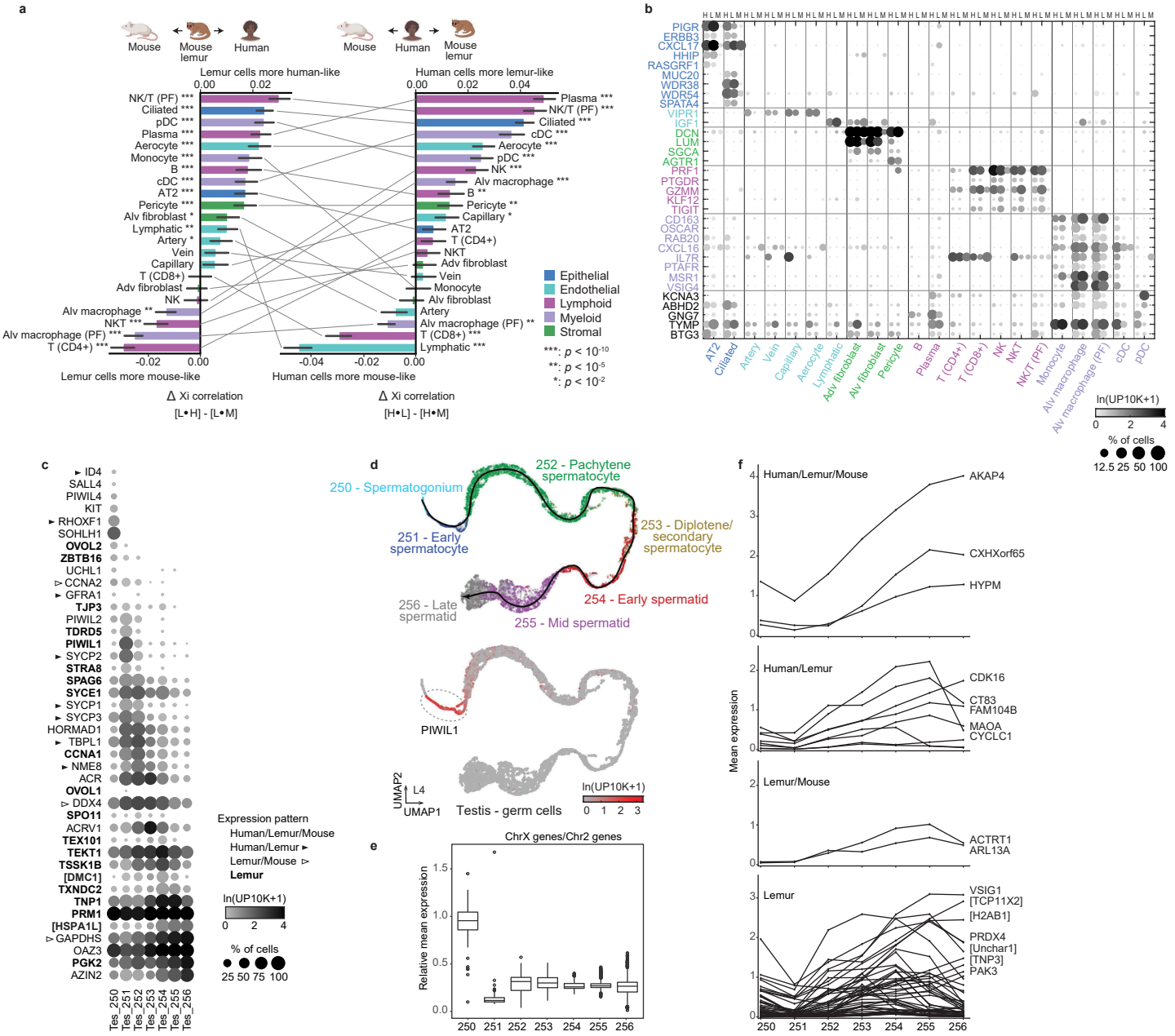

bioRxiv preprint doi: https://doi.org/10.1101/2021.12.12.469460; this version posted August 7, 2022. The copyright holder for this preprint (which was not certified by peer review) is the author/funder. All rights reserved. No reuse allowed without permission.

Fig. S1

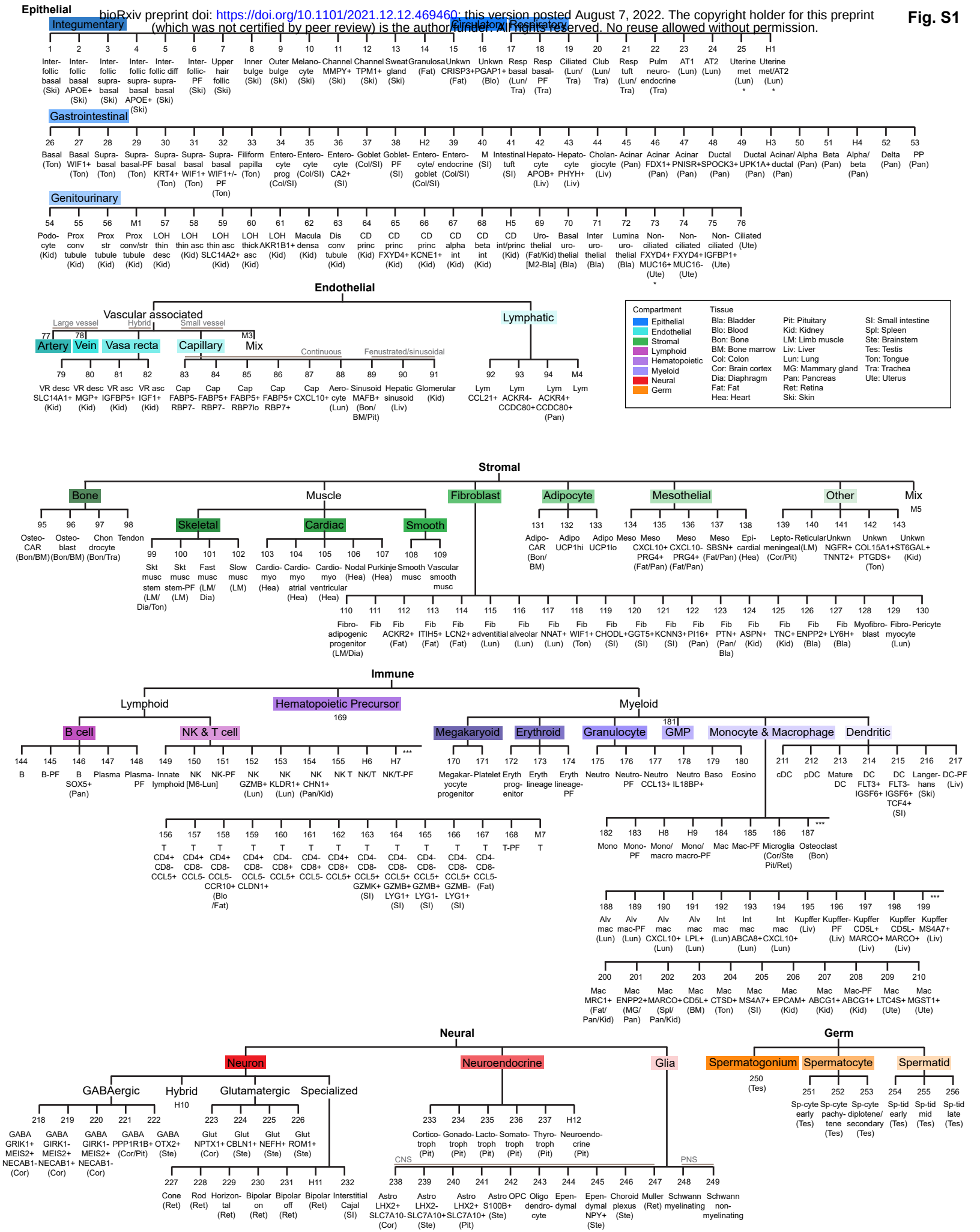

bioRxiv preprint doi: https://doi.org/10.1101/2021.12.12.469460; this version posted August 7, 2022. The copyright holder for this preprint (which was not certified by peer review) is the author/funder. All rights reserved. No reuse allowed without permission.

Fig. S2

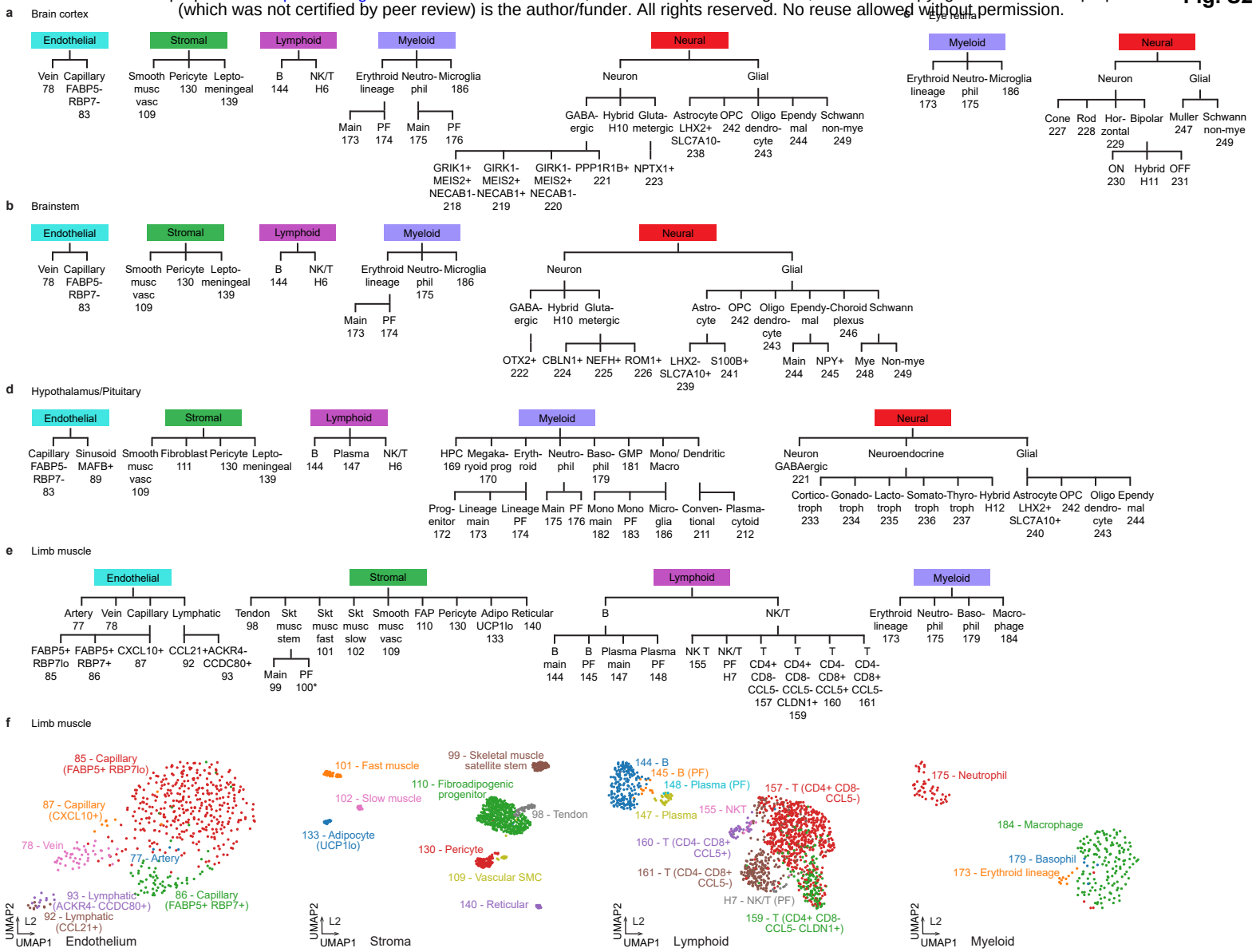

bioRxiv preprint doi: https://doi.org/10.1101/2021.12.12.469460; this version posted August 7, 2022. The copyright holder for this preprint (which was not certified by peer review) is the author/funder. All rights reserved. No reuse allowed without permission.

Fig. S3

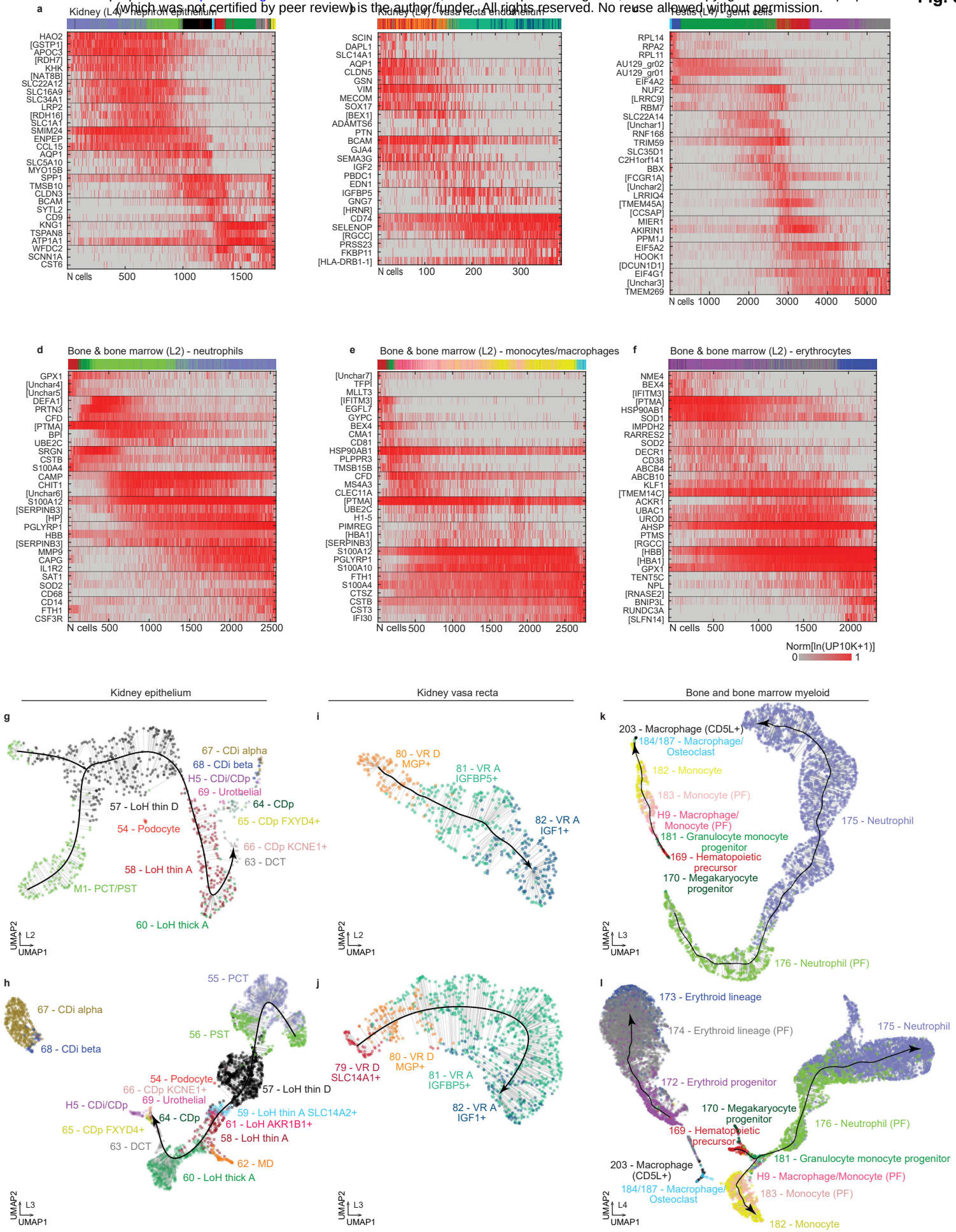

bioRxiv preprint doi: https://doi.org/10.1101/2021.12.12.469460; this version posted August 7, 2022. The copyright holder for this preprint (which was not certified by peer review) is the author/funder. All rights reserved. No reuse allowed without permission.

Fig. S4

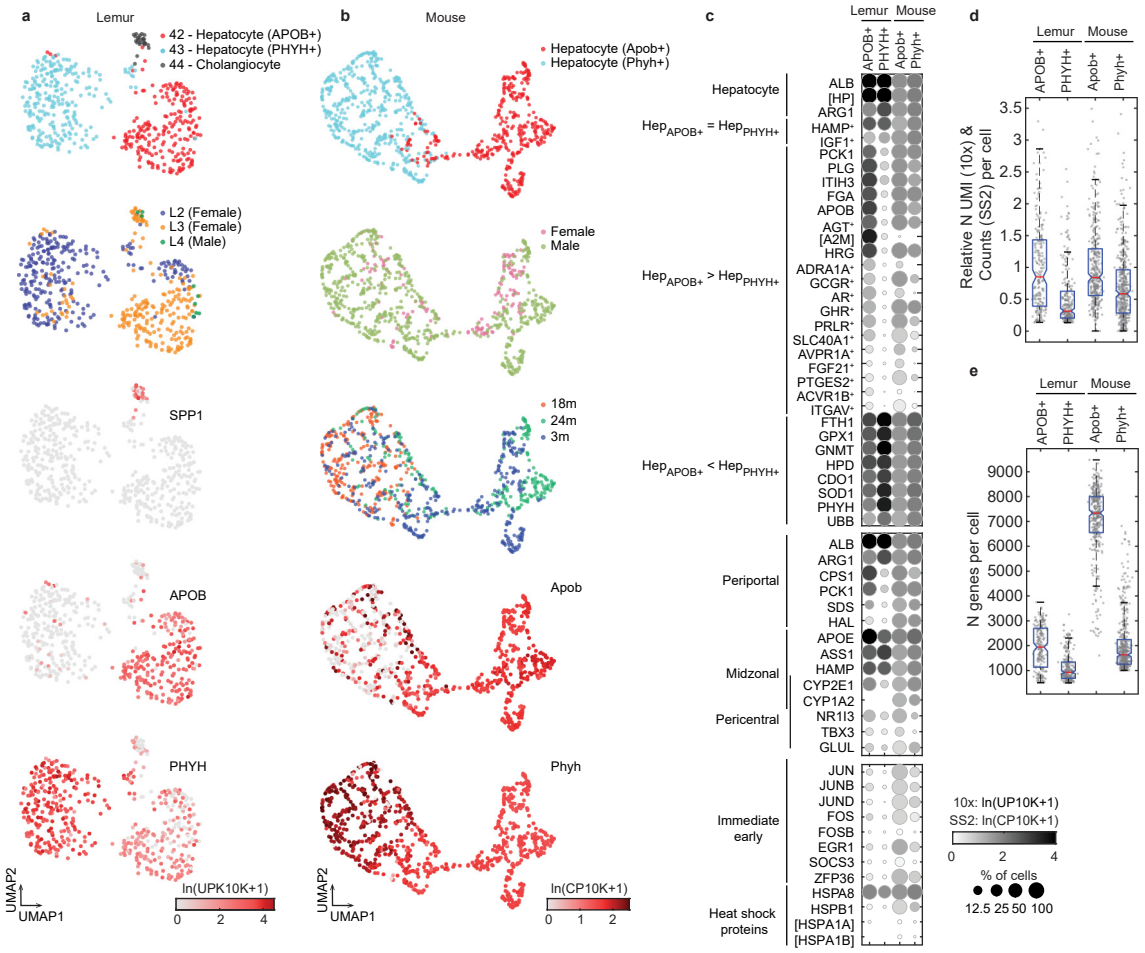

bioRxiv preprint doi: https://doi.org/10.1101/2021.12.12.469460; this version posted August 7, 2022. The copyright holder for this preprint (which was not certified by peer review) is the author/funder. All rights reserved. No reuse allowed without permission.

Fig. S5

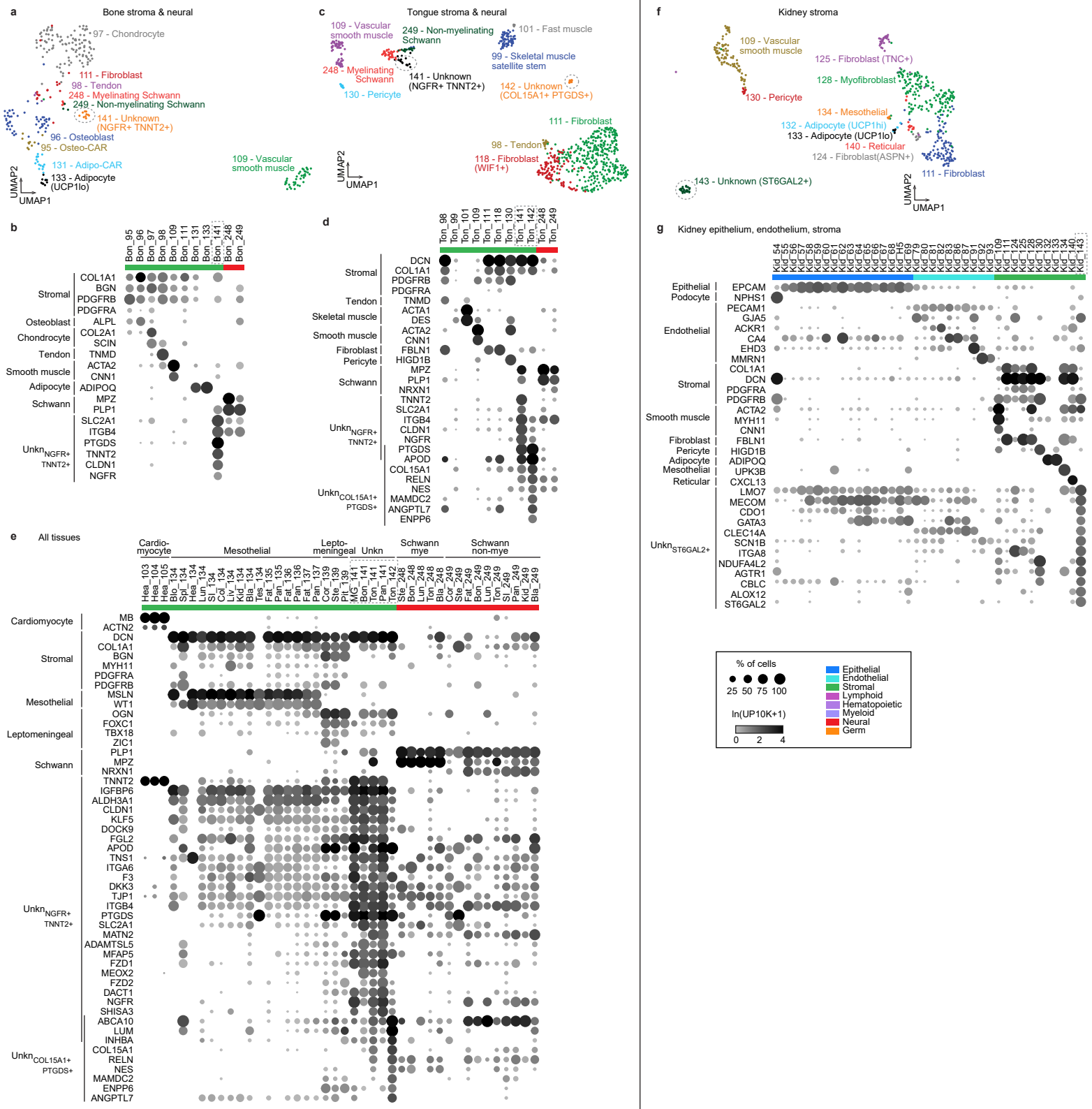

bioRxiv preprint doi: https://doi.org/10.1101/2021.12.12.469460; this version posted August 7, 2022. The copyright holder for this preprint (which was not certified by peer review) is the author/funder. All rights reserved. No reuse allowed without permission.

Fig. 85 - continued

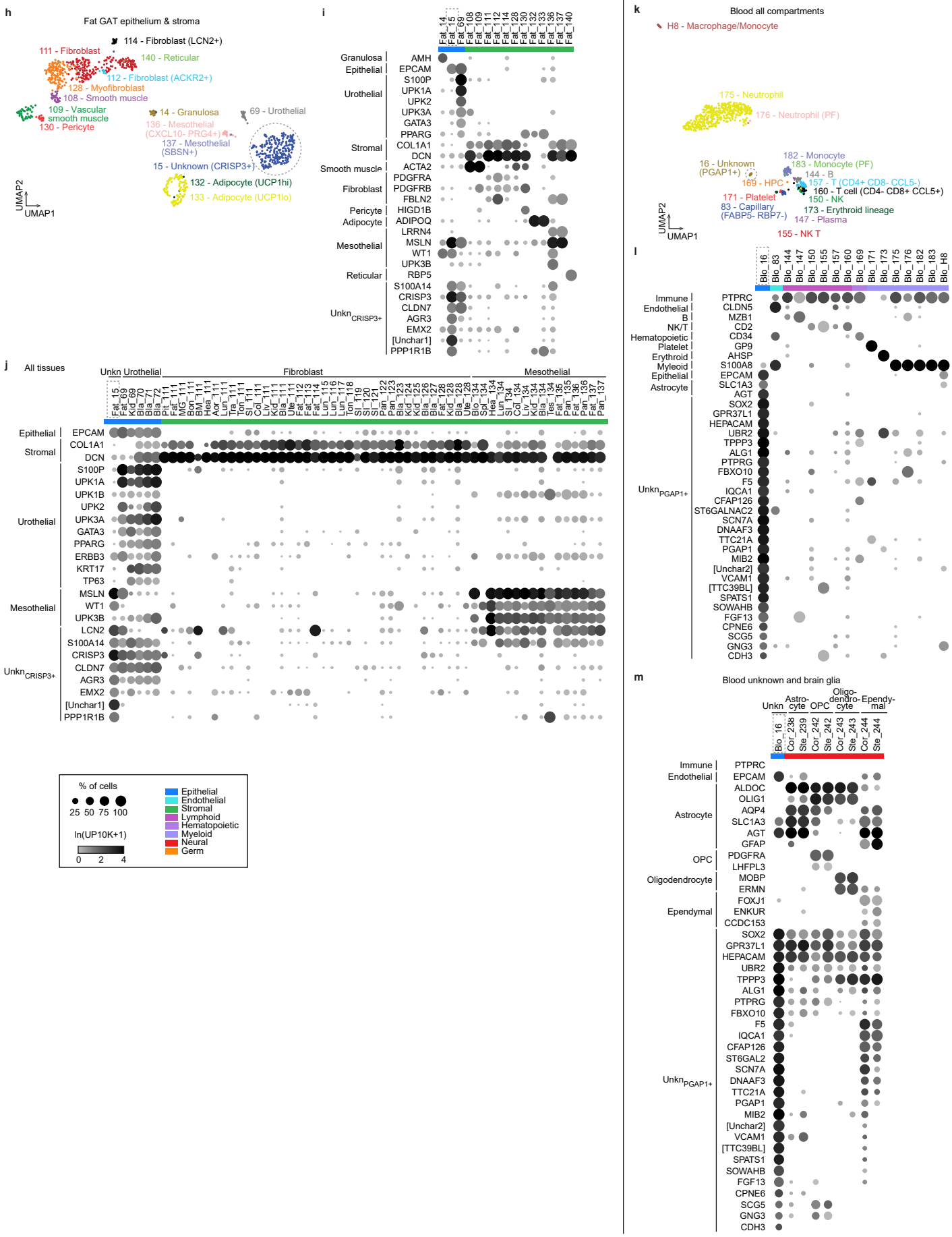

bioRxiv preprint doi: https://doi.org/10.1101/2021.12.12.469460; this version posted August 7, 2022. The copyright holder for this preprint (which was not certified by peer review) is the author/funder. All rights reserved. No reuse allowed without permission.

Fig. S6

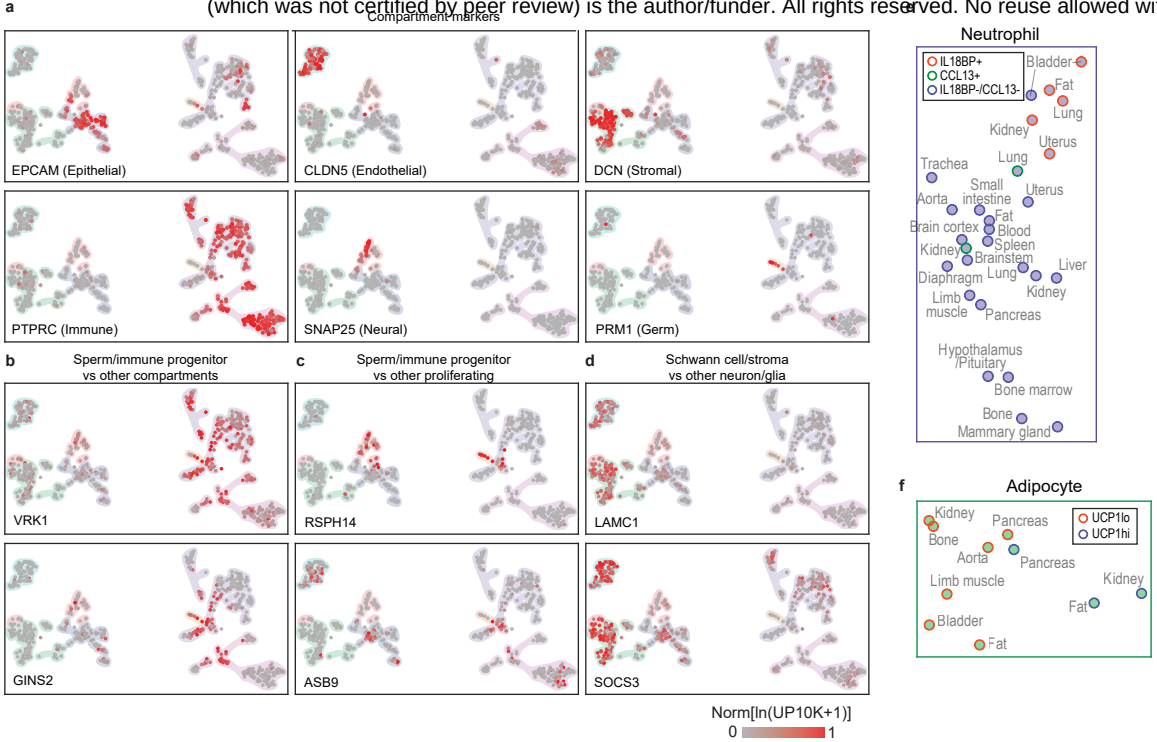

Fig. S7

a. Correlation heatmap A - ordered by compartment, cell type, tissue

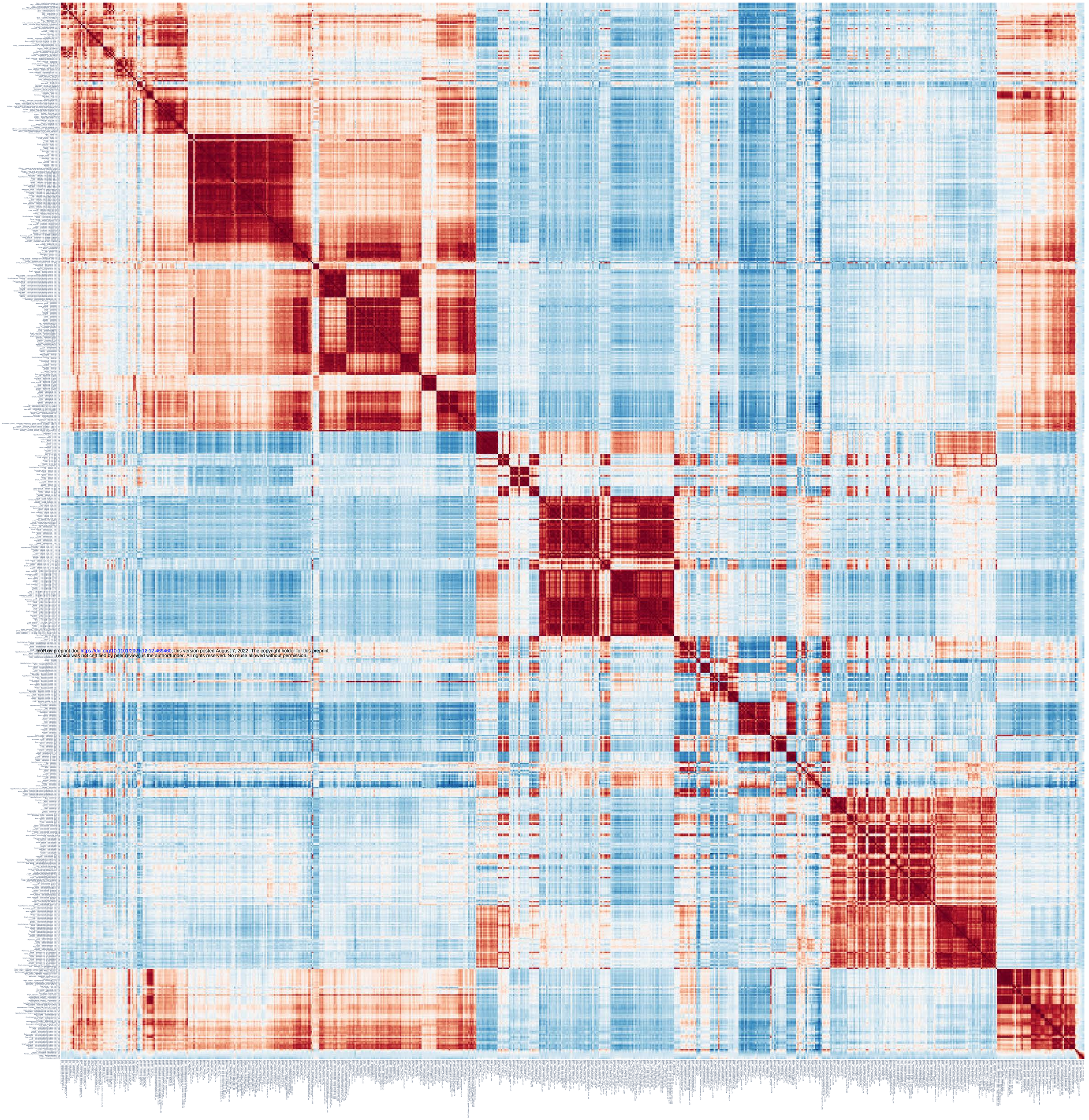

bioRxiv preprint doi: https://doi.org/10.1101/2021-12.12.469460; this version posted August 7, 2022. The copyright holder for this preprint (which was not certified by peer review) is the author/funder. All rights reserved. No reuse allowed without permission.

b. Correlation heatmap B - ordered by tissue, compartment, cell type

Fig. S7 - continued

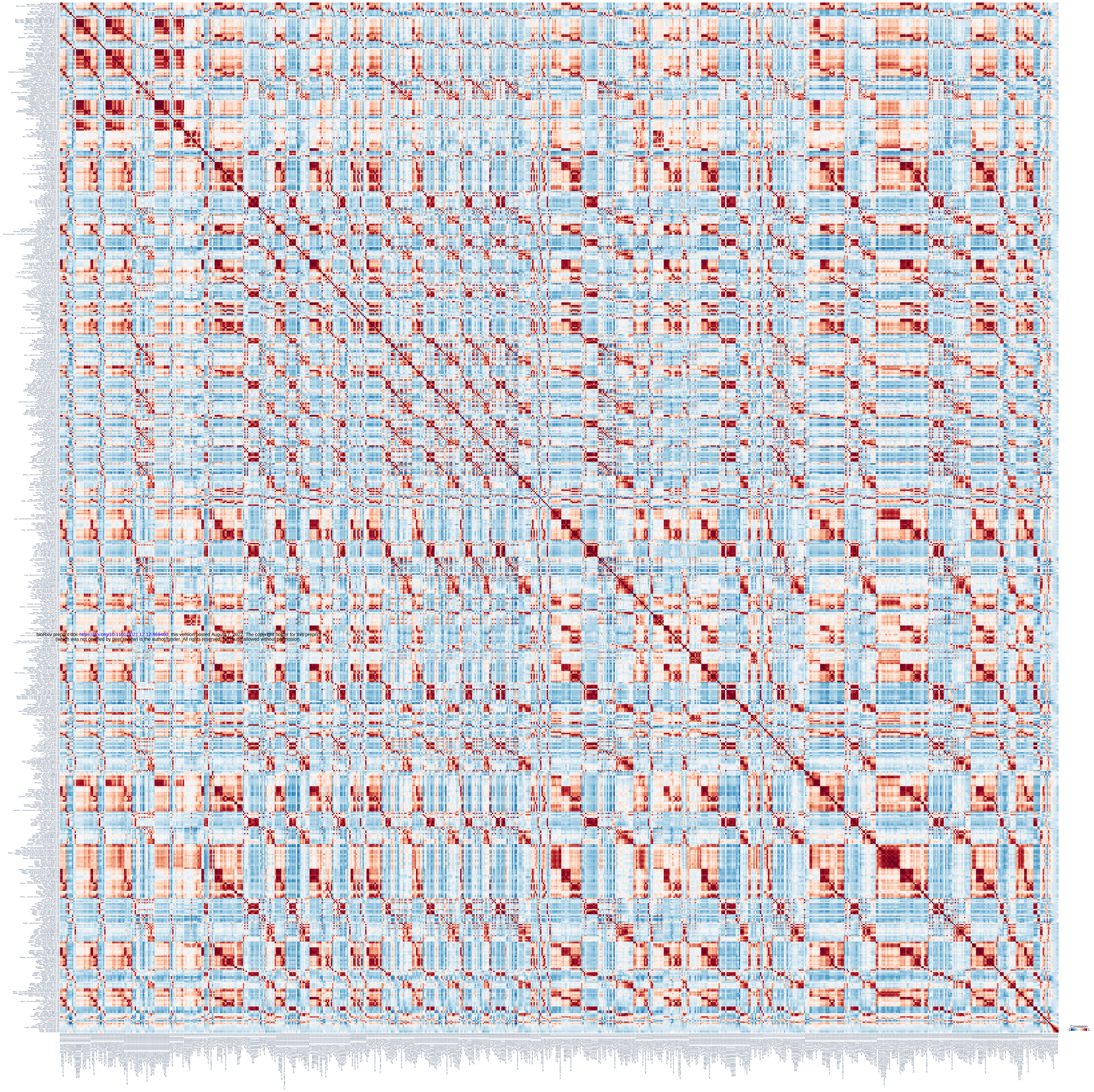

bioRxiv preprint doi: https://doi.org/10.1101/2021.12.12.469460; this version posted August 7, 2022. The copyright holder for this preprint (which was not certified by peer review) is the author/funder. All rights reserved. No reuse allowed without permission.

c. Correlation heatmap C - ordered by hierarchical clustering

Fig. S7 - continued

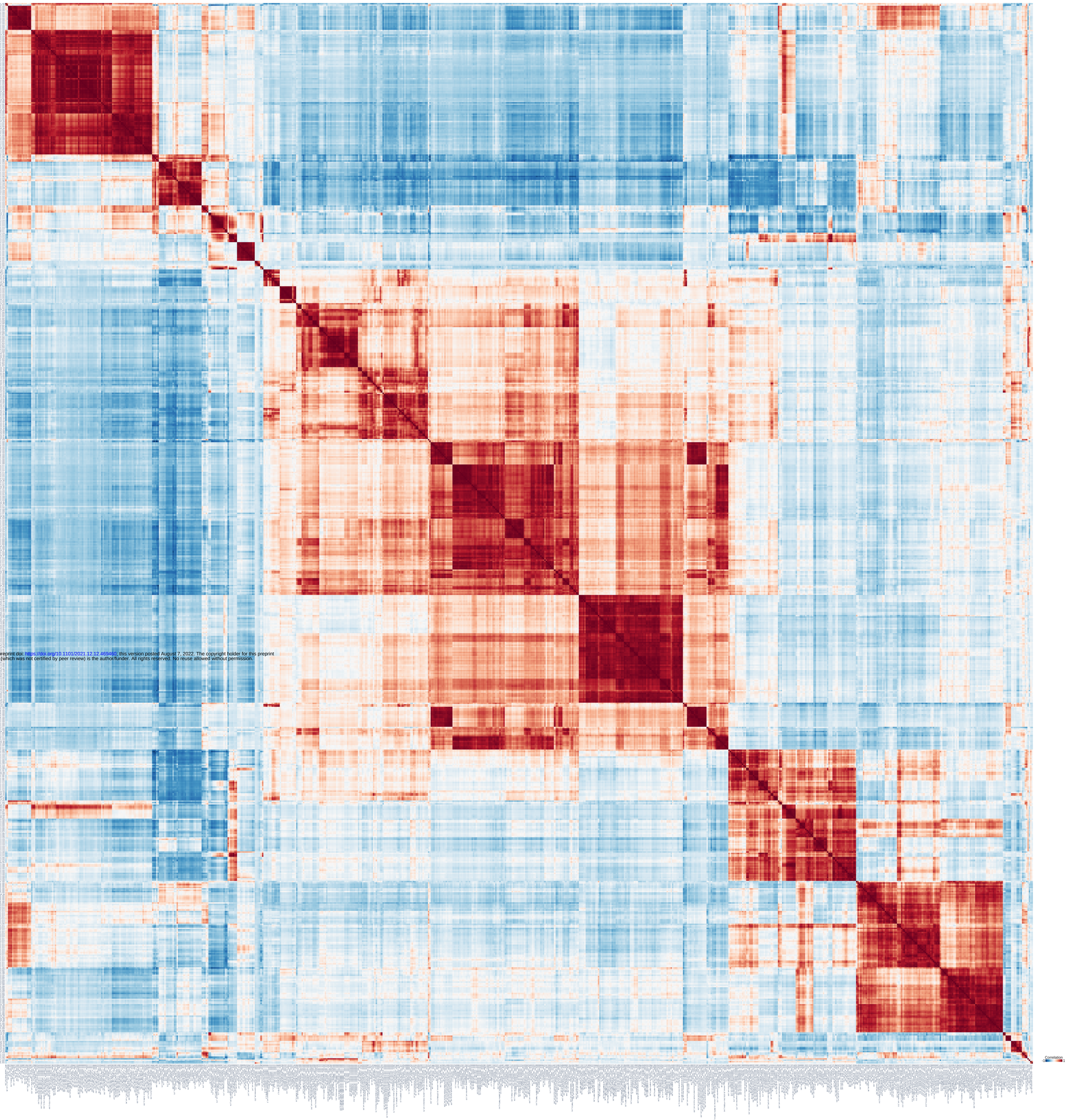

bioRxiv preprint doi: https://doi.org/10.1101/2021.12.12.469460; this version posted August 7, 2022. The copyright holder for this preprint (which was not certified by peer review) is the author/funder. All rights reserved. No reuse allowed without permission.

bioRxiv preprint doi: https://doi.org/10.1101/2021.12.12.469460; this version posted August 7, 2022. The copyright holder for this preprint (which was not certified by peer review) is the author/funder. All rights reserved. No reuse allowed without permission.

Fig. S8

a Lung Sankey plot

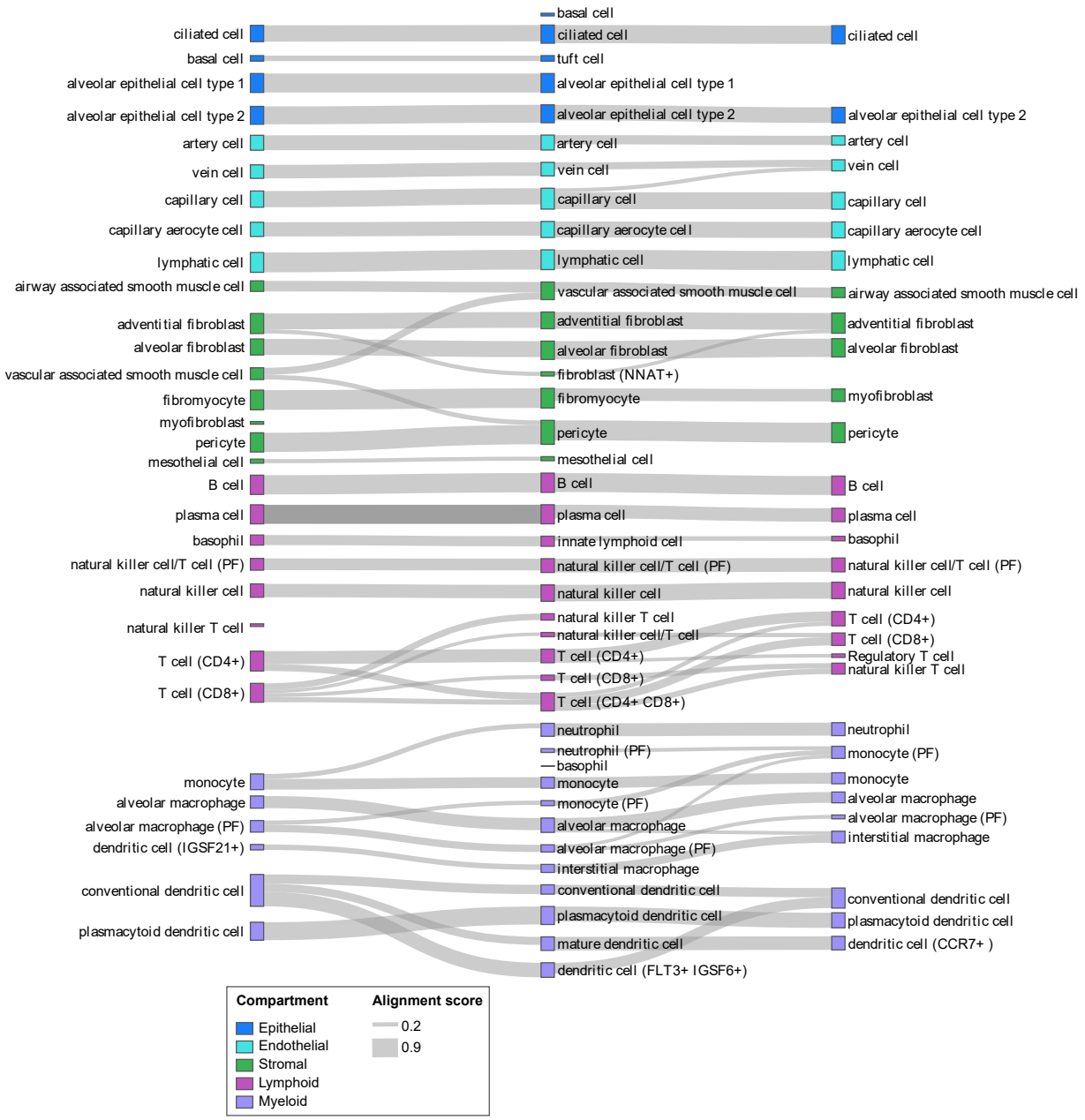

b Lung BBKNN-corrected UMAP

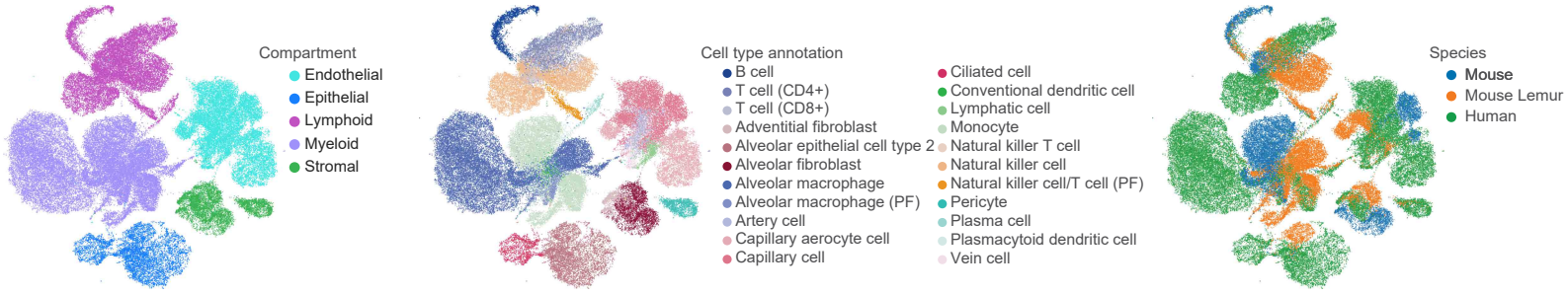

bioRxiv preprint doi: https://doi.org/10.1101/2021.12.12.469460; this version posted August 7, 2022. The copyright holder for this preprint (which was not certified by peer review) is the author/funder. All rights reserved. No reuse allowed without permission.

Fig. S8 - continued

c Limb muscle Sankey plot

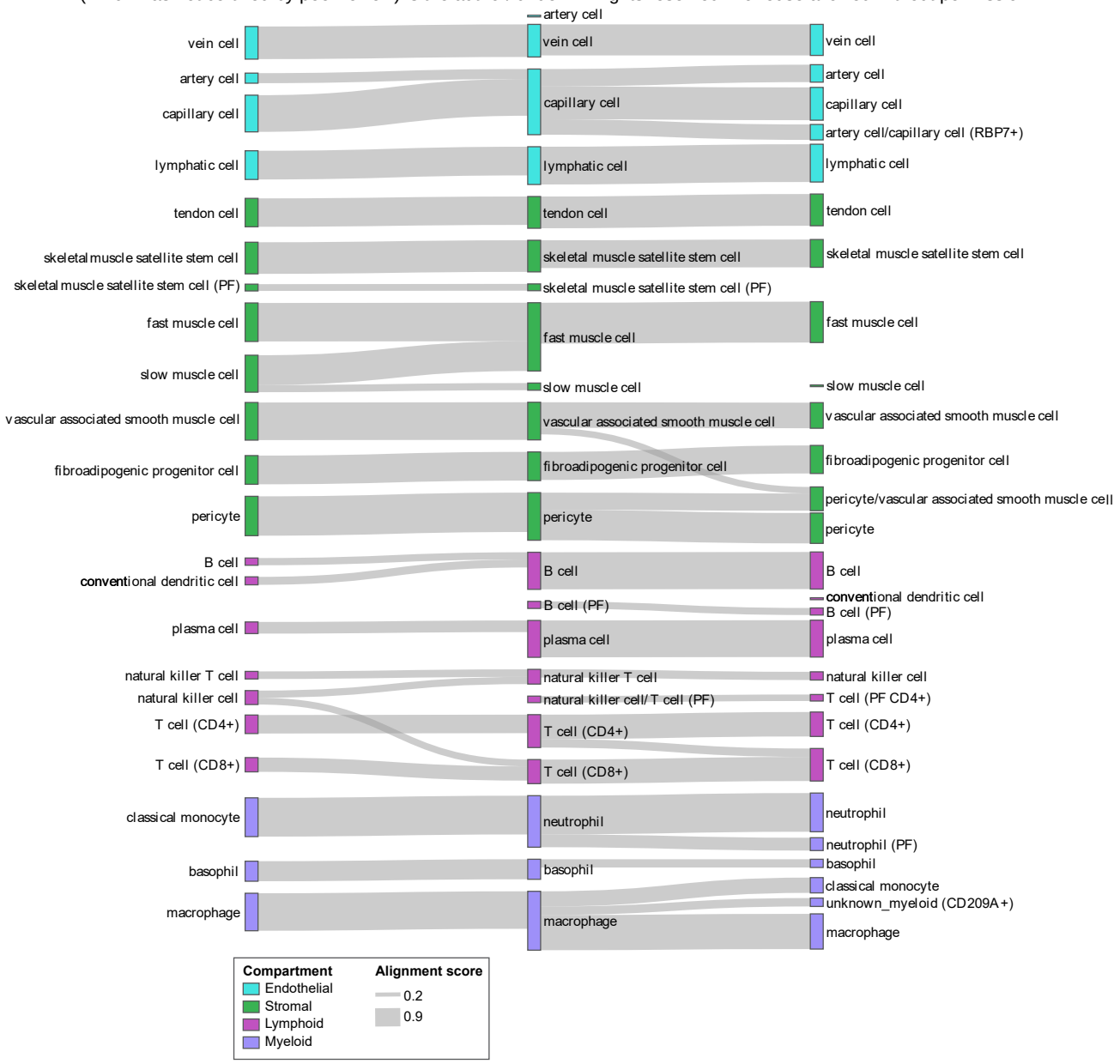

d Limb muscle BBKNN-corrected UMAP

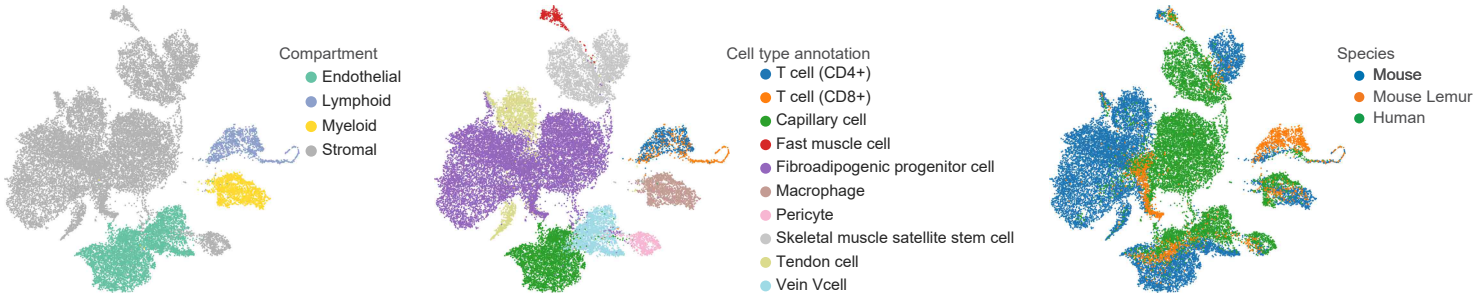

e Limb muscle Xi correlation

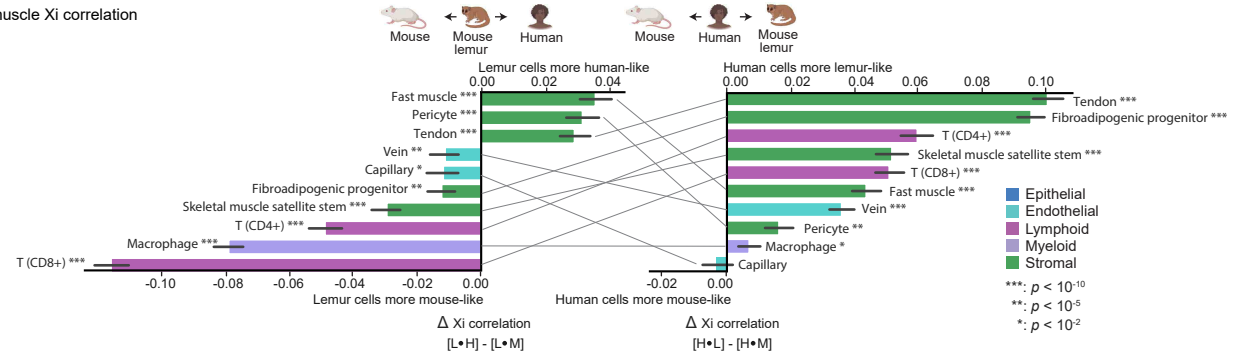

bioRxiv preprint doi: https://doi.org/10.1101/2021.12.12.469460; this version posted August 7, 2022. The copyright holder for this preprint (which was not certified by peer review) is the author/funder. All rights reserved. No reuse allowed without permission.

Fig. S9

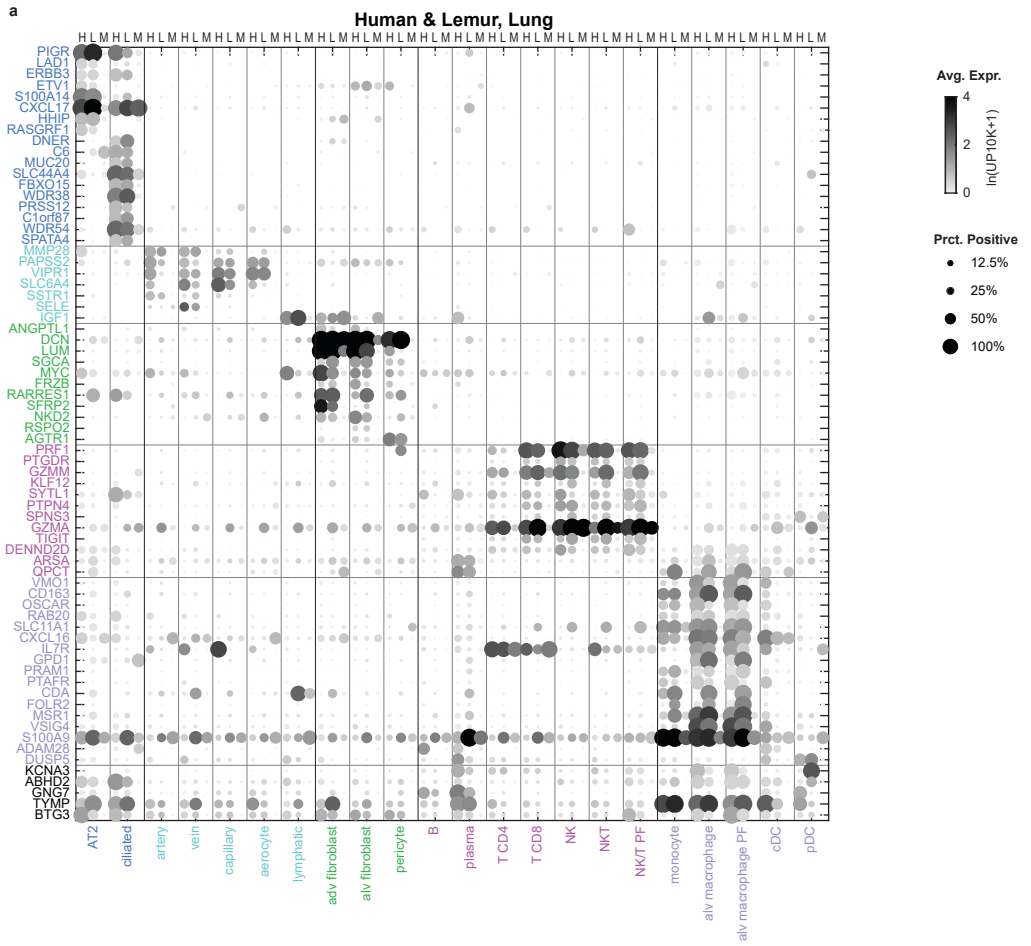

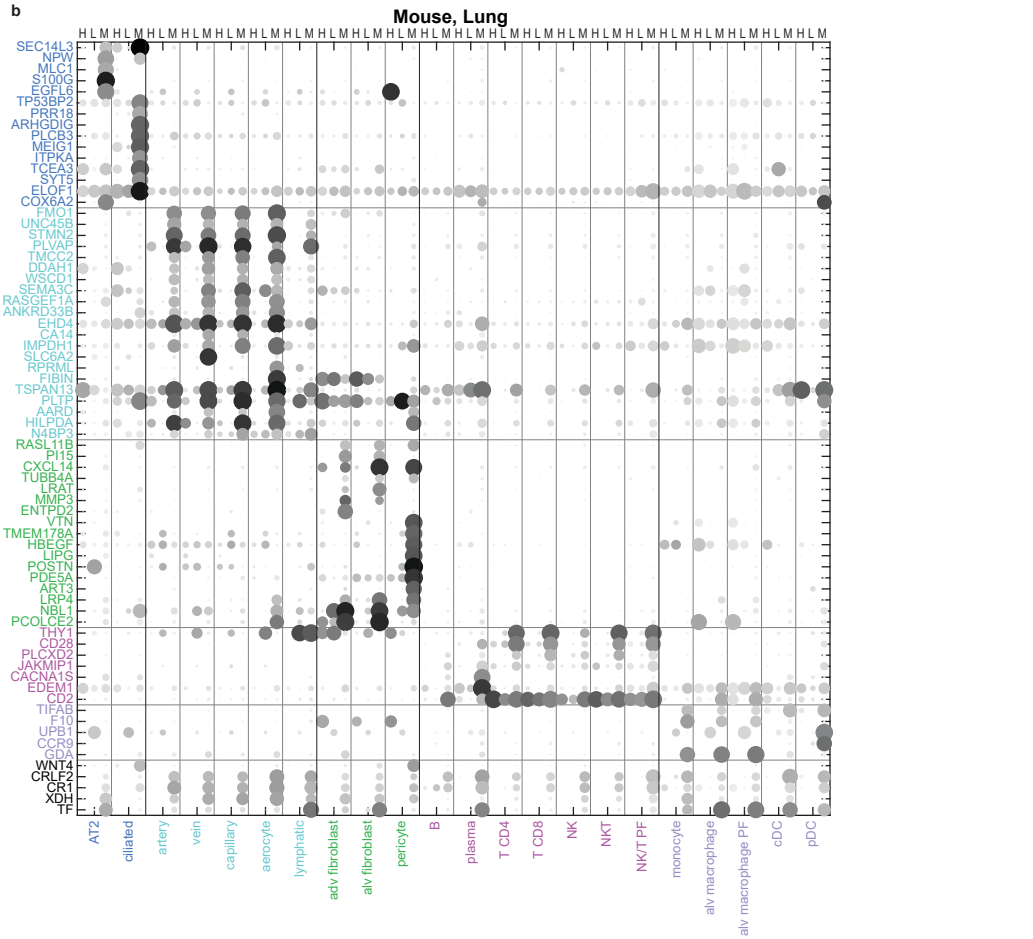

bioRxiv preprint doi: https://doi.org/10.1101/2021.12.12.469460; this version posted August 7, 2022. The copyright holder for this preprint (which was not certified by peer review) is the author/funder. All rights reserved. No reuse allowed without permission.

Fig. 89 - continued

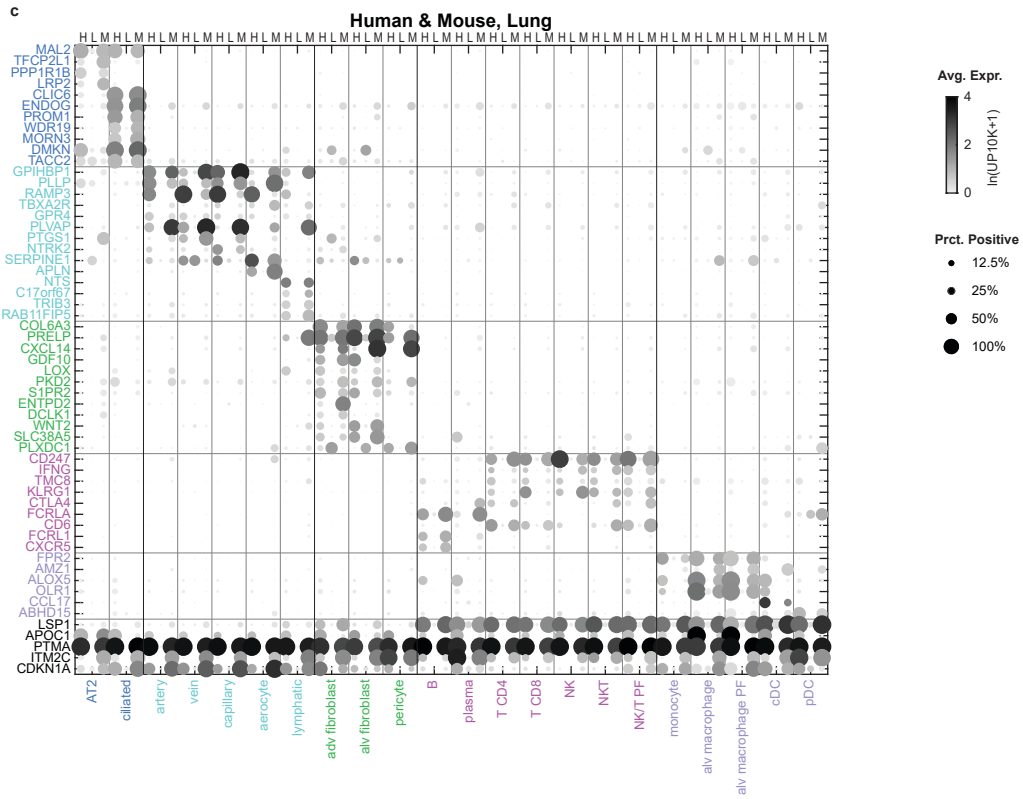

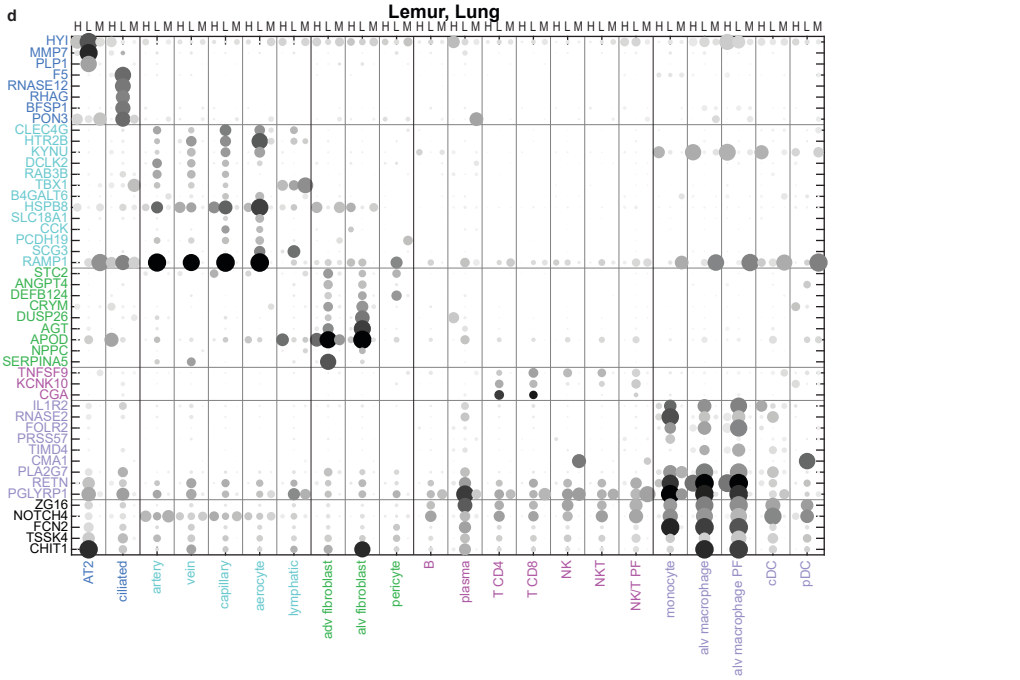

bioRxiv preprint doi: https://doi.org/10.1101/2021.12.12.469460; this version posted August 7, 2022. The copyright holder for this preprint (which was not certified by peer review) is the author/funder. All rights reserved. No reuse allowed without permission.

Fig. 89 - continued

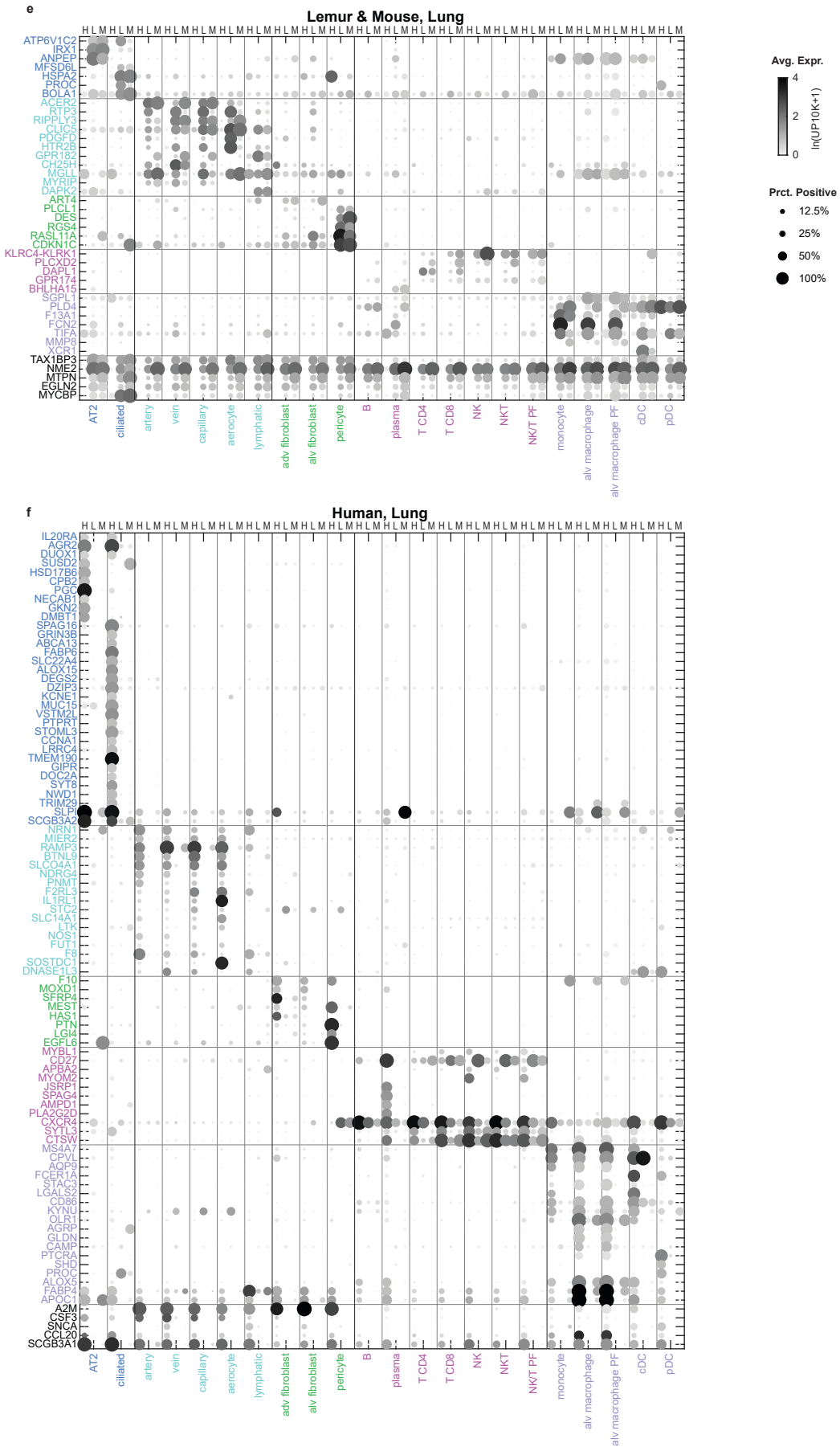

bioRxiv preprint doi: https://doi.org/10.1101/2021.12.12.469460; this version posted August 7, 2022. The copyright holder for this preprint (which was not certified by peer review) is the author/funder. All rights reserved. No reuse allowed without permission.
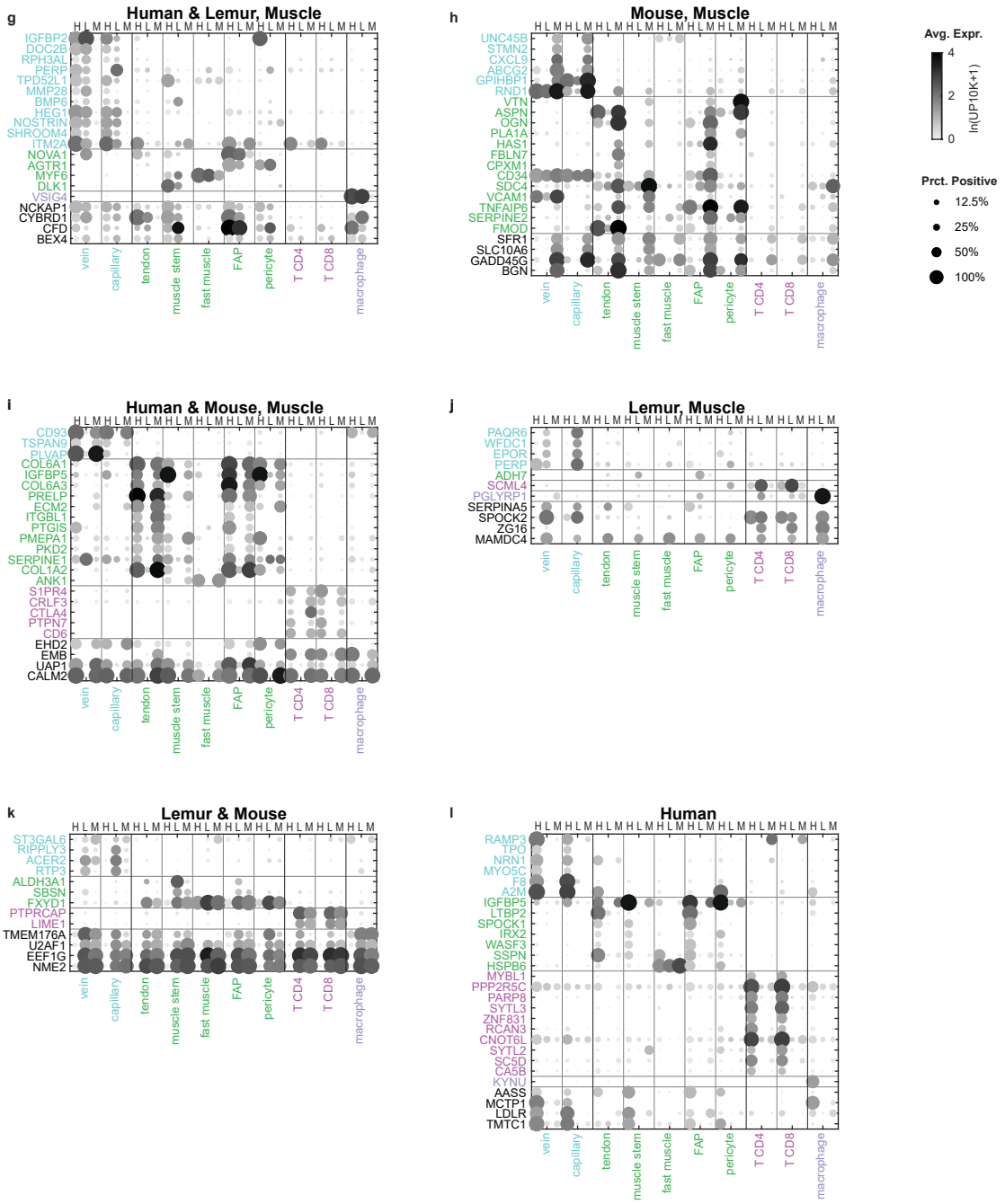
Fig. 89 - continued